MRI of Structure-Based Ventricular Mechanics

by

Wen-Yih Isaac Tseng

M.D., School of Medicine
National Taiwan University, 1987

SUBMITTED TO THE DEPARTMENT OF NUCLEAR ENGINEERING IN PARTIAL FULFILLMENT OF THE REQUIREMENTS FOR THE DEGREE OF DOCTOR OF PHILOSOPHY IN RADIOLOGICAL SCIENCES

AT THE

MASSACHUSETTS INSTITUTE OF TECHNOLOGY

FEBRUARY 1998

Signature of Author: .....
Department of Nuclear Engineering
January 9, 1998

Certified by: .....
Van Wedeen
Assistant Professor of Radiology at Harvard Medical School
Thesis Supervisor

Accepted by: .....
David Cory
Assistant Professor of Nuclear Engineering
Thesis Reader

Accepted by: .....
Lawrence Lidsky
Chairman, Departmental Committee on Graduate Students

MRI of Structure-Based Ventricular Mechanics

by

Wen-Yih Isaac Tseng

Submitted to the Department of Nuclear Engineering on January 9, 1998,
in partial fulfillment of the requirements for the degree of Doctor of Philosophy

Abstract

The relation between myocardial kinematics and underlying architectural components is the key to understanding the functional design of the ventricular myocardium. This thesis develops a completely noninvasive method, registered diffusion and strain MRI, to acquire information about myocardial architecture and myocardial strain under identical *in-vivo* conditions. This noninvasive methodology solves important limitations of existing methods all of which require myocardial dissection. It provides metrically correct data of myocardial structure and myocardial function without postmortem distortion. Further, it can be applied to living humans and allows examinations of multiple time horizons, essential to the study of normal development and disease.

To provide a valid MR methodology to study myocardial structure and structure-function relations in living humans, we focus on the three steps most essential to achieving this goal: 1) validate the correspondence between diffusion MRI and myocardial architecture, particularly the fiber and sheet organizations; 2) develop a practical method of measuring myocardial diffusion *in vivo*; 3) show that data obtained by registered diffusion and strain MRI can be employed to address important questions about myocardial structure-function relations.

To validate the ability of diffusion MRI to map myocardial architecture, we show, with a novel printing technique, that the deviation of sheet orientations is within MR noise from those in the cow heart specimens. The correspondence between directions of greatest diffusivity and fiber orientations is also verified by the consistency of architectural patterns in MRI of the cadaver heart with those reported in histology. To measure myocardial diffusion *in vivo*, a robust MR method is developed. In the normal heart that has the synchronous contraction, we show that the strain effect is negligibly small at time points relative to which the mean strain over one cardiac cycle equals zero: "sweet spots." Using this fact, we localize the sweet spots and show that the depicted myocardial fiber architecture agrees with the *ex-vivo* results.

Using registered diffusion and strain MRI, we obtain first quantitative maps of fiber and sheet dynamics in human hearts. Anatomically, MRI shows the classic pattern of fiber helix angles, namely a smooth transmural variation from a left-handed helix at the epicardium to a right-handed helix at the endocardium. It also shows a septum-versus-free-wall polarization of sheet orientations, a pattern recently documented in canine hearts. Analysis of conjoint data of diffusion and strain gives a clear picture of myocardial structure-function relations: 1) systolic fiber shortening, 11±3% relative to end-diastole, is exceptionally uniform across the wall; 2) cross-fiber shortening has a steep transmural slope; it is produced by a linear variation of angles between fibers and directions of principal shortening against wall depth (from 0° at the epicardium to 90° at the endocardium). Moreover, MRI shows two new findings: 1) there is no difference in fiber shortening between trabecular and compact myocardium; 2) sheet orientations are optimized to maximize sheet shear.

In conclusion, registered diffusion and strain MRI can map myocardial structure and structure-function relations practically and reliably in living human subjects. The noninvasive and spatially resolved characteristics of this methodology will facilitate investigation of myocardial mechanics in human disease.

Thesis Supervisor: Van J. Wedeen, M.D.
Title: Assistant Professor of Radiology at Harvard Medical School

Acknowledgments

I am grateful for what I experienced in the last four and a half years of my Ph.D. study. There were ups and downs, joys and pains during this phase. However, when I look back, they all accrue to the good of me and constitute the most precious memory in my life.

I express my sincere gratitude for my adviser Dr. Van Wedeen. His insightful guidance is indispensable to the accomplishment of this thesis. He cultivates my appreciation of science, and shows me through his own life how to be a researcher for truth. I am also indebted to his wife Dr. Lauren Abbate for her kind understanding of my frequent calls for Van, even a call at four o'clock in the morning.

I thank my respectful colleague Dr. Timothy Reese. His professional pulse programming and technical support greatly facilitate the progress of this project. I also appreciate his lectures that familiarize me with the MR machine.

I thank the members of my thesis committee: Professor David Cory, Professor Rohan Abeyaratne, Dr. Howard Kantor, and Dr. Robert Weisskoff. Their auspices have been invaluable to the success of my thesis. Communication with them is always inspiring.

I thank Professor Thomas Brady, Professor Bruce Rosen, Professor Sidney Yip, and Professor Sow-Hsin Chen for their encouragement and support when I was in need.

I thank editors of MIT writing center. Their mastery is the timely aid of the awkwardness of my written English.

I thank my parents for their endless care and concern.

I thank my wife Jenny. Her love is the shelter of my soul.

I thank God for been the source of my strength.

This work is supported in part by The Sol Goldman Charitable Trust, The Whitaker Foundation and The National Institute of Health (NHLBI1RO1 HL5627-0181).

Biographical Note

Education

1980 B.S., National Tsinghua University

1987 M.D., National Taiwan University, School of Medicine

1998 Ph.D., Massachusetts institute of Technology

Experience

1988 - 1992 Resident Doctor in Radiology, National Taiwan University Hospital

1992 - 1993 Attending Doctor in Radiology, National Taiwan University Hospital

1993 - 1996 Teaching Assistant, Department of Nuclear Engineering, MIT

1994 - 1997 Research Assistant, MGH-NMR Center, Charlestown, MA

Honor

Recipient, Outstanding Teaching Assistant Award, 1997.

Member

Alpha Nu Sigma, Sigma Xi.

Publications

Tseng W-Y. I., Reese, T.G., Weisskoff, R.M., Brady, T.J., Dinsmore, R.E., Wedeen, V.J., "Mapping myocardial fiber and sheet function in humans by magnetic resonance imaging," paper presented at American Heart Association, 70th scientific sessions, November, 1997, Orlando, FL, USA.

Tseng W-Y. I., Reese T.G., Dinsmore R.E., Weisskoff R.M., Wedeen V.J., "Progress in MRI of myocardial structure and function using diffusion and strain," paper presented at the International Society for Magnetic Resonance in Medicine, fifth scientific meeting and exhibition, April, 1997, Vancouver, B.C., Canada.

Chen S-J., Tseng W-Y., Tsang Y-M., Su C-T., Chang Y-C., Hsu J. C-Y., "Computed tomographic features of thymic carcinoid," Chinese J Radiology 1994;19:209-215.

Shih T., Tseng W-Y., Su C-T., Chiu L.C., "Multiplanar gradient recalled images of the knee: comparison of different flip angles and echo times," J Formosan Med Assoc 1992;91:976-981.

Tseng W-Y., Li Y-W., Shieh C-P., Su C-T., "Solid and papillary neoplasm of the pancreas: report of three cases," J Formosan Med Assoc 1991;90:1119-1123.

Tseng W-Y., Li, Y-W., Su I-J., Lin D-T., Huang K-M., "Burkitt's and Non-Burkitt's type lymphoma: clinicopathological and radiological manifestations," J Formosan Med Assoc 1991;90:357-364.

Contents

1 Introduction **13**

1.1 Overview....13

1.2 Background Outline.... 14

1.3 Myocardial Fiber Architecture of the Left Ventricle....15

1.4 Functional Significance of the Myocardial Architecture.... 19

1.4.1 Fiber function.... 19

1.4.2 Sheet function.... 22

1.5 Myocardial Strain Measurement....24

1.5.1 Magnetization tagging.... 24

1.5.2 Velocity-sensitive phase shift....26

1.6 Myocardial Diffusion Measurement.... 28

1.6.1 NMR pulsed gradient diffusion measurement.... 28

1.6.2 MRI of anisotropic diffusion.... 30

2 Validation of Diffusion Tensor MRI of Myocardial Architecture **41**

2.1 Correspondence of the MR Secondary Diffusion Anisotropy with the Sheet Orientation....42

2.1.1 Introduction....42

2.1.2 Methods....43

2.1.3 Results.... 44

2.1.4 Discussion.... 45

2.1.5 Conclusion....47

2.2 Correspondence of the MR Principal Diffusion with the Fiber Structure.... 47

2.2.1 Introduction....47

2.2.2 Methods....49

2.2.3 Results.... 51

2.2.4 Discussion.... 51

2.2.5 Conclusion....53

2.3 Mapping of Sheet Orientation Using MR Secondary Diffusion Anisotropy..... 54
2.3.1 Introduction..... 54
2.3.2 Definitions of sheet angle..... 54
2.3.3 Methods..... 56
2.3.4 Results..... 56
2.3.5 Discussion..... 57
2.3.6 Conclusion..... 59

Appendix A1 Calculation of prolate spheroid coordinates from Cartesian cardiac coordinates..... 60
Appendix A2 Three rotation matrices for transformation from local cardiac to structural coordinates..... 61

3 Diffusion Tensor MRI of Architectural Derangement in the Diseased Myocardium 76
3.1 Introduction..... 76
3.2 Methods..... 77
3.3 Results..... 78
3.3.1 Hypertrophic cardiomyopathy..... 78
3.3.2 Infarct expansion..... 78
3.3.3 Quantitative comparison..... 79
3.4 Discussion..... 80
3.5 Conclusion..... 82

4 Cardiac Diffusion Tensor MRI *In Vivo*: A Practical Method without Strain Correction 88
4.1 Introduction..... 88
4.2 Theory..... 89
4.3 Experiments and Results..... 92
4.3.1 MRI acquisition methods..... 92
4.3.2 Trace ADC movie..... 92
4.3.3 Myocardial architecture..... 93
4.4 Discussion..... 94
4.4.1 Synchrony assumption..... 95
4.4.2 Linear assumption..... 96
4.4.3 Movie method..... 96

4.5 Conclusion 97

5 Noninvasive Imaging of Human Myocardial Fiber and Sheet Functions Using Magnetic Resonance 103

5.1 Introduction 103
5.2 Theory 105
5.2.1 Cardiac synchrony 105
5.2.2 Localization of the sweet spot 106
5.2.3 Net systolic strain 107
5.3 Methods 107
5.3.1 MRI acquisition 107
5.3.2 Strain MRI 108
5.3.3 Diffusion MRI 108
5.3.4 Cardiac coordinates 109
5.4 Results 110
5.4.1 3D display of fiber orientation and strain tensor field 110
5.4.2 Strain component maps 110
5.4.3 Uniformity of the fiber shortening 111
5.4.4 Orientations of fibers relative to the principal shortenings 112
5.4.5 Orientations of sheets relative to the principal thickenings 112
5.5 Discussion 112
5.5.1 Fiber shortening 113
5.5.2 Unity of trabecular and compact myocardial function 113
5.5.3 Significance of sheet orientations 114
5.5.4 Error analysis 114
5.5.5 Future work 115
5.6 Conclusion 116
Appendix A3 Conversion of reference state of strain from mid-systole to end-diastole 117

6 Conclusions 125

6.1 Summary 125
6.2 Conclusion 127
6.3 Future work 128

List of Figures

1.1 Reconstructed fiber pathways on one and two cusped toroidal shells.....34

1.2 Sequence of photomicrographs in epicardial tangent plane, showing gradual change of helix angle through ventricular wall of a canine heart..... 35

1.3 Transverse section through the human left ventricular free wall at mid-ventricular level showing feathering pattern of cleavage planes.....36

1.4 Electron micrographs of laminar sheet architecture: (a) gross view, (b) x 145 magnification..... 37

1.4 Electron micrographs of laminar sheet architecture: (c) x 510, (d) x 1050 magnification.....38

1.5 Mechanisms for smoothing transmural differences in fiber shortening during systole (a), and for wall thickening through sheet slippage (b).....39

1.6 Evolution of spatial modulation of magnetization in pulsed gradient spin-echo diffusion sequence..... 40

2.1 A histologic section showing cleavage planes and a short axis MRI of 1-2 eigenspace of the diffusion tensor..... 62

2.2 A digitized image of cleavage planes inked from a cut face of a longitudinal slab (top), the traced lines of the above digitized image (middle), the traced lines and boundary superimposed over the computed intersections of the diffusion tensor MRI of the same specimen (bottom)..... 63

2.3 Histograms of specimens 1, 2, 3 and 3', and a histogram of disparity angles that is a multiplication of a Gaussian function and $\sin(\theta)$.....64

2.4 3D orientation of the fiber and geometric illustration of the helix and imbrication angles..... 65

2.5 An ellipsoid that best fits the epicardial contours from base to apex.....66

2.6 Longitudinal and radial vectors at each pixel in the image-coordinates {X, Y, Z}..... 67

2.7 Helix angle maps in 10 slices from base to apex (top), and helix angle histogram of the same fiber population (bottom)..... 68

2.8 Imbrication angle maps in 10 slices from base to apex (top), and imbrication angle histogram of the same fiber population (bottom) 69
2.9 Linear regression of the mean imbrication angles versus distance along apex to base direction 70
2.10 Three successive rotations from local cardiac coordinates (**c**, **L**, **r**) to structural coordinates (**f**, **s**, **n**) 71
2.11 A plot of angular error using Eq. 2.6 to calculate sheet angle γ 72
2.12 Sheet architecture at mid-ventricle level rendered by a three-dimensionally oriented disc at each pixel 73
2.13 Sheet angle maps and histogram of the normal heart 74
2.14 Cardiac prolate spheroid coordinates (λ, μ, θ) in relation to rectangular Cartesian coordinates (x, y, z) 75
3.1 Multiple transaxial slices of color-coded helix angle maps of HCM heart (top) and infarct expansion (bottom) 83
3.2 Multiple transaxial slices of color-coded imbrication angle maps of HCM heart (top) and infarct expansion (bottom) 84
3.3 Overlapped helix angle histograms (top) and imbrication angle histograms (bottom) of normal, hypertrophic cardiomyopathy (HCM) and infarct expansion (IE) 85
3.4 Sheet angle maps and histogram of the HCM heart 86
3.5 Sheet angle maps and histogram of the infarct expansion heart 87
4.1 Evolution of k(t) and $k(t)^2$ in pulsed gradient stimulated-echo diffusion sequence 98
4.2 Time-course of mean trace ADC over the cardiac cycle and the mean trace ADC of the single image acquired at the cardiac sweet spot 99
4.3 Helix angle maps and histograms obtained *in vivo* and *ex vivo* 100
4.4 Imbrication angle maps and histograms obtained *in vivo* and *ex vivo* 101
4.5 Sheet angle maps and histograms obtained *in vivo* and *ex vivo* 102
5.1 Time course of the myocardial mean radial strain 118
5.2 Registered diffusion and strain MRI pulse sequences 119
5.3 Graphics display of 3D orientations of the myocardial fibers and the registered strain tensor field from a normal volunteer 120
5.4 Strain component maps in local cardiac, principal, fiber, and structural coordinates 121
5.5 Linear regressions, with confidence intervals, of normal strains versus wall depth 122

5.6 Images of helix angles of maximal principal shortening, fiber, and minimal principal shortening, and linear regression of disparity angles versus radial depth 123
5.7 Quantitative map of the sheet angles relative to the principal thickenings, and the histogram of these angles 124

List of Tables

Table 2.1 Summary of the analysis of disparity angle between MR and optical images..... 44
Table 3.1 Comparison of fiber and sheet angle distributions between normal and diseased hearts..... 79
Table 5.1 Distributions of net systolic normal strains, including fiber shortening.....111

Chapter 1

Introduction

1.1 Overview

The relation of myocardial architecture and function is the most basic question pertinent to the study of biomechanics of the heart. Previous studies of this topic mostly relied upon cardiac dissection and histology to define myocardial architecture. This approach precludes the possibilities of obtaining information about myocardial architecture and myocardial function under identical *in-vivo* conditions. More importantly, this method can never be applied to living humans. Using sensitivities of magnetic resonance imaging (MRI) unique to tissue microstructure and to tissue velocity, in this thesis, we develop a completely noninvasive method to obtain architectural and functional information concurrently in the same beating heart. With this method, registered diffusion and strain MRI, investigation of ventricular mechanics and cardiac physiology in human hearts will be greatly facilitated. To provide a valid MR methodology to study myocardial structure and structure-function relations in living humans, this thesis focuses on three most relevant goals: 1) to validate the correspondence between diffusion MRI and myocardial architecture; 2) to develop a practical method to measure myocardial diffusion *in vivo*; 3) to show

that the data of diffusion and strain can be converted into physiologically meaningful values, including the differentiation of architectural patterns of the diseased myocardial tissue from the normal, and a consistent description of normal structure-function relations with those found in animal models.

To achieve these goals, in Chapter 2, the correspondence between secondary diffusion anisotropy and the sheet structure is investigated by comparing cleavage planes shown in the diffusion MRI with those observed optically on the same cow hearts. Then the investigation extends to the correspondence of the direction of greatest diffusivity (first eigenvector of the diffusion tensor) and the fiber orientation. There, we compare MR descriptions of the fiber orientations in the cadaver hearts with the classic findings in quantitative histology. In Chapter 3, we demonstrate the capacity of diffusion tensor MRI to discern architectural change in diseased hearts, including infarct expansion and hypertrophic cardiomyopathy. To implement diffusion MRI in the beating heart, we confront a problem of correcting the effect of tissue stretch on the diffusion measurement. Therefore in Chapter 4, we develop a practical method, the sweet spot method, to circumvent this problem. In Chapter 5, we report the first noninvasive study of structure-function relations in the human heart using registered diffusion and strain MRI. Our results agree with the current understanding of the myocardial architecture and its significance to the ventricular wall function.

1.2 Background Outline

To furnish the anatomic and physiologic backgrounds of this thesis, Sections 1.3 and 1.4 of this chapter review the historic evolution of the understanding of the myocardial architecture as well as its functional significance. The facts that the myocardium has a complex fiber organization and that it is the most densely collagenous muscle of the body, make the clarification of the myocardial architecture inordinately difficult. Today, the understanding of the disposition of the myocardial fibers and its significance to the ventricular function are the result of many insightful observations for centuries. The progress culminated in the work of Streeter in the 1970's. From the systematic micrometric examinations of the myocardial fibers, he constructed a simple and clear picture of the myocardial architecture: the myocardium is a three-dimensional (3D) syncytium composed of well-organized fibers obeying simple physical rules. This picture lays the foundation of continuum model of the myocardium in ventricular mechanics.

In the last 15 years, MRI has been shown to have an exquisite sensitivity to detect tissue velocity. One further application of this unique property is to image tissue deformation or strain.

Section 1.5 introduces the basic physics of velocity-sensitive MRI and the state-of-the-art myocardial strain tensor imaging techniques. The purpose is to provide a broad view with which to assess the technologies available now. Based on this, the rationale of selecting a better velocity-sensitive MR technique and the improvement required to fulfill a robust 3D strain tensor imaging will be clarified.

The capability of encoding water molecular diffusion into the nuclear magnetic resonance (NMR) signal was noticed shortly after NMR experimentation was first established. The proposal of using diffusion anisotropy to detect the orientation of microstructures is also not new. However, an attempt to implement diffusion measurement of the beating heart confronts both technical and theoretical challenges. Therefore, in Section 1.6, we will revisit the basics of MR diffusion measurement technique and its related theory. By doing so, we can define the current problem of applying this technique *in vivo*.

1.3 Myocardial Fiber Architecture of the Left Ventricle

Since the 16th century, anatomists have recognized the complexity of the arrangement of the myocardial fibers. For centuries, many investigators have striven to unravel this Gordian knot in anatomy. Their views of the myocardial architecture, though seemingly different in many aspects, converge to a common view on the whole. Today, the understanding of myocardial architecture is still evolving, but basic patterns of the fiber organization are clarified. Before presenting the modern concept of the ventricular architecture, the extensive earlier work is reviewed.

In 1664 Stensen pointed to the generally helical course of ventricular muscle [1]. Lower, in 1669, further stated that the most superficial subepicardial fibers invaginated the apex and became subendocardial or trabecular [2]. In 1749 Senac found that while the inner and outer fibers were disposed in helical fashion, those of the midwall were more circumferential [3]. Based on these ideas, in the 19th century, conceptualization of the fiber pathways of the ventricular myocardium was gradually condensed. In 1849 Ludwig stated that any cube of the heart wall extending from the pericardium to the endocardium was composed of fibers with smooth transition of their orientations across the wall [4]. He visualized the midwall fibers as forming a cylinder, and the outer-wall fibers connected to the inner-wall fibers at the apex as well as at the base in a figure-eight fashion. In 1864, Pettigrew integrated these ideas with his work and proposed a principle of the fiber arrangement [5]. He stated that the fibers of the ventricular wall readily admitted of being separated into seven layers, the fibers of each layer being characterized by having a different direction. In three outer layers, fibers ran in spiral direction from left to right

downwards, with gradation of fiber pitch across the wall. The fourth layer was situated in midwall and consisted of circumferential fibers. In three inner layers, fibers ascended in the reversed direction as a balance to the outer layers. The outermost and innermost layers were continuous at the apex, the second and the sixth were continuous somewhat above the apex, as were the third and fifth layers at a still higher level. This unique pattern of fiber organization was observed to occur in all parts of the ventricular walls. In 1891 Krehl systematized the ventricular fibers as two compartments: a myocardial circular collar in the middle layer (the "Triebwerk"), and inner and outer oblique fibers lying on a nested set of virtual toroidal shells [6]. In addition to the beauty of its simplicity, Krehl's model faithfully explained the features of the fiber organization described by Ludwig and Pettigrew.

Inspired by the conceptualization of the structural system of the heart made in the 19th century, anatomists in the 20th century found ways to dismantle the heart in order to reveal its organization. There are two seemingly different, but in fact, complementary approaches. The first approach is the blunt-dissection on a large scale. This approach inherits the belief that the myocardium is composed of a few distinct muscular bundles, and assumes that individual fiber bundles can be revealed by tearing the muscle along the plane of minimum resistance. The second approach is the micrometric method for through-wall blocks. This approach focuses on verifying orientations of fibers at each location by histology of serial sections. By sampling the tissue blocks systematically over the left ventricle (LV), 3D fiber pathways can be reconstructed based on reasonable assumption of the ventricular geometry.

In 1900, MacCallum established the blunt-dissection technique [7], a new systematic approach to the musculature of the ventricular myocardium. He dissected macerated embryo porcine hearts by following the main paths of fibers through the ventricular wall, ripping side branches, and unrolling the myocardium into separate large masses of muscle tissue. In 1911, Mall extended this technique to human hearts describing a series of complex spirals and loops of muscle within the ventricular mass [8]. He separated four main groups of fibers: the superficial and deep bulbo-spiral bands and the superficial and deep sino-spiral bands. This nomenclature was to form the basis of cardiac anatomy during the next half century. Mall-MacCallum's view of the unrolled heart muscle as a skeletal muscle of tendinous origin that inserted into the valve rings, created a unifying concept of myocardial organization that was easy to accept, and did in some sense realize the abstract models developed in the previous century.

After a half decade, the legitimacy of the blunt-dissection approach was challenged by Lev and Smikins [9]. Using a modified Mall's method, they were unable to identify the plane of cleavage between superficial and more deeply located fasciculi. They found no evidence of distinct muscle layers separated by fibrous tissue. In 1965, Grant showed that the concept of separate

muscles constituting the ventricular mass was untenable [10]. He challenged the blunt-dissection technique by indicating how subjective judgments of the dissector might influence the distribution of apparent muscle bundles. He showed that fiber matrix could be partitioned into different bundles depending on the orientation of the tearing forces employed, so he concluded that the results of such methods were not reproducible.

As a backlash, in 1973 Torrent-Guasp improved the blunt-dissection technique that revealed only the individual muscle pathways in the principal fiber direction [11]. He claimed that this technique was objective and reproducible. Using this protocol, he was able to show successive layers with a raked turban-like appearance within the ventricular myocardium, resembling Pettigrew's principle of fiber arrangement.

Another approach, the micrometric method for through-wall blocks, was first adopted by Hort in 1957 [12]. He made serial frozen sections parallel to the wall surface, and performed a microscopic examination to quantify local fiber orientations. He measured the fiber orientation from various sites of the heart wall and confirmed the mid-nineteenth century idea of continuous transition of fiber angle across the wall. A more systematic quantification of the fiber orientation was accomplished 10 years later by Streeter [13-15]. By measuring fiber orientations on parallel and rotated sections of the through-wall blocks sampled from different latitudes and longitudes of the wall, he reconstructed 3D orientations of the fiber pathways around the heart. He found that principal fiber pathways tend to follow a geodesic path on the planes parallel to ventricular wall surface. In addition, they burrow into the wall in a continuous fashion such that they make a figure-eight return to the equator (Fig. 1.1). Thus he vindicated Krehl's Triebwerk model of the heart wall, namely, that the ventricular wall can be imagined as a nested set of toroidal shells centered on the midwall on which the fiber pathways run in a helical pattern from epi- to endocardium.

At each location of the wall, Streeter referenced the 3D orientation of the fiber axis to three projected angles in orthogonal planes (tangential, longitudinal and traverse), i.e., the helix angle, the declination angle, and the traverse angle, respectively [16, 17]. Combination of declination and traverse angles gives the imbrication angle. This angle represents the rate of change in wall depth for a given fiber pathway, so it determines how steep a fiber path burrows into the wall. He found that the fiber helix angle, namely the angle of fiber on the local epicardial surface with respect to local latitude, varies smoothly from approximately -90° at the epicardial surface, through zero degrees near the midwall, to approximately 90° towards the endocardium (Fig. 1.2). The imbrication angle varies from approximately +15° near the base, passes 0°, changes sign through the equator, and approaches -15° near the apex.

Streeter refuted the concept of distinct bands of the heart muscle that have been claimed by many anatomists for decades. He regarded the myocardium as a well-ordered fiber-wound continuum of interconnecting muscle fibers. According to his model, elastic behavior of the myocardium can be approximated transversely isotropic. The fiber is essentially a rod structure in a lubricated near-parallel array in the vicinity (a slippery-skinned rod), carrying only axial tension and reacting to a pressure gradient laterally. Streeter's work lays the groundwork for the modern understanding of the fiber architecture. His quantification of the fiber helix angles provides invaluable information in modeling ventricular wall mechanics. However, the view of ventricular myocardium as a 3D continuum with uniform branching myocytes has been challenged in the last 5 years.

In fact, existence of regularly arranged gaps in both the right ventricle (RV) and LV walls in longitudinal and transverse sections has been reported for years. In transverse sections, these gaps can be readily recognized in the appearance of feathering or pinnation pattern converging toward the midwall (Fig. 1.3). Hort described these gaps as systematically ordered anastomosis-poor sections in the myocardium providing delicate regulation of the movement of muscle fibers with one another [18]. These gaps, however, had never been acknowledged as an indispensable part of the myocardial architecture.

In 1979 Caulfield and Borg described a hierarchy of the connective tissue in the myocardium [19]. They noted that myocytes were connected to adjacent myocytes by a regular array of radial collagen fibers. They also reported that a connective tissue meshwork surrounded groups of three or more myocytes, and that adjacent bundles of myocytes were loosely coupled by sparse and relatively long collagen fibers. In 1995 LeGrice systematized the relationship between 3D arrangement of myocytes and the extracellular connective tissue matrix in dog hearts [20]. He found that the myocardium consists of an ordered laminar arrangement of myocytes with extensive cleavage planes between muscle layers. Individual sheets of myocytes, approximately four cells thick, are stacked on one another and are twisted according to the orientational change of the constituent myocytes. Each sheet is wrapped by an extensive meshwork of connective tissue. Within each sheet, myocytes are bound tightly to each other by dense radial collagen cords. There are appreciable spaces with sparse long collagen fibers interconnecting between adjacent sheets (Fig. 1.4). The organization of these microscopic sheets corresponds to macroscopically visualized cleavage planes on the tissue sections. From these findings, LeGrice concludes that the ventricular myocardium is not a continuous structure composed of 3D network of fibers. It is actually a laminar hierarchy in which the existence of discontinuity can be identified at both microscopic and the macroscopic levels.

Therefore, the modern view of the myocardial architecture is a laminar hierarchy. At any point of the heart wall, local myocardial architecture is represented by a stack of sheets composed of parallel fibers. The orientation of the fibers at each location conforms to Streeter's classic description. The sheet direction is determined by the direction of lateral extent of these parallel fibers. The material symmetry at each location can be defined by three orthogonal axes paralleling fiber, sheet, and sheet normal vectors, and hence is orthotropic.

1.4 Functional Significance of the Myocardial Architecture

Since Streeter's description of unique helical fiber orientation, many investigators have proposed various explanations of its role in myocardial contraction and relaxation. Among these, only a few have solid experimental supports. To verify the functional role of fiber architecture, at least two pieces of information are required; they are fiber orientation and myocardial deformation. By combining these two sets of data, and by analyzing their relationships over different regions of the ventricular wall, some simplifying principles governing the mechanical role of the fiber architecture can be revealed. In principle, structural information and functional information need to be obtained simultaneously from the same location of the beating heart. Technically, this requirement is extremely difficult to attain; though myocardial function can be measured *in vivo* using invasive or noninvasive methods, fiber architecture can only be determined by dissection and histology. How much the structural information obtained *ex vivo* deviate from *in-vivo* situations is not clear. Assuming this error to be insignificant, investigators have tried to carry out the studies on canine hearts, and have obtained results that may shed light on the functional role of the fiber and sheet organizations.

1.4.1 Fiber function

Cumulative evidence from the results of animal experiments and computer simulation points to two functional roles of the fiber architecture. First, fiber helical pattern allows transmission of the fiber contraction from the outer wall to the inner wall through transmural coupling of the associated connective tissue. This force transmission results in remarkable cross-fiber shortening in the inner wall, which in turn leads to significant thickening in radial direction. Second, fiber helical pattern is the result of a local feedback process to equalize fiber stress and fiber strain across the wall. Equalization of the fiber work load is believed to be the manifestation of physiologically uniform distribution of coronary perfusion and cell metabolism in the wall. In the following paragraphs, lines of evidence supporting these two hypotheses will be described in detail.

In 1988 Waldman et al. first determined 3D myocardial deformation and fiber orientation in the anterior free walls of the LV in seven dogs [21]. Myocardial deformation was measured by recording motions of implanted radiopaque markers with high-speed, biplane cineradiography. Local myocardial 3D strain tensor with respect to end-diastole was computed from relative displacements of tetrahedrons demarcated by the markers. Hearts were then fixed at end-diastole and sectioned parallel to the local epicardial tangent plane to determine the transmural distribution of fiber directions at the site of strain measurement. Waldman found that, as compared to the wide range of fiber orientation ($\approx 180^{\circ}$), transmural variation of the direction of maximal shortening is relatively small ($\approx 90^{\circ}$). In particular, the directions of fiber and maximal shortening are not substantially different in the outer wall, but are orthogonal to each other in the inner wall. Deviation of maximal shortening direction from the fiber axis indicates some mechanism, other than fiber contraction, participating in this off-line shortening. Waldman proposed two possible mechanisms responsible for this deviation: 1) rearrangement of myocytes and 2) shape change in the cross sections of myocytes or the interstitium. Consequently, the maximal shortening orthogonal to the fiber axis in the inner wall leads to a larger radial thickening based on incompressibility of the myocardium. Waldman's finding implies that purpose of the helical pattern of the fiber orientation is to promote inner wall thickening during contraction. However, the accuracy of the data is compromised by the invasive procedure of recording the wall motion (opening the chest and traumatizing the myocardium) as well as uncontrollable errors arising from *ex-vivo* determination of the fiber orientation (incompatible physiological conditions and specimen distortion during tissue preparation).

To clarify the significance of helical fiber pattern relative to the wall thickening in a less invasive way, in 1994 Rademarkers et al. measured 3D myocardial strain on ten closed-chest dogs using NMR tagging technique [22]. After strain measurement, dogs were sacrificed and the fiber orientation at the same site of strain measurement was determined using a dissecting microscope. By recording strain tensors at 20 time points during systole, he statistically compared the correlation between different strain components (fiber shortening, cross-fiber shortening and in-plane shear) at different regions (endo- and epicardium). He reported that there is strong correlation between fiber shortening on one side of the wall with cross-fiber shortening on the other side. The finding suggests that there is strong coupling of the fiber shortening between the inner wall and the outer wall. He also found by regression analysis that epicardial and endocardial cross-fiber shortenings have strong relation to total wall thickening. These results support the hypothesis that contractile force of the fiber has been carried through the wall via connective tissue coupling from layer to layer. Because fibers in the outer wall, presenting a left-hand helix, and those in the inner wall, presenting a right-hand helix, are crisscrossing, contraction of fibers in the outer wall exerts exceedingly large cross-fiber shortening (three times the fiber shortening) in the

inner-wall. Consequently, spontaneous shortening in fiber and cross-fiber directions leads to a remarkable thickening in the radial direction. Structural basis of the cross-fiber shortening may be either slippage motion between myocyte bundles (i.e., sheet slippage inducing cellular rearrangement) or anisotropic stretching of the individual myocyte and/or sheet cross sections.

To study the dynamics of fiber architecture in the human heart and detect its change in disease, in 1997 MacGowan et al. applied the same MR tagging method to normal volunteers and patients with idiopathic dilated cardiomyopathy [23]. That study has two limitations. First, fiber orientation could not be determined from the same person who undertook noninvasive myocardial strain measurement by MR tagging. To circumvent this problem, they used fiber orientation data from other autopsy specimens assuming invariability of the fiber orientation between different hearts. Second, because of limited imaging time to obtain higher tag density, the mesh size for myocardial strain computation was on average 2.5 cm. These limitations illustrate the sheer difficulties of investigating myocardial structure-function relations on living human hearts.

Another hypothesis regarding functional significance of the fiber helical orientation is enunciated by Arts [24]. He claims that helical fiber orientation is the result of an adaptive process to equalize fiber stress and sarcomere shortening across the wall. In modeling the left ventricular wall as a thick-walled cylinder composed of 8 concentric shells, he incorporates anisotropic material property according to classic transmural transition of the fiber orientation. Simulation of cardiac contraction shows that, in contrast to conventional models based on isotropy, transmural distribution of stress and strain in the fibers appears to be rather uniform. In computer simulation, he also shows that equalization of fiber stress and fiber strain is achieved by the combination of cardiac torsion and transmural gradation of fiber angle which effectively levels off existing transmural difference of segmental shortening. This mechanism is explained and illustrated by diagrams in Figure 1.5 (a). He further hypothesizes that the fiber orientation is controlled by the feedback signals: fiber stress, end-diastolic sarcomere length, and sarcomere shortening during ejection [25]. With this feedback system set up, a stable final solution for the transmural course of fiber orientation can be achieved after self-correcting iterations. This final solution yields a homogeneous fiber load within ±2%, and is close to anatomical findings of fiber geometry reported in many species.

In fact, the uniformity of fiber work load and fiber strain is supported by many lines of experimental evidence. Transmural distribution of coronary perfusion was found to be uniform within ±10% at rest [26], and became even more uniform during exercise. The difference in cellular metabolism between endocardium and epicardium is insignificant [27]. Waldman, Rademarkers, and Bloomgarden [21, 22, 28] separately measured the fiber shortening in dog

hearts using different methods. They consistently found that fiber shortening is quite uniform across the wall.

The uniformity of fiber stress and fiber strain has potential significance in the evaluation of ventricular function. The contractile function of the heart wall can be indicated by a single active action, i.e., the fiber shortening. Furthermore, myocardial infarction results in imbalance of the fiber shortening and fiber loading. The adaptive process of the myocardium to resume uniformity of the fiber dynamics might closely relate to the process of ventricular remodeling.

1.4.2 Sheet function

In cardiac pump cycle, the ventricular wall undergoes 20% – 40% thickness change between contraction and relaxation, while the length of fiber or sarcomere changes by about 15% [29]. Given such an amount of fiber strain, simple calculation assuming incompressibility yields about 8% change in cross fiber direction, equivalent to one- to two-fifths of wall thickness change only. The explanation for this paradox was first described by Hort [12, 18]. He counted the number of fibers across the ventricular wall in various contracted and dilated hearts of guinea pigs and dogs. He noticed that there was a significant difference in transmural fiber number between dilated and contracted walls. Hort also measured the cross sections of the fibers in these walls, and found that fiber cross sections did not change significantly between different states. He speculated that the mechanism of this cell number change was due to distinct gaps or planes found in the myocardium, which provided freedom for fibers to slide on one another laterally. It resulted in rearrangement of the fibers and hence the observed variation in fiber number across the wall.

Hort's contention was further verified by Spotnitz et al. [30]. By examining longitudinal sections of the whole wall of rat hearts, fixed in different filling ventricular volumes, the numbers of fibers across the wall and the fiber density (the number of fibers per unit area) were correlated with wall thickness. His finding was consistent with Hort's: the wall thickness associated closely with the number of fibers across the wall, and the decrease in wall thickness was 3 to 4 times greater than the decrease in fiber density. Moreover, he illustrated how the gaps or cleavage planes in the myocardium change orientations to accommodate change in transmural fiber number. In thick-ventricular walls, these planes generally approached a horizontal orientation, while in thin walls, the planes tilted vertically along the ventricular axis, forming acute angles with the epicardium and endocardium.

In 1995 LeGrice documented that the myocardium was indeed a composite laminar structure [20], and that the spaces between adjacent laminae (or sheets) formed distinct cleavage planes observed on the macroscopic scale. He further hypothesized that the slippage motion between adjacent sheets provided an anatomic basis for myocyte (or cellular) rearrangement to

occur during systole [31]. To prove the hypothesis, he chose two regions where cleavage planes were opposite in orientation, i.e., anterior free wall and the septum of the LV, and correlated the 3D orientations of the cleavage planes with the myocardial strains measured at the same site. The myocardial strain was first measured on the anaesthetized open-chest dogs by recording the motion of the implanted metallic beads. After strain measurement, hearts were sectioned and 3D cleavage plane orientations at the site of strain measurement were determined in three orthogonal planes. He found that sheet shears in these two regions were opposite in sign, but they consistently contributed to wall thickening. The amount of wall thickening calculated from the shear amount and the cleavage plane angles at these two regions showed reasonable correspondence to the measured thickening strain. In the inner third of the wall, there was a close match between the planes of maximum shear and the planes of the sheet structure. He concluded, in the inner wall of anterior free wall and septum, systolic wall thickening was mostly contributed by slippage motion between the sheets. The mechanism of wall thickening through sheet slippage is illustrated schematically in Figure 1.5 (b).

Slippage between the sheets not only gives rise to wall thickness change during cardiac cycle; it also participates in the remodeling process of the ventricular wall undergoing hemodynamic change. Weisman et al. [32] and Olivetti et al. [33] separately showed side-to-side slippage of myocytes in both infarct and non-infarct regions of infarct expansion. Recently, apoptosis (programmed cell death) has been proposed to account for this augmented slippage in post-infarct remodeled ventricles [34].

In summary, invasive animal studies have shown the important functional significance of the myocardial architecture. The helical pattern of the fiber architecture is thought to equalize fiber stress and fiber strain across the wall. In addition, oblique fibers in the outer wall induce unusually large cross-fiber shortening in the inner wall; this shortening is accompanied by substantial thickening in the inner wall. This wall thickening arises from the cellular rearrangement facilitated by a shearing motion between the sheets.

Investigation of myocardial structure-function relations in the human heart is expected to give more insights into cardiac physiology and pathophysiology. However, the current paradigm of studying structure-function relations cannot provide a reliable way to determine myocardial architecture. Structural information is always obtained *ex vivo* (whether the information is obtained by post-mortem dissection or by referring to established values of unrelated hearts). The condition of the heart when it is taken out is completely different from *in-vivo* conditions when strain is measurable. Therefore, the goal of this thesis is to establish a completely noninvasive method to obtain structural information and functional information from human hearts under the same physiological conditions. We propose to use diffusion tensor MRI to map myocardial

architecture, and to use phase-contrast MRI to map wall deformation. By analyzing these data, we will produce quantitative maps of motion patterns of the fibers and the sheets. This will allow us to investigate many questions concerning structure-function relations of the myocardium.

1.5 Myocardial Strain Measurement

The inherent motion sensitivities of MRI can be exploited to measure the intramural motion of the heart wall noninvasively. Strain, as a tensor property of the relative motion between neighboring material points, can be computed based on the motion data provided by MRI. Generally speaking, there are two different approaches that utilizes unique motion-sensitive features of nuclear magnetic resonance (NMR) to detect the movement of an object: 1) magnetization tagging and 2) velocity-sensitive phase shift. In the following paragraphs, the development of strain measurement techniques based on these two NMR features is introduced. Emphasis will be put on the physical principles of these two techniques as well as their current limitations. A proposal of an improved technique for myocardial strain measurement will be presented at the end of this section.

1.5.1 Magnetization tagging

Following the demonstration of NMR by Bloch et al. [35] and Purcell et al. [36], experiments with flowing liquids were first reported in 1951 by Suryan [37]. He applied a strong B_1 field to magnetized stationary liquid in a fixed volume. The measured nuclear absorption signal was greatly attenuated due to substantial saturation by the B_1 field. However, when he repeated the same experiment on the flowing liquid, the NMR signal increased proportionately with liquid velocity. This velocity-dependent signal arises from the fact that the liquid flowing into the volume of detection carries unsaturated protons. Depending on the flow rate, these "fresh" protons replace different amounts of the saturated protons originally in the volume, and can be nutated by the B_1 field and emit signals proportional to the liquid velocity.

Application of velocity-sensitive NMR to the measurement of blood flow rates *in vivo* has been illustrated in the serial pioneering work of Singer et al.. In 1959, Singer demonstrated that the velocity of blood flow could be determined in terms of three measurements: longitudinal relaxation time T_1, and two signal amplitudes, one with flow and one without flow [38]. He performed the first *in-vivo* NMR measurement of blood flow in mouse tails, measuring T_1 and signal amplitude with tourniquet applied, followed by signal measurement with tourniquet released. He also proposed an MR "time-of-flight" method to measure the blood velocity. This

method consists of one set of transmitter coil located at the upstream that is allowed to demagnetize the proton spins, and the second set of coil at the downstream for monitoring the signal. By estimating the time for the bolus of demagnetized nuclei to reach the monitoring point, the flow velocity is determined.

The first NMR measurement of blood flow in humans was carried out by Morse and Singer (1970) [39]. They used the time-of-flight tagging method to measure blood flow in the median veins of human arms. The key idea is equivalent to the use of radioactive tracers in nuclear medicine to determine the velocity from the transit time of flow. In the NMR experiment, the "tagged" bolus of proton spins was used as the tracer. This method is more straightforward than Singer's previous three-measurement method, and has laid the foundation for the subsequent development of the MR tagging technique used to obtain quantitative images of the blood flow.

Tagging with cardiac MRI for the assessment of myocardial motion was first demonstrated by Zerhouni et al. [40]. This method relies on the persistence of local demagnetization for times on the order of T_1. The magnetization of the tissue is used to produce the signal displayed in MRI, so a local demagnetization results in signal-void markers in the resulting images. The tag planes can be applied orthogonally to the imaging plane, and the intersections between the tag planes and the imaging plane result in dark strips or grids in the image. Since the demagnetized nuclei move with the tissue, any motion between the time of demagnetization and subsequent imaging will be seen as a corresponding displacement of these tagged markers. In general, T_1 of myocardium is about several hundred milliseconds. This allows us to observe the deformation pattern of the tag image over the ejection phase before tagged markers fade away.

To calculate a 3D strain tensor field of the ventricular myocardium, the motion of a 3D grid system constituted by multiple short-axis and long-axis images of tagged grids over the whole ventricle needs to be reconstructed first [41, 42]. With sufficient temporal resolution of the tagged images, each grid intersection point can be tracked from end-diastole to end-systole. Given the motion for these intersection points through time, the corresponding displacement vectors are determined. A 3D displacement field is then obtained using the finite element method to interpolate a smooth displacement function between the adjacent grid points [43]. Finally, any tensor quantity regarding to myocardial kinematics, e.g. deformation gradient or strain tensor can be derived from this displacement field.

MRI strain measurement using magnetization tagging has wide appeal because of its novel and succinct rationale. It has successfully demonstrated the normal pattern of cardiac torsion and its change corresponding to various abnormal conditions. However, the current MRI technique cannot provide a satisfactory spatially resolved data. The spacing of the tagged lines is

approximately 7 mm, limiting its capability to show the transmural variation of the strain component. This limitation also makes study of thin walls such as dilated cardiomyopathy or post-infarct expansion difficult. In human study, the number of imaging slices must be decreased because of limited scanning time, and this will further compromise the spatial resolution of the data. The tagging method requires tracking of the same tagged markers from one scan to the next to provide the displacement data. The decision of the tracked locations near the endocardium is often confounded by the beat-to-beat variation of the endocardial contour, complex geometry of the trabeculae, and flow-related artifacts in the cavity. To overcome this, the current method of data analysis involves subjective guidance, and so is subject to inter-observer variation.

1.5.2 Velocity-sensitive phase shift

The effect of velocity-induced phase shift on the NMR signal was first discussed by Carr and Purcell in 1954 [44]. In their multi-echo experiment to measure transverse relaxation time (T_2) of liquids, they found that even echoes were larger than odd echoes if there was convection flow in the sample. This effect arises from the phase memory of the nuclear-spin Larmor precession. The distances that individual proton spins travel through a magnetic field gradient are inscribed by their accumulated phases. As a result, the ensemble evolution of the phases of the proton spins arrives at perfect refocusing at even echoes, producing larger amplitudes than those of odd echoes. In 1960 Hahn proposed the use of spin echoes to measure coherent motion of the sea water [45]. He derives an important equation which relates the velocity v with the phase shift $\Delta\phi$ of the spins by

$$\Delta\phi = \gamma g v t^2 \ , \qquad (1.1)$$

where γ is the gyromagnetic ratio of proton nuclei, g is the magnetic field gradient, and t is the time between RF pulses, namely a half of the echo time (t = TE/2). This relation established the conceptual basis for the development of phase-contrast MRI in the following decades.

Soon after MRI was manufactured for clinical use, Moran (1982) developed a theory of phase-gradient-modulation technique for phase-encoding velocity [46]. A bipolar velocity-sensitive gradient pair can be interlaced into an already existing MR imaging sequence without interference. Velocity components of the moving tissue are directly encoded as true subject variables of the magnetization to be imaged as the spatial positions of the magnetization are phase-encoded in conventional imaging sequence. From phantom studies, Moran verified the ability of phase contrast MRI to accurately quantify the velocity of the flow [47]. The confirmation of the application to detecting myocardial motion was initially implemented by van Dijk in 1984 [48]. He realized that the existing gradient pair for signal read-out actually phase-encoded the velocity of the moving spins. After off-setting unwanted phases induced by the slice-select gradients, he obtained

the phase image that was directly related to the velocity along the slice-select direction. Color-coded velocity images at different points in the cardiac cycle showed different patterns of spatial velocity distribution that were compatible with physiological motion patterns of the myocardium and the aortic blood flow.

Though velocity is crucial to indicate the functional status of the physiological flow (the blood or cerebro-spinal fluid flow), it is not sufficient to describe the mechanical function of the myocardium. A proper form of describing the mechanical action of the myocardium is the strain tensor; it is a rank-2 tensor constructed from differential displacements between adjacent points. It follows that differential velocities between adjacent points yield the strain-rate tensor. Accordingly, Wedeen (1992) first computed the 2D myocardial strain-rate tensor by taking spatial derivatives of the in-plane velocity components provided by phase-contrast MRI [49]. Since linearization holds for small displacements detected within a short period of velocity-sensitization, strain-rate tensor (**S'**) can be reasonably approximated by a linear combination of the spatial gradient of the velocity, **grad v**, and its transpose, $(\mathbf{grad\ v})^T$:

$$\mathbf{S'} = 1/2\ (\mathbf{grad\ v} + (\mathbf{grad\ v})^T)\ . \qquad (1.2)$$

Using single-shot echo-planar MRI (EPI), a series of strain-rate tensor images at 30 ms. increment through the cardiac cycle can be effectively obtained within 20 min. It shows the temporal evolution of the radial strain rates corresponding to the thickening and thinning action of the ventricular wall in systole and diastole, respectively. Based on this phase-contrast EPI technique, the present work extends the strain-rate measurements from 2D to 3D, and establishes a practical way to integrate the strain-rate properly over the ejection phase to quantify systolic strain.

Though information about myocardial kinematics can be derived from the strain tensor image in terms of coordinate-invariant principal strains or strain components in circumferential, longitudinal, and radial directions (three axes of local cardiac coordinates), these strain patterns only describe the morphological change at the geometrical level. The activities of the underlying fiber or sheet structures, pertinent to the origin of the mechanical function of the myocardium, remain obscure. To gain insight into the role of the myocardial architecture in the mechanical function of the ventricular wall, information about the fiber and sheet orientation at each location must be incorporated. Only by analyzing conjoint information of myocardial structure and function, can some principles governing structure-function relations of the myocardium become evident. For this reason, present study explores the use of diffusion tensor MRI to acquire architectural information in the beating heart. The image of 3D strain is then registered to the image of myocardial structure for studying structure-function relations (later discussed in Chapter 5).

1.6 Myocardial Diffusion Measurement

Self-diffusion in the liquid state arises from translational displacements of constituent molecules due to Brownian motions. To measure self-diffusion, a molecular label is required so that positional change of molecules can be followed through time. Three techniques employing such a molecular label are radioactive tracer measurement, neutron scattering spectroscopy, and pulsed gradient NMR. These techniques differ significantly in their sensitivity to Einstein lengths of molecular diffusion. Tracer measurement is useful for lengths on the scale of millimeters, neutron scattering is for those on the scale of Angstroms. Pulsed gradient NMR probes diffusion lengths ranging from a few microns to hundreds of microns, compatible with the size of cells in biological tissue. Therefore, one important application of pulsed gradient NMR is to investigate the structural features of cellular organization based on the parallel correspondence between diffusion anisotropy and structure anisotropy.

1.6.1 NMR pulsed gradient diffusion measurement

NMR provides a molecular label by imposing a smoothly varying magnetic field over the sample. In this magnetic field, the individual nuclei of each molecule precess with characteristic Larmor frequencies according to their positions. Individual nuclei accumulate precessional phases as they move with molecules and experience different magnetic fields during the measurement. In contrast to the coherent motion of water molecules in the macroscopic flow, molecular translation due to Brownian motion is random in nature. The major difference between these two motions regarding to phase memory of the precessing nuclei is that diffusion is dissipative, and flow is conservative. Consequently, the effect of diffusion is to attenuate the echo amplitude whilst the effect of flow is to shift its phase.

The influence of diffusion on the attenuation of echo signals was noticed and discussed by Hahn in his original paper on spin echoes (1950) [50]. Carr and Purcell (1954) extended Hahn's idea and proposed a multi-echo method to minimize such a diffusion effect [44]. A formal derivation of the diffusion effect on the signal attenuation was carried out by Torrey (1956) who took the "magnetic flow" approach by adding diffusion terms to the original Bloch equations (1946) [35, 51]. Though it is theoretically feasible to measure self-diffusion using conventional spin-echo pulse sequence (90° – TE/2 – 180° – TE/2 – echo) with a magnetic field gradient continuously applied, this sequence suffers from a higher noise due to the increased signal bandwidth. To circumvent this problem, Stejskal and Tanner (1965) proposed that the gradients

could be applied in the form of pulses, one inserted between 90° pulse and 180° pulse, another between 180° pulse and echo (Fig. 1.6) [52]. They also demonstrated a detailed theoretical description of the signal attenuation that generalizes Torrey's equation of the constant-gradient case. The diffusion coefficient (D) is related to the signal attenuation A(TE) / A(0) by:

$$\ln[A(TE) / A(0)] = - \gamma^2 g^2 \delta^2 D (\Delta - 1/3\ \delta) \ , \qquad (1.3)$$

where g is the magnitude of the pulsed gradient, δ is its duration, and Δ is the interval between the pulse pair, i.e., diffusion time.

It is instructive to derive Eq. 1.3 in the limit of $\delta << \Delta$ for it provides a clear picture of the mechanism for diffusion-induced signal attenuation. Assuming pulsed gradients are the only predominant gradients to impose phase shifts to the spins, a spin at position $\mathbf{r}$ gains a phase shift of $\gamma\delta\mathbf{g}.\mathbf{r}$ after 90° pulse (bringing the magnetization to the transverse plane) and the first gradient pulse (imposing the phase shift to the transverse magnetization). During the diffusion time Δ, the spin changes its position from $\mathbf{r}$ to $\mathbf{r}'$ due to molecular translation, resulting in a net phase shift $\gamma\delta\mathbf{g}\cdot(\mathbf{r}' - \mathbf{r})$. The probability for a spin to begin at $\mathbf{r}$ and move to $\mathbf{r}'$ at the time Δ can be described by conditional probability $P_S(\mathbf{r}|\mathbf{r}', \Delta)$ multiplied by function of spin concentration $\rho(\mathbf{r})$. The echo signal $E(\mathbf{g})$ is then the ensemble average of transverse magnetizations with phase terms $\exp[i\gamma\delta\mathbf{g}\cdot(\mathbf{r}' - \mathbf{r})]$ weighted by $\rho(\mathbf{r})\ P_S(\mathbf{r}|\mathbf{r}', \Delta)$:

$$E(\mathbf{g}) = \int\int \rho(\mathbf{r})\ P_S(\mathbf{r}|\mathbf{r}', \Delta) \exp[i\ \gamma\delta\mathbf{g}\cdot(\mathbf{r}' - \mathbf{r})]\ d\mathbf{r}'\ d\mathbf{r} \ . \qquad (1.4)$$

Provided the diffusion time Δ is sufficiently long, $P_S(\mathbf{r}|\mathbf{r}', \Delta)$ is independent of starting position $\mathbf{r}$ and depends only on the net displacement $\mathbf{r}' - \mathbf{r} = \mathbf{R}$. The conditional probability P_S for water molecular diffusion in an anisotropic medium can be represented by a normalized Gaussian as a function of $\mathbf{R}$, Δ, and the diffusion tensor $\mathbf{D}$:

$$P_S(\mathbf{R}, \Delta) = (4\pi\Delta\|\mathbf{D}\|)^{-3/2} \exp[-\mathbf{R}^T\cdot\mathbf{D}^{-1}\cdot\mathbf{R} / 4\Delta] \ , \qquad (1.5)$$

where $\|\mathbf{D}\|$ is the norm of $\mathbf{D}$, i.e., $\|\mathbf{D}\| = (\lambda_{max}\ \mathbf{D}^T\cdot\mathbf{D})^{1/2}$; λ_{max} = the largest eigenvalue of $\mathbf{D}^T\cdot\mathbf{D}$. Substituting Eq. 1.5 to Eq. 1.4, we immediately realize that $E(\mathbf{g})$ is, in fact, the Fourier transformation of the Gaussian $P_S(\mathbf{R}, \Delta)$:

$$E(\mathbf{g}) = \exp[-\gamma^2 \delta^2\ \mathbf{g}^T\cdot\mathbf{D}\cdot\mathbf{g}\ \Delta] = \exp[-4\pi^2\ \mathbf{k}^T\cdot\mathbf{D}\cdot\mathbf{k}\ \Delta] \ , \qquad (1.6)$$

where $\mathbf{k} \equiv (1/2\pi)\ \gamma\delta\mathbf{g}$. The echo signal $E(\mathbf{g})$ derived above has neglected the signal attenuation caused by T_2. Experimentally, diffusion-induced signal attenuation is actually measured by the ratio of the signal with diffusion-sensitizing gradients on to the signal with the gradients off.

It should be held in mind that Eq. 1.6 is derived under the assumption that pulsed gradient acts like an instantaneous spike. The duration of the spike is so short that molecular diffusion during δ can be neglected. In the case of finite δ, the phase term of transverse magnetization should be expressed in an integral form of field gradient, namely, $\exp[i\ \gamma (\int_0^t \mathbf{g}(t')dt')\cdot\mathbf{r}] =$

$\exp[i\ 2\pi\mathbf{k}(t)\cdot\mathbf{r}]$, instead of $\exp[i\ \gamma\delta\mathbf{g}\cdot\mathbf{r}]$. Equation 1.6 can thus be extended as follows:

$$E(\mathbf{g}) = \exp[-\int_0^{\Delta} 4\pi^2\,\mathbf{k}(t)^T\cdot\mathbf{D}\cdot\mathbf{k}(t)\ dt] = \exp[-\ 4\pi^2\,\Delta\ \langle\mathbf{k}(t)^T\cdot\mathbf{D}\cdot\mathbf{k}(t)\rangle_{\Delta}]\ , \qquad (1.7)$$

where $\langle\ldots\rangle_{\Delta}$ denotes time average over the diffusion time Δ, i.e., $\langle\ldots\rangle_{\Delta} = 1/\Delta\ \int_0^{\Delta}(\ldots)dt$. In pulsed gradient spin-echo sequence, evolution of the spatial modulation of the magnetization k(t) and its quadratic counterpart $k(t)^2$ is illustrated in Fig. 1.6. From this diagram, it is readily seen that the time integral of $k(t)^2$ over TE yields $(1/4\pi^2)\ \gamma^2g^2\delta^2\ (\Delta - 1/3\ \delta)$, the attenuation factor of Stejskal-Tanner's equation (Eq. 1.3). It should be emphasized that equation 1.7 can be generalized to the diffusion-attenuation effect as a result of any time-varying spatial modulation of the magnetization during Δ. The implication of this important principle will be invoked in the next section when the effect of tissue stretch on the MR diffusion measurement is considered.

1.6.2 MRI of anisotropic diffusion

The ability of MRI method to measure the self-diffusion coefficient of water molecules was first demonstrated in vitro by Wesbey (1984) [53]. By incorporating the paired-gradient Stejskal-Tanner sequence into conventional imaging sequences, MRI images with the image contrast predominantly weighted by the local tissue diffusivity (diffusion-weighted images) can be obtained. From these images, we can compute apparent diffusion coefficients (ADC) of water, and obtain information about tissue pathophysiology complementary to that contained in usual T_1- and T_2-weighted images.

The character of diffusion anisotropy inherent to materials exhibiting organizational anisotropy has been investigated in NMR diffusion experiments [54-57]. In tissues that have a regularly ordered microstructure, e.g., brain white matter, skeletal, cardiac, and uterine muscles, kidney and lens, the measured ADC of water is also found to vary with tissue orientation [58-64]. It is greatest when the diffusion-sensitizing gradient is applied along the fiber direction, and

smallest when the gradient and fiber directions are perpendicular to each other The most plausible explanation for this phenomenon is that cell membranes and other oriented molecular structures retard water diffusion perpendicular to the fiber tract axis more than water diffusion that is parallel to it. Recognizing this, Moseley et al. (1990) and Douek et al. (1991) suggested that this diffusion anisotropy could be used to determine the orientation of nerve fiber tract within brain white matter [65, 66]. To fully define a 3D orientation of the microstructure, however, a rank-2 diffusion tensor in each voxel of the tissue needs to be determined. Tissue's three orthotropic axes can only be defined by three eigenvectors of the diffusion tensor. For this reason, Basser et al. (1994) proposed a new imaging protocol using a series of NMR pulsed gradient spin-echo experiments to compute an effective diffusion tensor at each voxel. This technique is called MR diffusion tensor imaging [67].

The key procedure of diffusion tensor imaging is to acquire six diffusion-attenuated images by applying six noncollinear diffusion-sensitizing gradients. Given a set of six attenuated images and one unattenuated reference image, inverse algebra can be employed to solve for six components of the diffusion tensor. To illustrate the mathematical construct of this procedure, we rewrite Eq. 1.6 as follows:

$$\ln[A(TE) / A(0)] = - 4\pi^2 \Delta \, \mathbf{k}^T \cdot \mathbf{D} \cdot \mathbf{k} = - \mathbf{b}^T \cdot \mathbf{d} \ , \qquad (1.8)$$

where $\mathbf{d}$ is a column vector containing six components of the diffusion tensor D_{ij}, namely $\mathbf{d} = \{D_{11}, D_{22}, D_{33}, D_{12}, D_{13}, D_{23}\}$; and $\mathbf{b} = 4\pi^2 \Delta \{k_x^2, k_y^2, k_z^2, k_x k_y, k_x k_z, k_y k_z\}$ where $k_i = (1/2\pi) \gamma \delta g_i$, g_i is the component of $\mathbf{g}$ in Cartesian coordinates, i = x, y, z. By varying the directions of the diffusion-sensitizing gradient, we obtain six different signal attenuations (indicated by $\mathbf{a} = \{a_1, a_2, a_3, a_4, a_5, a_6\}$) corresponding to six different $\mathbf{b}$ vectors (indicated by $\mathbf{b}_n$, n = 1,2,...,6). From the measured $\mathbf{a}$ and $\mathbf{b}_n$, we can solve for $\mathbf{d}$ uniquely by

$$\mathbf{d} = \{\mathbf{b}^T_1, \mathbf{b}^T_2, \mathbf{b}^T_3, \mathbf{b}^T_4, \mathbf{b}^T_5, \mathbf{b}^T_6\}^{-1} \cdot \mathbf{a} \ . \qquad (1.9)$$

The capability of diffusion tensor imaging to define 3D orientation of the myocardial fibers was first demonstrated by Garrido et al. in perfused rat hearts [61]. *In-vivo* MR diffusion tensor imaging of the heart is of particular interest because it provides a noninvasive means to assess the organization of myocardial fibers. It is potentially useful in both basic and clinical investigations. However, MR diffusion measurement in the beating heart poses a serious problem due to cardiac and respiratory motion. Since bulk motion from pulsation or respiration is approximately a hundred folds larger than molecular diffusion, the phase shift of bulk motion is predominantly larger than that of diffusion. Any imperfect refocusing of the transverse magnetizations due to bulk motion may cause unwanted signal attenuation comparable to that produced by diffusion. To

overcome this problem, Edelman et al. used a stimulated-echo echo-planar MRI sequence to synchronize the timing of diffusion-sensitizing gradients [68]. The rationale of this technique is that phase information applied during the preparation of the stimulated echoes is preserved over the period between preparation pulse and read-out pulse (the diffusion time Δ). Taking the advantage of this, one can prolong the diffusion time Δ with a tolerable signal loss due to T_1 relaxation, rather than substantial signal loss due to T_2 relaxation. In cardiac diffusion MRI, the diffusion time is prolonged to be exactly one cardiac cycle; two diffusion-sensitizing gradients are placed at the same cardiac phase of successive heart beats (double-gating). In regular heart beats, little bulk motion is phase-encoded by the diffusion sensitizing gradients, and so signal attenuation of the echo is purely from the molecular diffusion.

Though the method of double-gating stimulated-echo echo-planar MRI effectively ameliorates the problem of bulk motion in diffusion measurement of the beating heart, it causes a new problem that was never encountered in previous static diffusion measurements. As pointed out by Reese et al., the problem arises from the spatial modulation of the magnetization, $\mathbf{k}(\mathbf{X}) = (1/2\pi)\,\gamma\mathbf{g}\delta = \mathbf{grad}(\phi)$ [69]. In myocardial tissue that undergoes a deformation $\mathbf{F}(\mathbf{X}) \equiv \partial\mathbf{x}/\partial\mathbf{X} = \mathbf{grad}(\mathbf{x})$, $\mathbf{k}(\mathbf{X})$ is also "deformed" according to the linear mapping: $\mathbf{k}(\mathbf{X}) \rightarrow \mathbf{F}^{-T}(\mathbf{X})\cdot\mathbf{k}(\mathbf{X}) \equiv \mathbf{k}_{eff}(\mathbf{X})$. In other words, spins in the myocardium "see" a time-varying $\mathbf{k}_{eff}$ during diffusion time Δ. Therefore, referring to the generalized form of Eq. 1.7, signal attenuation in this case is the result of the time integral of $\mathbf{k}_{eff}$:

$$\ln[A/A_0] = -4\pi^2\,\Delta\,\langle\mathbf{k}^T_{eff}(t)\cdot\mathbf{D}(t)\cdot\mathbf{k}_{eff}(t)\rangle_\Delta. \qquad (1.10)$$

Substituting $\mathbf{k}_{eff}(t)$ with $\mathbf{F}^{-T}(t)\,\mathbf{k}$, and using polar decomposition: $\mathbf{F}(t) = \mathbf{R}(t)\cdot\mathbf{U}(t)$, we obtain from Eq. 1.10

$$\ln[A/A_0] = -4\pi^2\,\Delta\,\mathbf{k}^T\cdot\langle\mathbf{U}^{-1}\cdot(\mathbf{R}^T\cdot\mathbf{D}_0\cdot\mathbf{R})\cdot\mathbf{U}^{-1}\rangle_\Delta\cdot\mathbf{k}$$

$$= -4\pi^2\,\Delta\,\mathbf{k}^T\cdot\langle\mathbf{U}^{-1}\cdot\mathbf{D}_0\cdot\mathbf{U}^{-1}\rangle_\Delta\cdot\mathbf{k}\ . \qquad (1.11)$$

The only time-independent functions in the Eq. 1.11 are $\mathbf{k}$ and $\mathbf{D}_0$. The last expression in Eq. 1.11 has used the fact that diffusion tensor rotates with the myocardium, i.e., $\mathbf{D}(t) = \mathbf{R}(t)\cdot\mathbf{D}_0\cdot\mathbf{R}^T(t)$, and has assumed that true diffusivity $\mathbf{D}_0$ is independent of tissue stretch. Therefore, the observed diffusion tensor $\mathbf{D}^{obs}$ is related to true diffusion tensor $\mathbf{D}_0$ by:

$$\mathbf{D}^{obs} = \langle\mathbf{U}(t)^{-1}\cdot\mathbf{D}_0\cdot\mathbf{U}(t)^{-1}\rangle_\Delta\ , \qquad (1.12)$$

where $\mathbf{U}(t)$ is the stretch tensor at time t with respect to time t_0.

To correct the effect of stretch on the diffusion measurement, according to Eq. 1.12, one needs to solve for D_0 using stretch tensor history U(t), and the measured D_{obs}. Reese proposed that the history of stretch tensor over a cardiac cycle can be obtained by a motionless movie technique [70]. Motionless movie technique utilizes stimulated echoes to sample temporal evolution of 3D velocity of each pixel in a fixed image. Given velocity data, this stretch tensor history in the material coordinates can be computed by numerical integration. This image is taken at the identical cardiac phase as the time of MR diffusion imaging so that images of $\mathbf{D}_{obs}$ and $\mathbf{U}(t)$ are well-registered. In this way, $\mathbf{D}_0$ in each pixel can be solved for.

Reese's scheme for stretch correction, though theoretically feasible, suffers from large noise and lengthy scanning time. The noise comes from inherently noisy measurement of the stimulated-echo sequence, in particular, when the period between preparation and readout pulses is close to one cardiac cycle. Other noise source comes from the complex computation for stretch correction that may result in large propagated errors. The scanning time for 3D motionless movie at 50 ms temporal resolution may take up to one hour. These problems prohibit accessibility of diffusion tensor imaging in the beating heart. To address this problem, one purpose of the present study is to find an alternative way practical for clinical use; still, it can circumvent the stretch effect on the diffusion measurement and reliably provide the orientations of the underlying fiber and sheet structures (later discussed in Chapter 4).

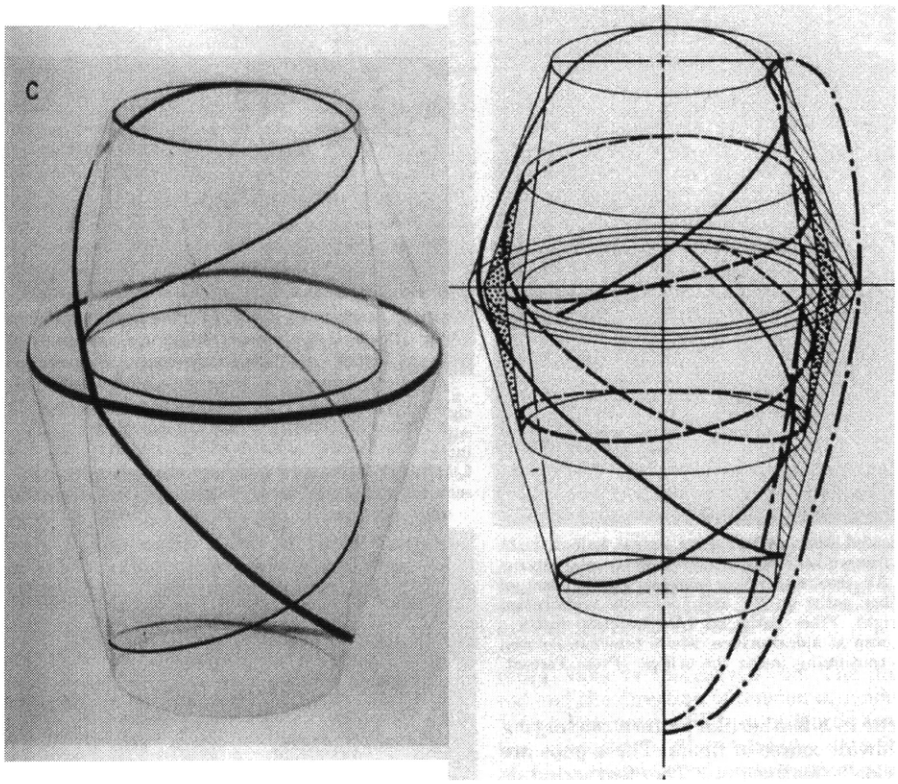

Figure 1.1 Reconstructed fiber pathways on one (left), and two cusped toroidal shells, one nested within the other (right). The paths preserve their geodesic property on the surface of the corresponding shells, and form figure-eight configurations. (From Streeter [16])

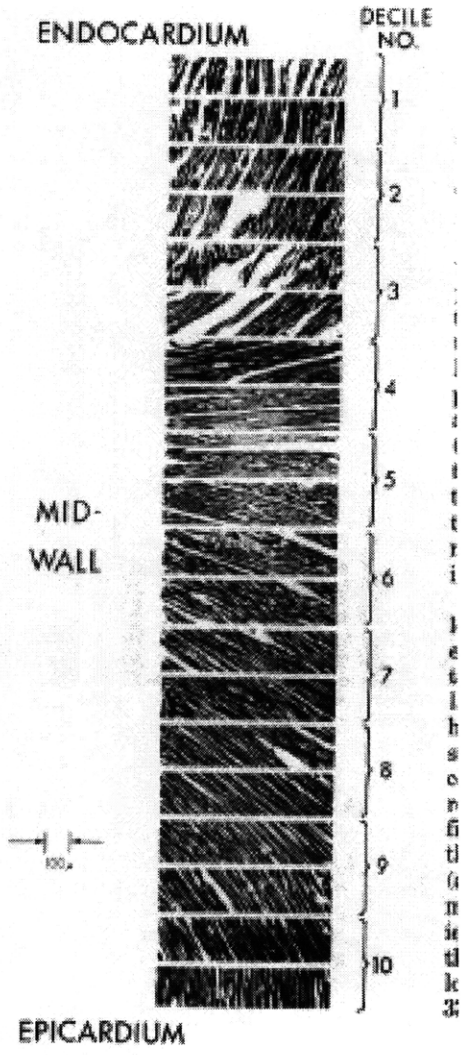

Figure 1.2 Sequence of photomicrographs in epicardial tangent plane, showing gradual change of helix angle through ventricular wall of a canine heart. The helix angle approaches 90° endocardially and -90° epicardially, running through 0° at the midwall, with a range approaching 180°. (From Streeter [16])

Figure 1.3 Transverse section through the human left ventricular free wall at mid-ventricular level (5 x magnification). A feathering pattern of cleavage planes is clearly shown. (From Lunkenheimer et al. [71])

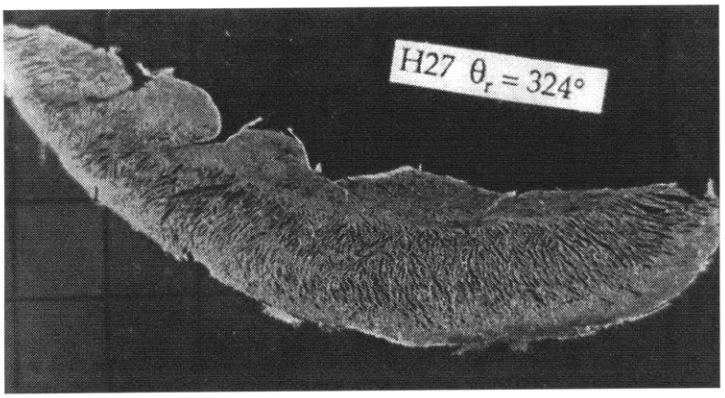

(a)

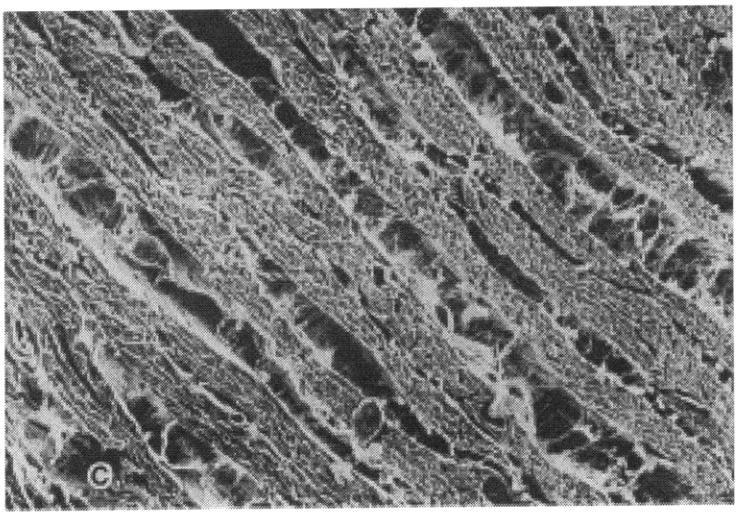

(b)

Figure 1.4 (a) Cross section of LV free wall showing myocardial sheet orientation (From LeGrice et al. [20]). (b) Transverse midwall section of x 145 magnification showing layers of myocyte groups with distinct gaps between them. (From Smaill et al. [72]).

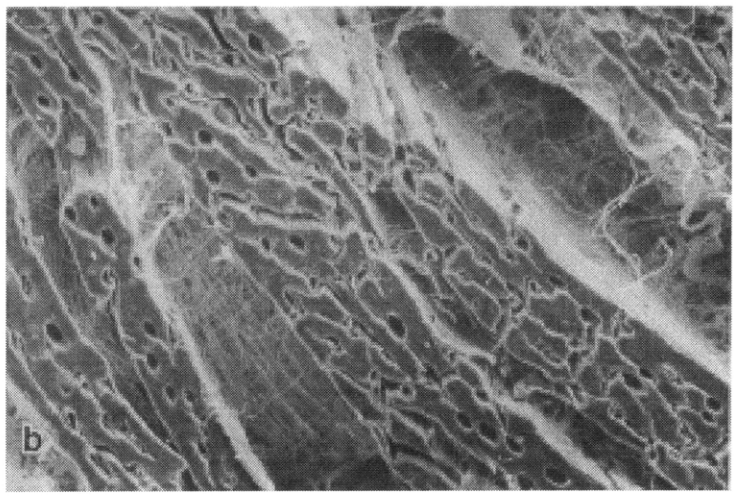

(c)

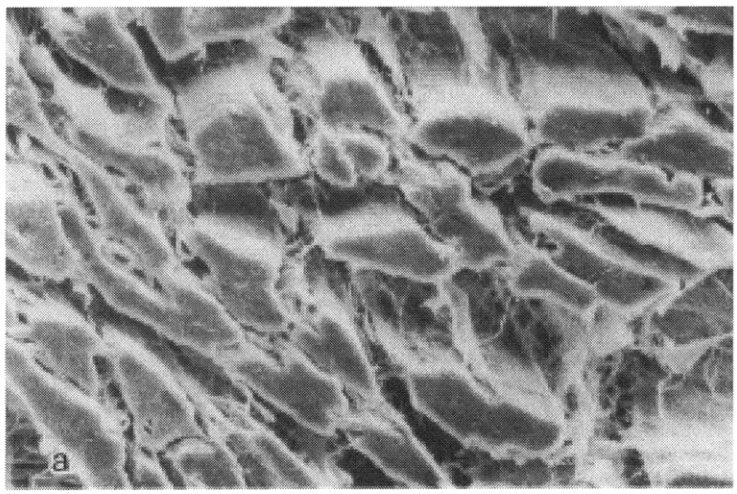

(d)

Figure 1.4 Electronmicrographs of laminar sheet architecture. (c) Groups of myocytes are surrounded by meshwork of connective tissue, x 510; (d) Surrounding individual myocytes, there are radial collagen cords interconnecting with myocytes, x 1050. (From Smaill et al. [72])

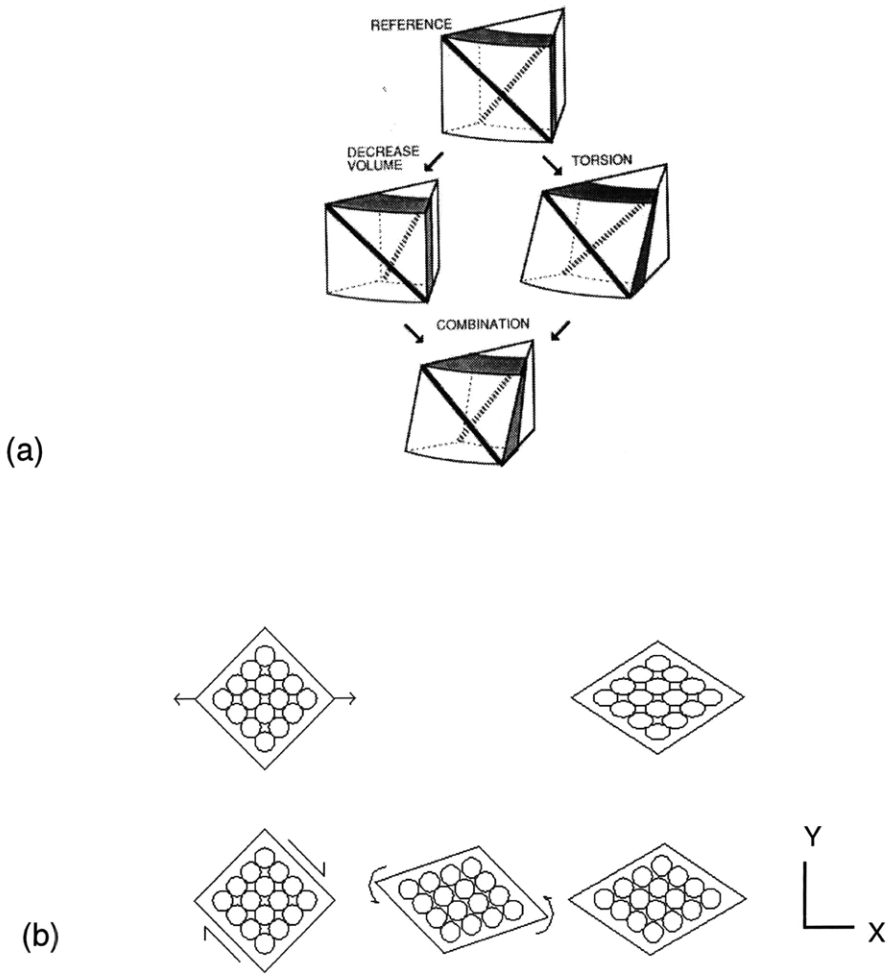

Figure 1.5 (a) Mechanism for smoothing transmural differences in fiber shortening during systole. Starting from the end-diastolic reference state, a decrease in cavity volume without torsion causes more shortening of the subendocardial fibers (hatched bar) than of the subepicardial fibers (solid bar). Pure torsion causes lengthening of the subendocardial fibers at the cost of shortening of the subepicardial fibers. In an appropriate combination of both deformation modes, the transmural distribution of fiber shortening evens. (From Arts et al. [73]). (b) 2D examples of mechanism for wall thickening through sheet slippage. A pure stretch of myocytes (top) cannot account for remarkable systolic wall thickening along x-direction. Instead, a pure shear along $\pm\{1,-1\}$ between layers of myocytes (bottom left) followed by a small rigid body rotation (bottom middle) can explain increased myocyte numbers across the wall during systole.

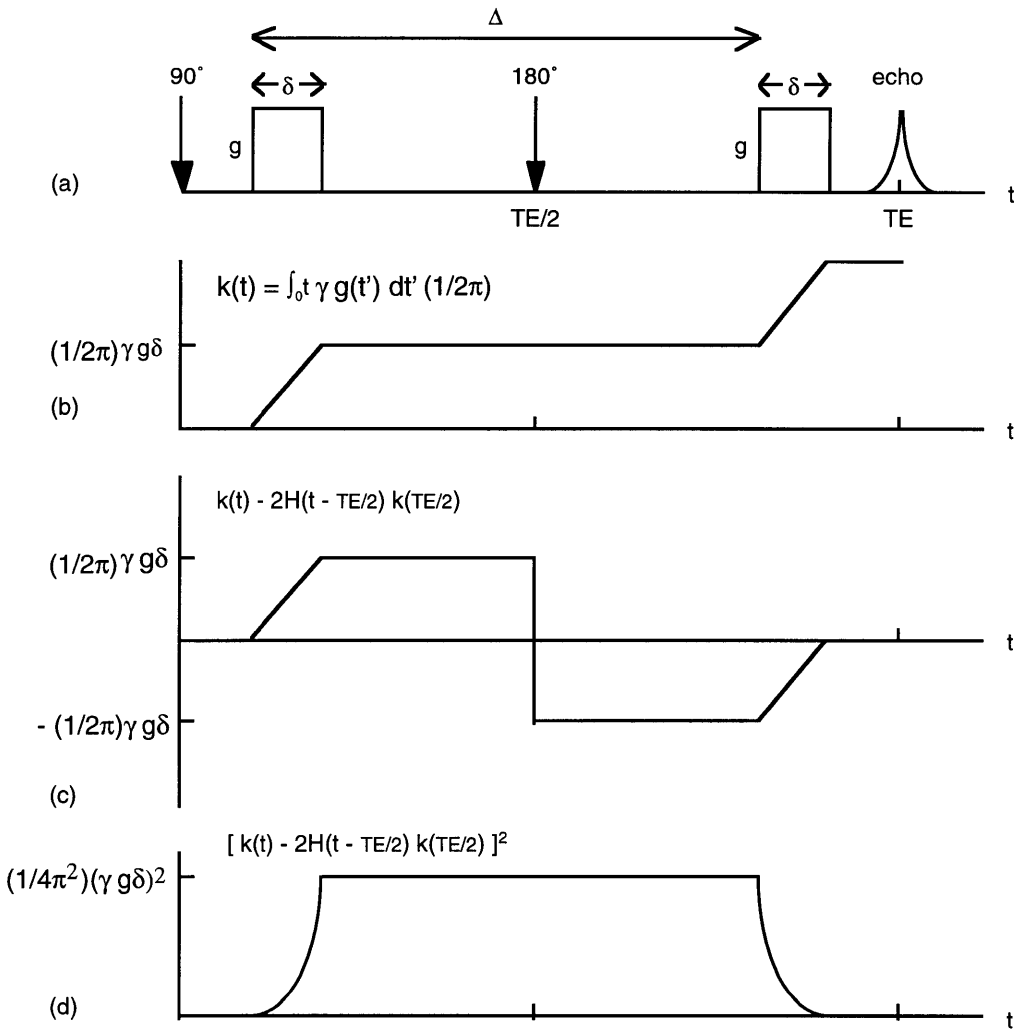

Figure 1.6 Pulsed gradient spin-echo diffusion sequence (a). Diffusion-sensitizing gradients are applied one at the time between the 90° and the 180° RF pulses, another between the 180° RF pulse and the echo. (b) Evolution of k(t) if only 90° were applied. (c) In the spin-echo sequence (90° – 180° – echo),the evolution of k(t) is down shifted by 2 k(TE/2) at the time when the 180° pulse is applied. H(t) is Heaviside function. (d) The square of the evolution in (c) has the time integral = $(1/4\pi^2)\ (\gamma\, g\, \delta)^2\ (\Delta - 1/3\ \delta)$.

Chapter 2

Validation of Diffusion Tensor MRI of Myocardial Architecture

The knowledge of how the fibers are organized in the ventricular wall is crucial to the understanding of engineering design of the heart. Recent advance in cardiac histology has provided an overall picture of the myocardial architecture [17, 74]. Fibers, the basic anatomic unit of the myocardium, wind around the ventricle in a symmetric helical pattern. Adjacent parallel fibers aggregate to form discrete sheet structures which rotate with fibers and stack on one another. At each location of the wall, this fiber-sheet organization constitutes an orthotropic material with three orthogonal axes of symmetry, paralleling fiber, sheet and sheet normal directions.

In parallel with the progress in cardiac histology, MR diffusion tensor imaging has shown its potential to depict internal structures of various tissues without dissection, based on the premise that diffusion anisotropy corresponds to material anisotropy [65, 66]. It is interesting to note that diffusion tensor in the myocardium also manifests an orthotropic property with three distinctly different eigenvalues [70]. This suggests a possible correlation between principal directions of the diffusion tensor and symmetry axes of the fiber-sheet structure.

Therefore, the major goal of this chapter is to validate the ability of MR diffusion tensor imaging to describe fiber and sheet structures in the heart. To provide various sources of evidence for this validation, Chapter 2 is divided into three sections. In Section 2.1, correspondence of the MR secondary diffusion anisotropy with the sheet structure is investigated using direct histologic comparison. In Section 2.2, correspondence of the MR principal diffusion with the fiber structure

is validated by comparing MR results with the known features of the fiber geometry documented in quantitative histology. In Section 2.3, a less familiar sheet architecture was quantified and compared with the state-of-the-art understanding of the sheet structure.

2.1 Correspondence of the MR secondary diffusion anisotropy with the sheet structure

2.1.1 Introduction

Recent progress in quantitative histology made by LeGrice et al. has documented the existence of sheet architecture in the myocardium [20]. This sheet architecture accounts for the well known tissue cracks, called "cleavage planes", observed in the histologic sections; cleavage planes have long been considered important in inducing myocardial cellular rearrangement to facilitate the change of ventricular wall thickness [18, 30]. Our preliminary results show a potential correspondence between MR diffusion tensor image and the sheet architecture. On comparing a diffusion tensor image of our study with a histologic section in the literature [71], planes spanned by the first and the second eigenvectors of the diffusion tensors (Fig. 2.1, right) appeared parallel to the orientations of the cleavage planes of the corresponding areas in the histologic section (Fig. 2.1, left). This prompted us to hypothesize the correspondence between the eigenspace spanned by the first two eigenvectors of the diffusion tensor (1-2 eigenspace) and the myocardial sheets. In this study, we test this hypothesis by comparing MRI and histology of the same myocardial tissue.

To compare 3D orientations between the 1-2 eigenspace of the diffusion tensor and the myocardial sheets, we must address two crucial challenges to the histologic analysis. First, specimens must have relatively unchanged geometric configurations between MRI and histologic sections. However, during the process of histologic fixation, changes in specimen geometry including shrinkage, warping and tearing are inevitable. Because of this fixation problem, our initial attempts to correlate diffusion MRI with registered histology met with limited success. Second, while each histologic analysis provides only 2D data , we need to establish correspondence with the diffusion MRI which provides 3D data for each voxel. Therefore, it requires at least three orthogonal sections of a tissue block corresponding to the same image voxel to reconstruct a 3D orientation of the myocardial sheet [31].

In this study, we propose a practical solution to circumvent the technical difficulties encountered in the histologic analysis: instead of comparing 3D orientation of the myocardial sheet for each tissue block of a voxel size individually, 2D sheet orientations of tissue slabs in orthogonal planes are compared. To do this, we slice the ventricle into slabs of about 5 mm in

thickness, obtain NMR images of these slabs, and compute the intersection of the 1-2 eigenspace of the MR diffusion tensor with the imaging plane at each pixel. These computed intersections are then compared with orientations of the cleavage planes on the cut face of the same slab. By reducing the histologic correlation from 3D to 2D, we avoid the meticulous sectioning procedure required to reconstruct 3D sheet orientation for each tissue voxel. Though different populations of samples are studied in myocardial slabs in different orthogonal planes, three dimensional correlation between secondary anisotropy of the MR diffusion tensor and the myocardial sheets can still be appreciated by studying the statistics of angular errors in different orthogonal planes.

To solve the problem of fixation-induced tissue destruction and deformation, we devise a simple alternative means to obtain the histologically visible cleavage planes by "fingerprinting" cut faces of the myocardium. These ink patterns show with high contrast and resolution the raised detail of the cut face corresponding to the intersection of the myocardial sheet architecture with the cut face. This inking procedure has little distortion on the specimen, making registration and comparison between MRI and histology easier and more accurate.

Using this technique to compare 2D orientations of the cleavage planes between MRI and histology in different orthogonal planes, our aims are to 1) test the hypothesis that the 1-2 eigenspace of the MR diffusion tensor corresponds to the orientation of the myocardial sheet; 2) quantify the accuracy of the diffusion tensor MRI in defining the myocardial sheet orientation.

2.1.2 Methods

We obtained the fresh beef-heart specimens on the day of harvest. The specimens were then sliced into flat slabs of 5 mm in thickness, corresponding to only about 15% of typical beef heart wall thickness. Slices were obtained in mid-ventricular short-axis and long-axis sections which is typical of orthogonal views of myocardial sheet architecture [20, 75]. Each slab was mounted on a rectangular Lucite sheet of 4 x 5" in size and 0.5" in thickness. The top cut face of the myocardium was inked with a wide ink pad and printed onto high-absorbency paper. Following inking procedure, we sandwiched the specimen by covering the top cut face with another Lucite sheet. The top and bottom sheets are bound securely by pieces of scotch tape to avoid inadvertent movement of the specimen. The specimen was then placed flat upon an RF surface coil for MR scanning. Diffusion images of each slab were obtained with in-plane resolution of 3 x 3 mm and the slice thickness set by the 5 mm slab thickness.

The inked images of the visible cleavage planes on the high-absorbency paper were electronically digitized by a scanner (UC1260 UMAX®) at 600 dpi. The digitized images were then magnified and displayed on a computer screen, from which cleavage planes and boundaries of the specimens were traced, and data saved. From the diffusion MRI, the intersection of the 1-2

eigenspace of the diffusion tensor with the imaging plane was computed for each pixel. Data registration of the traced cleavage planes and the computed intersections was accomplished by a 2D-fitting of the boundary landmarks of the digitized image to the NMR diffusion images. The quality of inter-modality correlation was expressed in terms of the statistics of angular errors between corresponding MRI and histologic orientations.

2.1.3 Results

From four cow hearts, we obtained 1 short-axis and 2 longitudinal slabs for study. Figure 2.2, top, demonstrated a digitized image of cleavage planes inked from a cut face of a longitudinal slab. After magnifying and tracing (Fig. 2.2, middle), traced lines and boundaries of the digitized image were registered in accord with the computed intersections and boundaries of the diffusion MRI (Fig. 2.2, bottom). Corresponding to one computed MR intersection at each location of a pixel, the number of traced lines ranged from 0 to 55 depending on variable visibility of the cleavage planes on the specimen. At each pixel. the angular error $\mathbf{e}_i$ between MR intersection, $\mathbf{a}$, and one traced line, $\mathbf{b}_i$, was calculated by

$$\mathbf{e}_i = \cos^{-1}(|\mathbf{a}\cdot\mathbf{b}_i|) \ , \qquad (2.1)$$

where i = 1, ... n, n is the total number of traced lines in the same pixel. Disparity angle histograms of specimen 1 and 2 are shown on the top row of Fig. 2.3, whereas histograms of the whole specimen 3 and its apical portion 3' are shown in the middle row of Figure 2.3. These histograms consistently show a peak population of the disparity angle at about 10°. The total number of MRI pixels and traced lines of the visible cleavage planes recruited for comparison in each specimen, as well as the peak disparity angle and calculated mean are listed in Table 2.1.

	total number of pixels	total number of lines	peak of disparity angle (θ_p)	mean
specimen 1	610	3026	10°	17°
specimen 2	186	1025	9°	22°
specimen 3	894	12498	10°	24°
specimen 3'	461	6024	9°	18°

Table 2.1 Summary of the analysis of disparity angle between MR and optical images.

2.1.4 Discussion

Diffusion anisotropy measured by MRI has been found to correspond to the structural anisotropy of the measured tissue such as cerebral white matter, muscle, kidney, or ocular lens [59-64]. Based on this correspondence, intense interest has been focused on characterizing principal orientation of an anisotropic tissue by computing the leading eigenvector of the measured diffusion tensor; however, structural implication of the other two eigenvectors are often neglected. While the neglect is legitimate for a transversely isotropic tissue, it is an unnecessary loss of information to fully characterize orientations of an orthotropic material such as myocardium. In this study, we verify that secondary anisotropy of the NMR diffusion tensor corresponds to the myocardial sheet structure which, together with the fiber structure, is integral to a complete description of the myocardial architecture.

To investigate the correspondence between secondary diffusion anisotropy and the myocardial sheet architecture, one obvious method is to compare sheet orientations determined by MRI (1-2 eigenspace of the diffusion tensor) with those in histologic sections. However, after several tries with unsatisfactory results, we recognized that there are problems of misregistration and distortion posing crucial challenges to this histologic method. The way of obtaining histologic sections entails two key steps, fixation (tissue is fixated into a plastic block) and slicing (tissue block is then sliced with a microtome). During fixation, cardiac geometry undergoes substantial deformation and shrinkage. This makes slicing along a plane exactly identical to the imaging plane of MRI highly problematic. Mismatch of the MR imaging plane and the sectioning plane results in failure of registration. Further, making thin slices of myocardium with a large in-plane area leads to inevitable tissue tear. Removing, transferring the sliced tissue, and mounting it onto a glass slide further cause unpredictable distortion of the tissue geometry.

To circumvent these problems, in the present study , the novel printing technique is devised. In this new method, the hearts are sliced into 5-mm slabs prior to MRI and optical imaging. This ensures that the comparison between MR and optical images can be made on the same tissue slab; also, this procedure reduces 3D registration problem to 2D automatically. Since both MRI and printing techniques incur little tissue distortion, an inter-modality comparison of cleavage orientations under identical *in-situ* conditions is also secured.

To verify that 1-2 eigenspace of the diffusion tensor corresponds to the myocardial sheet, and to evaluate the accuracy of the NMR diffusion measurement, we calculate the disparity between the tensor intersection and the histologic cleavage plane on the imaging plane. Histograms of disparity angles (θ) from three specimens of more than 15,000 samples show a consistent shape of data distribution: skew with a peak at approximately 10° (Fig. 2.3). To interpret this result and to make an estimate of the accuracy of the NMR diffusion measurement, we will discuss two issues in the following paragraphs: first, possible change in disparity angle statistics by reducing

the measure of sheet orientations from 3D to 2D, second, errors and limitations from the present inking technique.

To understand the nature of our data distribution, we need to go to the 3D case and model a probability of the 3D orientation of 1-2 eigenspace of the diffusion tensor (the third eigenvector of the diffusion tensor) relative to the real orientation of the myocardial sheet (the sheet normal). Let the myocardial sheet normal be a reference vector pointing at the north pole of a unit sphere from the origin. All the possible orientations of the third eigenvector of the diffusion tensor can be modeled as a bunch of vectors clustering around the sheet normal with disparity angles (θ) of 90° in range and its probability conforming to Gaussian distribution. In this model, the mean vector is the same as sheet normal, pointing at the north pole, and the width of the distribution represents the accuracy of the NMR measurement. Moreover, the population of vectors per unit angle depends on the radius of the circle of the same latitude, and the radius of the circle is $\sin(\theta)$. Consequently, the absolute histogram of the disparity angle is a multiplication of a Gaussian function and $\sin(\theta)$. The shape of this histogram is skew symmetric with the location of the peak θ_p related to the accuracy of the NMR measurement, $\sigma = \sqrt{\theta_p \tan(\theta_p)}$ (Fig. 2.3, bottom). Therefore, the model of Gaussian distribution of disparity between the myocardial sheet normal and the third eigenvector of the diffusion tensor in general, accounts for the skew symmetric shape of the histograms in our results.

Now, going back to the 2D disparity angle we measured in this study, it is not the angle between two plane normals (the myocardial sheet normal and the third eigenvector of the diffusion tensor), but the angle of intersections of these two planes with the third plane, i.e., the cut face or the imaging plane. The angle of intersection may vary according to relative orientation of two planes to the third plane which is unknown *a priori*. Though it is impossible to describe how the histogram of 2D disparity angle will change, from the consistency of the histogram pattern observed in our results, we speculate that this change is not large enough to alter the genuine pattern of the 3D disparity angle histogram, but only modifies its relative height with respect to the peak. It follows that we can still infer the accuracy of the NMR measurement from the 2D disparity angle histogram by the location of the peak. The mean location of the peak in three histograms is 9° ± 1°, implying that the error of NMR measurement of the myocardial sheet orientation has a Gaussian distribution with a ±10° width.

In the present inking method, the visibility of the cleavage planes, on the order of 0.1 mm in resolution, has marked regional variations. We found that subendocardial and apical regions have more visible cleavage planes than subepicardial and basal regions (Fig. 2.2, top). This finding is consistent with LeGrice et al.'s systematic investigation on the microscopic sheet structure in the canine heart [74]. Visibility of the cleavage planes affects the quality of correlation in two ways. First, there is a significant part of the area in the specimen, especially in the short-

axis slab, where no distinguishable cleavage planes can be traced. These areas, being excluded from the comparison, might contain microscopic sheets, but the correlation of these microscopic sheets with NMR diffusion measurement cannot not be established in this study. Second, including traced lines in the areas with poor visibility of the cleavage planes results in bad quality of correlation. This effect is demonstrated in Fig. 2.3 by the histograms of specimen 3 where the whole specimen is included for comparison and specimen 3' where only apical portion of the specimen is included for comparison. In contrast to specimen 3, the histogram of specimen 3' shows a marked reduction of the tail population and a significant increase of the peak population with left shift of the mean and peak values from 24° to 18°, and 10° to 9°, respectively. These results suggest that some areas of mismatch are related to poor visibility of the cleavage planes on the inked image.

2.1.5 Conclusion

As a trade-off for lowering the technical difficulties of histologic analysis, the present method is unable to show explicit 3D correlation of the 1-2 eigenspace of the diffusion tensor and the myocardial sheet on a voxel-by-voxel basis. Furthermore, inevitable limitations of the inking technique only allow us to study partial areas of the specimen with visible cleavage planes, and the quality of correlation is also affected by poor visibility of the cleavage planes in some areas. Nevertheless, our results consistently show the peak of disparity angle at approximately 10° in the histograms, corresponding to an approximately 10° width of the random errors in the 3D case. Given that the angular error due to NMR noise is also 10° in the root-mean-square sense, we conclude that the accuracy of the NMR measurement of the myocardial sheet orientation is very close to the noise level.

2.2 Correspondence of the MR principal diffusion with the fiber structure

2.2.1 Introduction

In the previous section, we have tested the correspondence between 1-2 eigenspace of the diffusion tensor and the myocardial sheet structure by comparing MRI and histology of the same myocardial tissue. To circumvent the problems of misregistration and fixation-induced tissue destruction, we sliced the specimen (reducing 3D registration problem to 2D) and compared intersections of 1-2 eigenspace with the imaging plane with cleavage planes on the inked print (having minimal tissue

manipulation). The success of this method hinges on the fact that a planar structure always makes a line intersection with any non-parallel plane; this property allows us to compare 2D orientations of intersections on a common test plane between MRI and histology. This method, however, does not work in correlating the first eigenvector of the diffusion tensor with the fiber orientation because fiber vector only makes a point intersection with a non-parallel plane. In other words, for a given slice, there are mostly end-ons of the fibers, and only a few fibers that are lying within $\pm 10^{\circ}$ to the sectioning plane can be identified by the appearance of parallel tracks [76]. Pixel-by-pixel correlation of the fiber structure between MRI and histology is doomed to encounter insurmountable difficulties. Being unable to make histologic correlation of the first eigenvector of the diffusion tensor and the fiber structure, we turn to the alternative approach: to quantify 3D fiber geometry with MR diffusion tensor imaging and to compare our MR results with known histologic results in animal or cadaver studies.

Fiber geometry has been studied in pigs, canine, guinea pigs, macaques, rats, and human cadavers for almost two decades [12-14, 16, 18, 77]. The understanding of it culminated in Streeter's systematic quantification of the fiber orientation [16]. Experimentally, he excised through-wall blocks from different sites of the LV, prepared sequential sections parallel to the ventricular wall surface or rotated slices about the transmural axis, and measured specific fiber orientations from these tissue sections. By referring local fiber orientation to local orthogonal coordinates (local latitude, longitude, and epicardial surface normal), he specified fiber orientation in terms of two angles: helix angle and imbrication angle (Fig. 2.4). Helix angle was defined as the angle between the local latitude and the fiber that is projected on the epicardial tangent plane (the plane spanned by local latitude and longitude). Imbrication angle was defined as an orthogonal complement to the angle between fiber and the epicardial surface normal. From these studies he reconstructed a clear and simplified picture of the wall fiber paths: fibers are winding around the ventricular wall on a virtual nested set of toroidal shells (Fig. 1.1). This model faithfully describes two basic features of the fiber geometry, 1) helix angle changes smoothly across the ventricular wall from approximately -90° at the epicardium through 0° at the mid wall to approximately 90° at the endocardium; 2) imbrication angle is small but finite, being positive near base, passing zero at equator and becoming negative near apex. These features of fiber geometry are in general true for hearts in different species. Given fiber geometry with such specific features, we claim that if MRI can faithfully reproduce these features, its capability of depicting fiber orientation is vindicated.

The purpose of this study is to test the posit that the first eigenvector of the diffusion tensor corresponds to the myocardial fiber. We test this posit by 1) quantifying orientations of the first eigenvectors of the diffusion tensors in terms of helix angle and imbrication angle; and 2) assessing spatial maps and histograms of these two angles to see whether they convey the same features of fiber geometry observed in quantitative histology.

2.2.2 Methods

Data acquisition

Diffusion tensor imaging study of a freshly isolated normal cadaver heart was performed in a GE/ANMR 1.5 T instrument. The heart was immersed in a jar of normal saline doped with T_1-shortening agent (Gadolinium DTPA). Multiple transaxial images were acquired in contiguous short axis slices of 5 mm thickness and 3 mm in-plane resolution. Stimulated-echo echo-planar MRI pulse sequence was used with diffusion-sensitizing gradient pulses applied in six directions $\{x, y, z\} = \{1, \pm1, 0\}$, $\{0, 1, \pm1\}$ and $\{\pm1, 0, 1\}$. The gradient intensity $\|\mathbf{g}_D\| = 1$ gauss cm^{-1} and duration $\delta_D = 9.6$ ms, corresponding to spatial modulation $\|\mathbf{k}_D\| = 4.1$ mm^{-1} and diffusion sensitivity $b = 4\pi^2 \Delta \|\mathbf{k}_D\|^2 \approx 660$ s mm^{-2} given a mixing time $\Delta = 1$ s. With 16 averages, repetition time (TR) = 2 s, TE = 46 ms, number of slices = 15, scan time ≈ 60 min and myocardial SNR ≈ 35:1 per pixel for the b = 0 and ≈ 20:1 for the b ≈ 660 s mm^{-2} images.

Establishment of local cardiac coordinates in MRI

A complete description of the fiber orientation can be obtained in the local (circumferential, longitudinal and radial) orthogonal coordinate system at any point in the wall. To establish this coordinate system, we adopt a model of truncated confocal ellipsoid shells for the left ventricular geometry. The key is to find the best fitted ellipsoid shells from multiple tomographic images of the whole LV. Once the key parameter, focal length, of these ellipsoid shells is known, prolate spheroid coordinates for each pixel can be uniquely determined from the original Cartesian coordinates. These prolate spheroid coordinates provide information about the latitude, longitude and transmural depth of each point. Consequently, axes of local circumferential, longitudinal and radial coordinates can be defined by taking tangential to polar, azimuthal, and transmural trajectories at each point, respectively.

Multiple transaxial tomographies of MR diffusion tensor imaging of a freshly isolated normal human heart were analyzed. To determine prolate spheroid coordinates for each pixel in the LV, we traced epicardial contours of the LV on each slice, and defined the ventricular axis by linearly fitting the ventricular centroids on each of the slices. The ellipsoids, among which the one that best fits the epicardial surface contour will be chosen, are constrained to a group with their major axes being parallel to the ventricular axis, and centers coinciding with the centroid of the slice with the largest contour diameter. Least square fit was carried out and the ellipsoid that best fitted the epicardial surface contour was chosen. Once the focal length of the best-fitted ellipsoid was determined, any pixel within the LV with given Cartesian coordinates (x, y, z) could be

converted to prolate spheroid coordinates (λ, μ, θ) based on confocal assumption of the left ventricular geometry [78]. The algebra of the conversion from (x, y, z) to (λ, μ, θ) is demonstrated in Appendix A1.

Local radial vector **r** was defined by taking the tangential to the transmural trajectory (a trajectory along λ coordinate line with μ and θ fixed) at each pixel. With the knowledge of the ventricular axis (denoted as a unit vector **j** due base) and the orientation of **r**, circumferential unit vector **c** and longitudinal unit vector **L** at each pixel was obtained by

$$\mathbf{c} = \mathbf{j} \times \mathbf{r} / |\mathbf{j} \times \mathbf{r}|$$

$$\mathbf{L} = \mathbf{r} \times \mathbf{c} / |\mathbf{r} \times \mathbf{c}| \ . \qquad (2.2)$$

In this way we established the local cardiac coordinate system at each point in the wall that is essentially equivalent to the local coordinate system (local latitude, longitude and epicardial surface normal) Streeter used.

Quantification of fiber orientation in local cardiac coordinates

Given the myocardial diffusion tensor field, we identified the first eigenvector with the orientation of the local myocardial fiber vector **f**. The direction of **f** was assigned as the one having a smaller angle to the local circumferential vector **c**.

To quantify the fiber orientation, fiber helix angle α was defined as the angle between **c** and the projection of **f** on the epicardial tangent plane, i.e., **c**-**L** plane. According to the sign convention proposed by Streeter [16], the angle is positive if the projected **f** ($\mathbf{f}_{epi}$) is counter clockwise to **c**, and negative if clockwise. Mathematically, helix angle α with proper sign convention could be calculated as follows

$$\alpha = \arg(\mathbf{f}_{epi} \cdot \mathbf{c} + i\,(\mathbf{f}_{epi} \cdot \mathbf{L})) \ , \qquad (2.3)$$

where i represents the imaginary unit $\sqrt{-1}$.

Imbrication angle β was defined as an orthogonal complement to the angle between **f** and **r**. Also assigning the sign convention for β, it could be calculated by a polar angle of a complex number with real axis along **r** and imaginary axis along $\mathbf{r}_\perp$ ($\mathbf{r}_\perp$ is perpendicular to **r** and lies in the imbrication plane, namely, the plane spanned by **f** and **r**). The imbrication angle β was calculated by

$$\beta = \arg(\mathbf{f} \cdot \mathbf{r}_\perp + i\,(\mathbf{f} \cdot \mathbf{r})) \ , \qquad (2.4)$$

where $\mathbf{r}_\perp$ was determined by normalizing $(\mathbf{r} \times \mathbf{f}) \times \mathbf{r}$.

2.2.3 Results

A total of 15 transaxial tomographies of diffusion tensor MRI were obtained with 3 x 3 x 5 mm spatial resolution and 7 mm gap along slice selection. The ellipsoid that best fitted the epicardial contours, shown in Fig. 2.5, was found to be 54 mm in focal length. Local longitudinal and radial vectors at each pixel are shown in Fig. 2.6 in four selected slices. It is easy to see that as the slice level approaches base/apex, longitudinal vectors gradually tilt inward/outward and radial vectors gradually tilt upward/downward according to the ellipsoid geometry.

Spatial maps of fiber orientations are color-coded according to fiber helix angle (Fig. 2.7, top). The helix angle maps show a rather circularly symmetric pattern and vary little from apex to base. Consistent with Streeter's finding, helix angle maps demonstrate a classic smooth transmural progression from high positive values subepicardially (left-handed helix) through zero in the midwall (circumferential orientations) to high negative values subendocardially (right-handed helix). The helix angle histogram (Fig. 2.7, bottom left) looks like a broad pyramid in shape, achieving maxima near 0° (fibers of circumferential orientation) and declining symmetrically toward minimal at the densities around +/- 90°. The proportion of circumferential fibers is 38% at equator and 31% near apex. The mean (± SD) equals $4^\circ \pm 47^\circ$.

Spatial maps of the color-coded imbrication angle show a specific geometric pattern (Fig. 2.8, top). In general, there is a systematic shift of the mean imbrication angles of each slice from apex to base: negative ($\approx$-13°) at apex, crossing zero at mid-ventricle and positive at base ($\approx$13°). Linear regression of the mean imbrication angle versus distance along z-direction (apex-to-base direction) shows a slope of 3.7°/cm with regression coefficient $r^2 = 0.93$ (Fig. 2.9). The regions of positive imbrication angles are mainly at anterior and lateral free wall near base, and posterior aspect of interventricular septum around RV insertion, whereas negative imbrication angles are mostly distributed at posterior wall near apex, and the anterior aspect of interventricular septum around RV insertion. Histogram of the imbrication angle shows a symmetric Gaussian-like distribution with mean (± SD) equaling $0^\circ \pm 21^\circ$ (Fig. 2.8, bottom left).

2.2.4 Discussion

Though it is natural to posit that the direction of the maximum water mobility parallels myocardial fiber direction, a quantitative validation is still needed. The attempt to make histologic comparison in the myocardium, however, encounters an extraordinary difficulty in experimental techniques. To circumvent this problem, we turn to the known fiber geometry features observed in quantitative histology, and see whether or not MR diffusion tensor imaging can reproduce the same features. Our results show that the orientation field acquired from the first eigenvectors of the diffusion

tensors faithfully reveal the spatial characteristics of the fiber helix angles and imbrication angles. Furthermore, these spatial maps provide some detailed information about the fiber geometry that had not been discovered before. In the following paragraphs, we will list the findings we obtained from the diffusion tensor imaging that are consistent with known fiber geometry, and discuss the differences.

Spatial distribution and histogram of the helix angles (Fig. 2.7). present three independent features that are consistent with histologic observation [16]. First, helix angles vary from about -90° (left handed helix) at epicardium through 0° at mid wall to about 90° (right handed helix) at endocardium. Second, this transmural variation is circularly symmetric, varying little from apex to base. Third, histogram is symmetric with predominant portion of fibers and balance achieved by right handed and left handed oblique fibers. The only difference is our reported proportion of circumferential fibers, 35% at mid ventricular level and 31% at apical level, which are smaller than Streeter's results of 47% at equator and 38% at non-equatorial sites [16]. This discrepancy arises from the fact that in Streeter's study of normal cadaver hearts, free trabeculae were excluded, so the proportion of circumferential fibers is relatively larger than our results. The exclusion of free trabeculae also resulted in imbalance between right handed and left handed oblique fibers that he admitted was an artifact. Our MR diffusion tensor imaging clearly shows that free trabeculae and papillary muscles are the continuum of the fiber geometry, constituting the inner vertical layers to complete the full spectrum of the fiber orientation.

In spatial maps and histogram of the imbrication angle (Fig. 2.8 and 2.9), there are two independent features consistent with histologic observation [16]. First, average imbrication angles vary from positive (≈13°) at base through zero at mid-ventricle level to negative (≈-13°) at apex. Second, imbrication angles are small and finite, manifesting a sharp histogram with ±20°. The presence of apex-to-base transition of the imbrication angles is consistent with Krehl's Triebwerk model of fiber geometry, that is, fiber continuum conforms to figure-eight loop pathways that pass from epicardium to endocardium near apex and connect back to epicardium near base [6]. Because fibers need to roll over epi-to-endo and vice versa, imbrication angle must be positive toward base and negative toward apex.

Actually, our spatial maps of imbrication angles reveal a more complicated geometric distribution that had never been noticed before. While there is a systematic shift of the imbrication angle from apex and base, two major exceptions of this general transition are observed in interventricular septum around anterior and posterior RV insertions. These exceptions may result from retention of fetal myocardial architecture in which the septal circumferential muscle is continuous with the right ventricular free wall [79]. This finding suggests that Krehl's model may not be valid for describing fiber geometry in interventricular septum.

As Streeter emphasized, "the orientation of the fiber cannot be divorced from the shape of the wall" [16]; it is important to appreciate the need for characterizing fiber orientation in the local coordinate system. As the location in the ventricle changes, local axes rotate in accord with the change of local cardiac geometry. Because of this local property, a consistent quantification of the fiber orientation independent of cardiac geometry can be made at different locations in the heart. Cardiac geometry also varies at different times in the cardiac cycle and differs from one heart to another. Comparison of fiber orientation pattern between different time points or different hearts can only be made if appropriate local cardiac coordinates are established for individual cardiac configurations.

Recently, local cardiac coordinates have been established using finite element method [80]. With sufficient number of meshes, finite element method can model realistic ventricular geometry with a higher precision. However, there is an essential issue being neglected. The ventricular axis has always been assumed to be a line drawn from apex to the center of the largest minor axis of the LV, or to the mid point of base [78, 81]. This anatomic axis is different from the symmetry axis of the circumferential fibers (functional axis). In cadaver hearts, Streeter found that the difference between these two axes was within noise level in contracted state, but the difference increased significantly in dilated state [78]. We also calculated the functional axis in our study and found that it deviated from the anatomic axis by less than 10°. Therefore, we did not adjust our angle measurement according to this deviation. However, we expect that larger angular error will arise in the dilated or diseased heart if local cardiac coordinates are established purely by wall geometry. The correction can be made by determining the orientation of the functional axis relative to the anatomic axis, and applying rigid body rotation to the original local cardiac coordinates according to the orientation of the deviation.

To estimate the accuracy of the diffusion tensor MRI in defining the fiber direction, numerical simulation was performed on the current diffusion data by randomly adding a Gaussian noise with a width the same as the background noise. Principal diffusion at each pixel was recalculated and compared with the original one. The root-mean-square of the angular error was approximately 10°.

2.2.5 Conclusion

Myocardial fiber architecture, including fiber and sheet organizations, bears important relation to the cardiac function. A simple and clear characterization of the fiber architecture has been successfully obtained by MR diffusion tensor imaging in the normal cadaver. This achievement opens a door to investigating architectural change in diseased hearts, as well as the structure-function relationships of the ventricular wall. From these studies, deeper understanding of engineering design of the myocardial architecture will be obtained.

2.3 Mapping of Sheet Orientations Using MR Secondary Diffusion Anisotropy

2.3.1 Introduction

In previous sections, we quantified helix and imbrication angles of the fibers by measuring orientations of the first eigenvectors of the diffusion tensors. The results were in accord with those observed in quantitative histology. We also verified that 1-2 eigenspace of the diffusion tensor corresponded to the myocardial sheet structure. This opens an opportunity for us to investigate sheet orientations in normal cadaver hearts, the pattern of which has not been fully characterized yet. In this section, we will quantify and map sheet orientation over the whole LV. The distribution features will be analyzed and compared to recent published findings in histology. The goal is to obtain distribution characteristics of this less familiar sheet architecture, as well as to substantiate validation of MR diffusion tensor imaging of myocardial sheet structure.

While 3D fiber orientation can be uniquely defined by helix and imbrication angles, the orientation of sheet, being subordinate to the fiber, is greatly confounded by the fiber orientation. Due to a large variation of the fiber orientation across the wall, these sheets swirl with the fibers and become a stack of twisted laminae. Because of this, the meaning of sheet angle is obscure when one tries to define it in local cardiac coordinates. Current histologic analysis defines sheet orientation as an angle subtended by the sheet vector and the radial vector [74]. This definition was made based on the assumption that fiber imbrication angle is zero. However, we have shown that average imbrication angle varies from approximately -15° at apex through 0° at mid-ventricle to 15° at base. The validity of this definition is thus limited at mid-ventricle levels only. To characterize sheet orientation over the whole ventricle, we propose to define sheet orientation in the coordinates that are tied to the fiber-sheet structure (structural coordinates). In this way, quantification of real sheet angle, which is immune to confounding fiber orientation, can be obtained.

The specific aims of this study are to 1) propose a more general definition of the sheet angle that takes into account 3D fiber orientation; and 2) quantify and map sheet orientation over the LV, and compare its distribution pattern with recently published reports.

2.3.2 Definition of sheet angle

Three-dimensional orientation of the fiber has been uniquely defined by helix (α) and imbrication (β) angles. However, to completely define 3D orientation of the fiber-sheet structure, another degree of freedom (sheet angle γ) indicating orientation of the sheet is needed. Because of the confounding effect from the fiber orientation, the definition of the sheet angle can only be clearly

appreciated by a transformation from local cardiac coordinate axes (circumferential **c**, longitudinal **L** and radial **r**) to material coordinate axes given by fiber (**f**), sheet (**s**) and sheet normal (**n**). The transformation from (**c**, **L**, **r**) to (**f**, **s**, **n**) is accomplished by three successive right-hand rotations (Fig. 2.10): $\mathbf{R}_1$: a rotation about **r** by helix angle α which transforms (**c**, **L**, **r**) to ($\mathbf{f}_{epi}$, **L'**, **r**); 2) $\mathbf{R}_2$: a rotation about **L'** by imbrication angle β which transforms ($\mathbf{f}_{epi}$, **L'**, **r**) to (**f**, **L'**, **r'**); and 3) $\mathbf{R}_3$: a rotation about **f** by $\pi/2 - \gamma$ which transforms (**f**, **L'**, **r'**) to (**f**, **s**, **n**). This transformation can be described as a matrix multiplication:

$$(\mathbf{f} \mid \mathbf{s} \mid \mathbf{n}) = \mathbf{T} \cdot (\mathbf{c} \mid \mathbf{L} \mid \mathbf{r}) \quad , \tag{2.5}$$

where (. | . | .) indicates a 3 x 3 matrix with three columns divided by "|", and **T** is a multiplication of three rotational matrices $\mathbf{R}_1, \mathbf{R}_2, \mathbf{R}_3$, namely, $\mathbf{T} = \mathbf{R}_3 \cdot \mathbf{R}_2 \cdot \mathbf{R}_1$. The expressions of three rotation matrices in local cardiac coordinates are listed in Appendix A2.

The key point implied in the above transformation is that the sheet angle γ can only be defined with **f** as an axis of rotation. In other words, a correct quantification of sheet orientation cannot be obtained without **f**. Current method quantifies sheet orientation as the angle (γ') subtended by **s** and **r**:

$$\gamma' = \cos^{-1}(\mathbf{s} \cdot \mathbf{r}) \quad . \tag{2.6}$$

This definition makes $\gamma' = \gamma$ only when **f** is perpendicular to **r** ($\beta = 0°$). The value of γ' calculated by Eq. 2.6 actually varies with β, so it is not an independent parameter for sheet orientation.

To quantify real sheet orientation, we define a sheet angle (γ'') as an angle subtended by **s** and a projected **r** on the **s**-**n** plane. The value of γ'' can be calculated by the polar angle of this projected **r** ($\mathbf{r}_p$) on the complex plane with **s** as the real axis and **n** as the imaginary axis:

$$\gamma'' = \arg(\mathbf{s} \cdot \mathbf{r}_p + i\,(\mathbf{n} \cdot \mathbf{r}_p)) \quad . \tag{2.7}$$

With this new definition, sheet angle is defined with **f** as an axis of rotation, and therefore, γ'' is not affected by the orientation of **f**.

To test the accuracy of two definitions of the sheet angle (Eq. 2.6 and Eq. 2.7), a numerical calculation was performed by varying the helix, imbrication and sheet angles of (**f**, **s**, **n**) systematically over physiological ranges. Equations 2.6 and 2.7 were then applied to calculate the respective sheet angles, namely, γ' and γ'', and their deviations from real sheet angle γ were calculated. The numerical results (shown in Fig. 2.11) are summarized as follows: 1) both definitions are not affected by the helix angle; 2) for a given real sheet angle γ, γ' varies with the imbrication angles. The worst case occurs when $\gamma = 0°$ ($\gamma - \gamma' = \beta$), whereas when $\gamma = \pm 90°$, no error occurs ($\gamma' = \gamma$); 3) γ'' always equals γ despite variation of imbrication angles. From the above results, we conclude that Eq. 2.7 is an appropriate definition for quantifying the real sheet angle.

2.3.3 Methods

We analyzed multiple transaxial diffusion tensor MRI of a freshly isolated normal human. Local cardiac coordinates (**c**, **L**, **r**) established by prolate spheroid fit of the epicardial contours were obtained from Section 2.2. Sheet vector **s** was identified by the second eigenvector of the diffusion tensor $\mathbf{d}_2$ that formed an angle less than 90° to the radial axis, i.e., $\mathbf{s} = \text{sign}(\mathbf{d}_2 \cdot \mathbf{r})\ \mathbf{d}_2$. Sheet normal **n** was determined by $\mathbf{n} = \mathbf{f} \times \mathbf{s}$. After determining these base vectors of the material coordinates, (**f**, **s**, **n**), sheet angle was calculated using Eq. 2.7. Spatial maps and histograms of sheet angles over the whole LV were produced, and the characteristics of the sheet distribution were analyzed.

2.3.4 Results

Three dimensional orientation of the sheet structure at each pixel is rendered by a disc with faces coinciding with 1-2 eigenspace of the diffusion tensor . A mid-ventricle slice of sheets viewing from base to apex is shown in Fig. 2.12. It is obvious that top faces of the discs at the septum are oriented toward the left ventricular cavity, but those at the free wall are oriented opposite to the cavity. This unique sheet orientation pattern accounts for the reversal of sheet signs in the septum versus free wall.

To see the spatial distribution of the sheet angles, sheet angle maps are displayed with gray-level scales indicating the directionality and the magnitude of the angle (Fig. 2.13, top). With 0° and ±90° set at mid-gray, positive angles have lighter gray levels with maximum (pure white) at 45°, while negative angles have darker gray levels with minimum (pure black) at -45°. Sheet angle maps show a distinct geometrical distribution of the sheet angle signs: positive sheet angles are mainly distributed over septum and basal levels, whereas negative sheet angles are mainly at the free wall and apical levels. At the mid-ventricle level, a polarization pattern with negative sheet sign in the free wall and positive sheet sign in the septum is clearly seen. This polarization pattern gradually disappears as transaxial sections move away from the mid-ventricle level: positive sheet sign dominates toward base, whereas negative sheet sign dominates toward apex.

Sheet angle histogram (Fig. 2.13, bottom) shows a bimodal pattern; the sheet angle distribution can be decomposed into two distinct populations of opposite signs. The positive bump represents the angle distribution at the septal side with the peak at 23° and with the mean(± SD) = 26° ± 25°. The negative bump is the distribution at the free wall side with the peak at -20° and with the mean(± SD) = -23° ± 26°.

2.3.5 Discussion

Sheet angle has been measured under the assumption that fibers are strictly lying on the epicardial tangent plane ($\beta = 0^{\circ}$). This assumption limits sheet angle measurement to be accurate only at mid-ventricle levels where fiber imbrications are close to 0°. In this section we proposed a new definition of the sheet angle, and showed in the numerical calculation that this definition accurately measured the real sheet angle despite fiber orientations. Using this definition, we were able to quantify sheet orientation at any location of the LV and to obtain an overall orientation pattern of the sheet structures. A unique bimodal distribution of the sheet angles was discovered with positive angles mainly at the septum and basal region, and negative angles mainly at the free wall and apical region. In the following paragraphs, we will relate our sheet orientation pattern to the reported histologic findings. Some limitations in quantifying sheet orientation will also be discussed.

The major feature of our sheet angle maps is reversed sheet sign with positive mainly at septal-to-base region and negative mainly at free wall-to-apex region. This feature is consistent with sporadic findings in quantitative histology. In the investigation of the relationship between myocardial architecture and the wall strain, Costa measured sheet morphology at four sites of the canine LV: base, apex, mid-anterior free wall, and mid-septum [82]. From the average-fitted transmural distribution of the sheet angles, he showed that the sheet angles at the apical and mid anterior sites were predominantly negative while those in the septal and basal sites were mostly positive. A marked reversal of sheet signs at inner walls of interventricular septum versus anterior free wall was also noticed by LeGrice et al. [31], who made use of this fact to study structural correlation of the shear deformations in these two areas. Recently, the same authors used systematically sampled data of sheet architecture and the finite element method to interpolate sheet orientations over the whole heart [74]. They reported that the transmural pattern of sheet orientations in the septum is exceptionally different from those in left and right ventricular free walls. Septal sheets are oriented in the opposite sense to those in the free wall. This statement, according to our sheet angle maps, is particularly true at mid-ventricle levels. The consistency of our results with current histologic findings supports the ability of MR diffusion tensor imaging to depict myocardial sheet architecture.

Owing to the difficulty of assessing myocardial architecture, quantitative histology can only study sheet morphology at a few selective sites in the ventricle. The polarization pattern of sheet angles and how it evolves from base to apex requires comprehensive sampling of the sheet orientation throughout the whole LV. For this reason, this unique characteristic of the sheet pattern has not been documented yet. With MR diffusion tensor imaging, we can easily obtain more comprehensive and detailed information about sheet architecture. Our sheet angle map is the first

presentation of an overall picture of the sheet orientations and clearly shows this polarization pattern and its apex-to-base transition.

The credibility of our sheet angle map hinges on an appropriate definition of the sheet angle (Eq. 2.7). In this definition, sheet angle is defined in the material coordinates where fiber, sheet and sheet normal are the base axes. The measurement of the sheet angle, therefore, not only requires sheet and radial directions at each myocardial location, it also requires knowledge of fiber orientation. The requirement of knowing both fiber and sheet orientations at the same location is extremely difficult to attain in quantitative histology because, in general, only one angle can be determined in one particular tissue section at each point. On the other hand, MR diffusion tensor imaging provides all the information required at each point in a single study, and the accurate sheet angle defined by Eq. 2.7 can be readily computed.

It should be noted that our definition of sheet angle has two limitations: 1) singularity occurring at imbrication angle $\beta = \pm 90^\circ$; and 2) possible aliasing in some sheet angles. The first limitation arises from the fact that as the fiber approaches the radial direction ($\beta = \pm 90^\circ$), the component of **r** projected on **s**-**n** plane becomes smaller, so the direction of the projected **r** becomes more ambiguous due to data noise. Given a $\pm 15^\circ$ rms error of α from MR measurements, the uncertainty of projected **r** is greater than $\pm 30^\circ$ when $|\beta| > 60^\circ$. This limitation, however, is considered minor because most of the imbrication angles are within $\pm 20^\circ$. The probability that imbrication angles exceed $\pm 60^\circ$ is extremely rare.

The second limitation is due to the way we identify the sheet vector. The sheet vector is identified to be the second eigenvector of the diffusion tensor that forms an angle less than 90° to the radial axis. This assignment is based on the premise that sheet angles are mostly oriented in the radial direction ($|\gamma| \leq 30^\circ$). From our sheet angle histogram, a significant amount of sheet angles exceeds $\pm 45^\circ$. Three-dimensional rendering of the sheet structure (Fig. 2.10) clearly shows that sheet orientations vary smoothly across the vertical direction ($\gamma = \pm 90^\circ$) in the mid-septum. However, in this transitional zone, sheet vectors have to be flipped because of current assignment, and result in abrupt change in gray levels of adjacent pixels. To ameliorate this aliasing problem (sheet vectors flip abruptly across the junctional zone), we assign the gray level of the sheet angle to be maximum/minimum at 45°/-45° , passing through mid-gray at 0° and $\pm 90^\circ$. With this gray-level assignment, the sheet vectors that are artificially flipped at the $\pm 90^\circ$ junction can still present smoothly varying gray scale.

The accuracy of the measured sheet angle depends on the noise from the MR experiment. Routine MR diffusion tensor imaging yields $\approx$ 45:1 and $\approx$ 25:1 signal-to-noise ratios for unattenuated and attenuated images, respectively. Under this condition, the accuracy of the sheet angle was evaluated by Gaussian noise simulation. It is approximately 15° in the root-mean-square sense.

2.3.6 Conclusion

The ability of diffusion tensor MRI to depict myocardial sheet architecture is vindicated by presenting sheet orientation features that are consistent with recent reported findings in quantitative histology. Moreover, because of the advantages of noninvasiveness and persuasiveness, MRI provides us complete information on fiber-sheet structure at each location in the myocardium. This allows us to obtain more accurate and comprehensive mapping of sheet orientations, and to document the unique polarization sheet pattern in the LV.

Appendix A.1 Calculation of prolate spheroid coordinates from rectangular Cartesian coordinates

A material point in the left ventricular myocardium described by the prolate spheroid coordinates (λ, μ, θ) has rectangular Cartesian coordinates

$$\begin{aligned} x &= a \cosh \lambda \cos \mu \\ y &= a \sinh \lambda \sin \mu \cos \theta \\ z &= a \sinh \lambda \sin \mu \sin \theta \end{aligned} \qquad \text{(A.1)}$$

where a is the location of the focus on the x-axis, as shown in Fig. 2.10. The λ-coordinate is directed transmurally, the μ-coordinate runs azimuthally from apex ($\mu = 0$) to base along an elliptical path, and the θ-coordinate runs circumferentially from y-coordinate ($\theta = 0$). Given (x, y, z) and a for a material point, we want to solve for (λ, μ, θ) using Eq. A.1. The polar coordinates θ of the material point can be determined readily by:

$$\cos \theta = y / (y^2 + z^2)^{1/2} \ . \qquad \text{(A.2)}$$

The azimuthal μ and transmural λ coordinates can be solved simultaneously as follows. Summation of the squared terms on either side of Eq. A.1 results in the following identity:

$$x^2 + y^2 + z^2 = a^2 (\cos^2 \mu + \sinh^2 \lambda) \ . \qquad \text{(A.3)}$$

To express $\cos^2 \mu$ in terms of (x, y, z) and a, a set of identities in the prolate spheroid is employed:

$$\begin{aligned} \cos^2 \mu &= x^2 / m^2 = x^2 / (a^2 + n^2) \\ \sin^2 \mu &= (y^2 + z^2) / n^2 \end{aligned} \qquad \text{(A.4)}$$

where m and n are the lengths of the major and minor axis of the ellipsoid. With some algebra we obtain from Eq. A.4

$$\begin{aligned} \cos^2 \mu &= 1/2 \, (R - (R^2 - 4 x^2 / a^2)^{1/2}) \quad \text{where} \\ R &= (x^2 + y^2 + z^2 + a^2) / a^2 \ . \end{aligned} \qquad \text{(A.5)}$$

Using Eq. A.3 and A.5, μ and λ can be solved for simultaneously.

Appendix A.2 Three rotation matrices for transformation from local cardiac to structural coordinates

The expressions of three rotation matrices ($\mathbf{R}_1$, $\mathbf{R}_2$, $\mathbf{R}_3$) in local cardiac coordinates are:

$$\mathbf{R}_1 = \begin{pmatrix} \cos\alpha & -\sin\alpha & 0 \\ \sin\alpha & \cos\alpha & 0 \\ 0 & 0 & 1 \end{pmatrix};$$

$$\mathbf{R}_2 = \begin{pmatrix} \cos^2\alpha\cos\beta + \sin^2\alpha & -\sin 2\alpha \sin^2(\beta/2) & \cos\alpha\sin\beta \\ -\sin 2\alpha \sin^2(\beta/2) & \cos^2\alpha + \cos\beta\sin^2\alpha & \sin\alpha\sin\beta \\ -\cos\alpha\sin\beta & -\sin\alpha\sin\beta & \cos\beta \end{pmatrix}. \qquad \text{(A.6)}$$

For the sake of clarity, the expression of $\mathbf{R}_3$ is listed component-wise in the form $R_3(i,j)$, indicating a component at i-th column and j-th row.

$$R_3(1,1) = \cos^2\alpha\cos^2\beta + (1 - \cos^2\alpha\cos^2\beta)\cos(\pi/2 - \gamma)$$

$$R_3(1,2) = \cos^2\beta\sin\alpha\cos\alpha - \cos^2\beta\cos(\pi/2 - \gamma)\sin\alpha\cos\alpha + \sin\beta\sin(\pi/2 - \gamma)$$

$$R_3(1,3) = -\cos\alpha\sin\beta\cos\beta + \cos\alpha\cos(\pi/2 - \gamma)\sin\beta\cos\beta + \cos\beta\sin\alpha\sin(\pi/2 - \gamma)$$

$$R_3(2,1) = \cos^2\beta\sin\alpha\cos\alpha - \cos^2\beta\cos(\pi/2 - \gamma)\sin\alpha\cos\alpha - \sin\beta\sin(\pi/2 - \gamma)$$

$$R_3(2,2) = \cos^2\beta\sin^2\alpha + \cos(\pi/2 - \gamma)(1 - \cos^2\beta\sin^2\alpha)$$

$$R_3(2,3) = -\sin\alpha\sin\beta\cos\beta + \cos(\pi/2 - \gamma)\sin\alpha\sin\beta\cos\beta - \cos\alpha\cos\beta\sin(\pi/2 - \gamma)$$

$$R_3(3,1) = -\cos\alpha\sin\beta\cos\beta + \cos\alpha\cos(\pi/2 - \gamma)\sin\beta\cos\beta - \cos\beta\sin\alpha\sin(\pi/2 - \gamma)$$

$$R_3(3,2) = -\sin\alpha\sin\beta\cos\beta + \cos(\pi/2 - \gamma)\sin\alpha\sin\beta\cos\beta + \cos\alpha\cos\beta\sin(\pi/2 - \gamma)$$

$$R_3(3,3) = \cos^2\beta\cos(\pi/2 - \gamma) + \sin^2\beta \qquad \text{(A.7)}$$

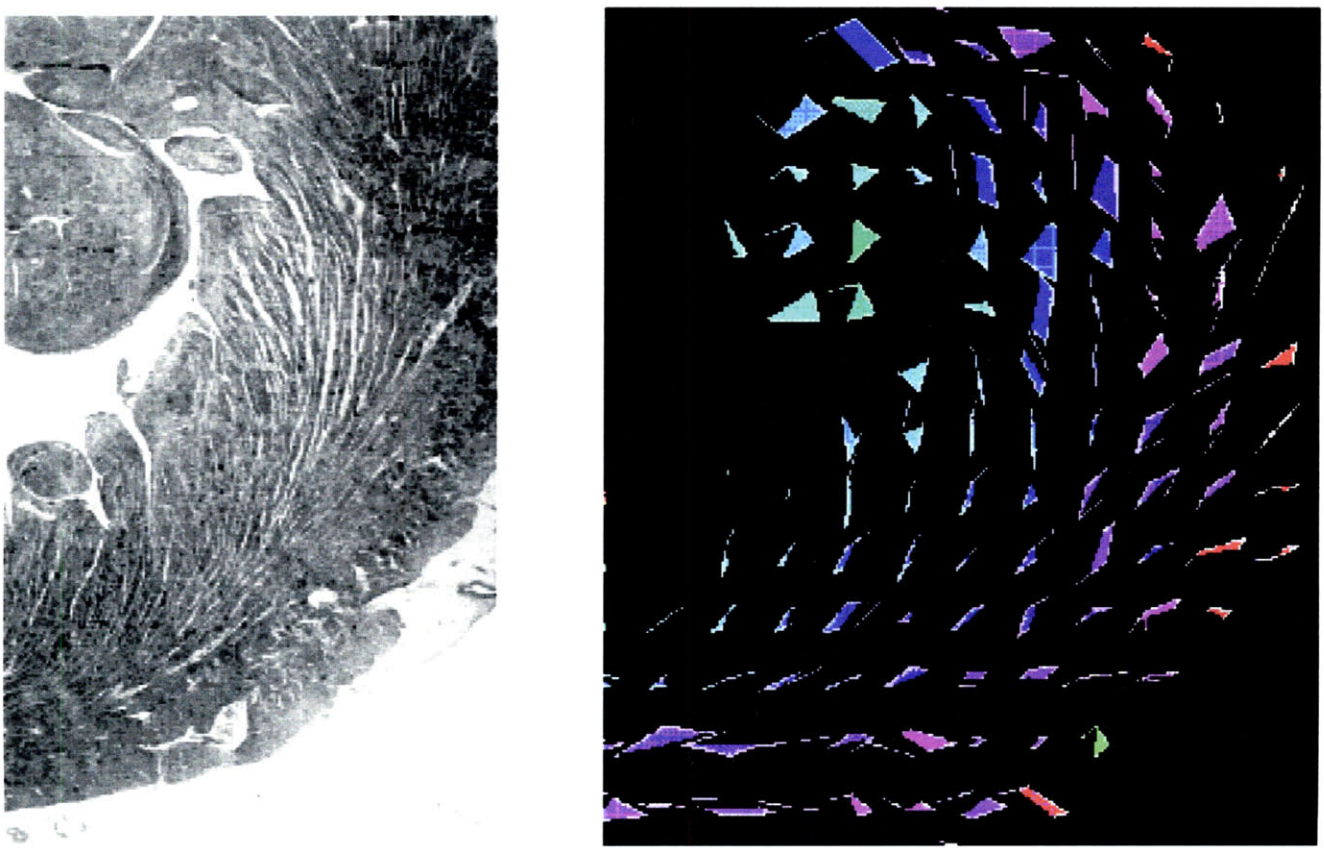

Figure 2.1 A histologic section showing cleavage planes (left; from Lunkenheimer [71]), and a short axis MRI of 1-2 eigenspace of the diffusion tensor (right).

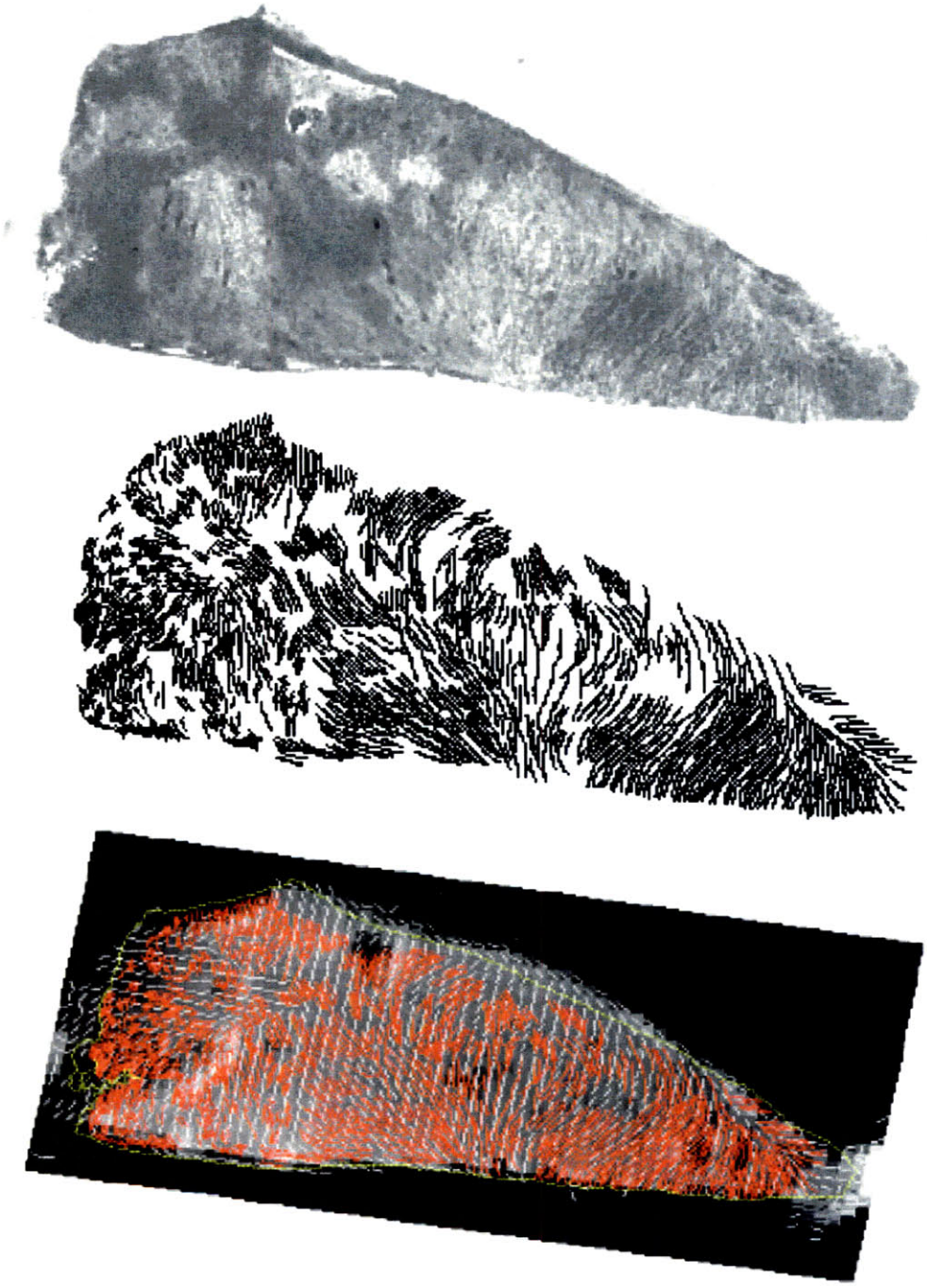

Figure 2.2 The top panel shows a digitized image of cleavage planes inked from a cut face of a longitudinal slab. The middle panel shows traced lines of the above digitized image. The bottom panel shows traced lines (red segments) and boundary (yellow contour) superimposed over the computed intersections (white segments) of the diffusion tensor MRI of the same specimen.

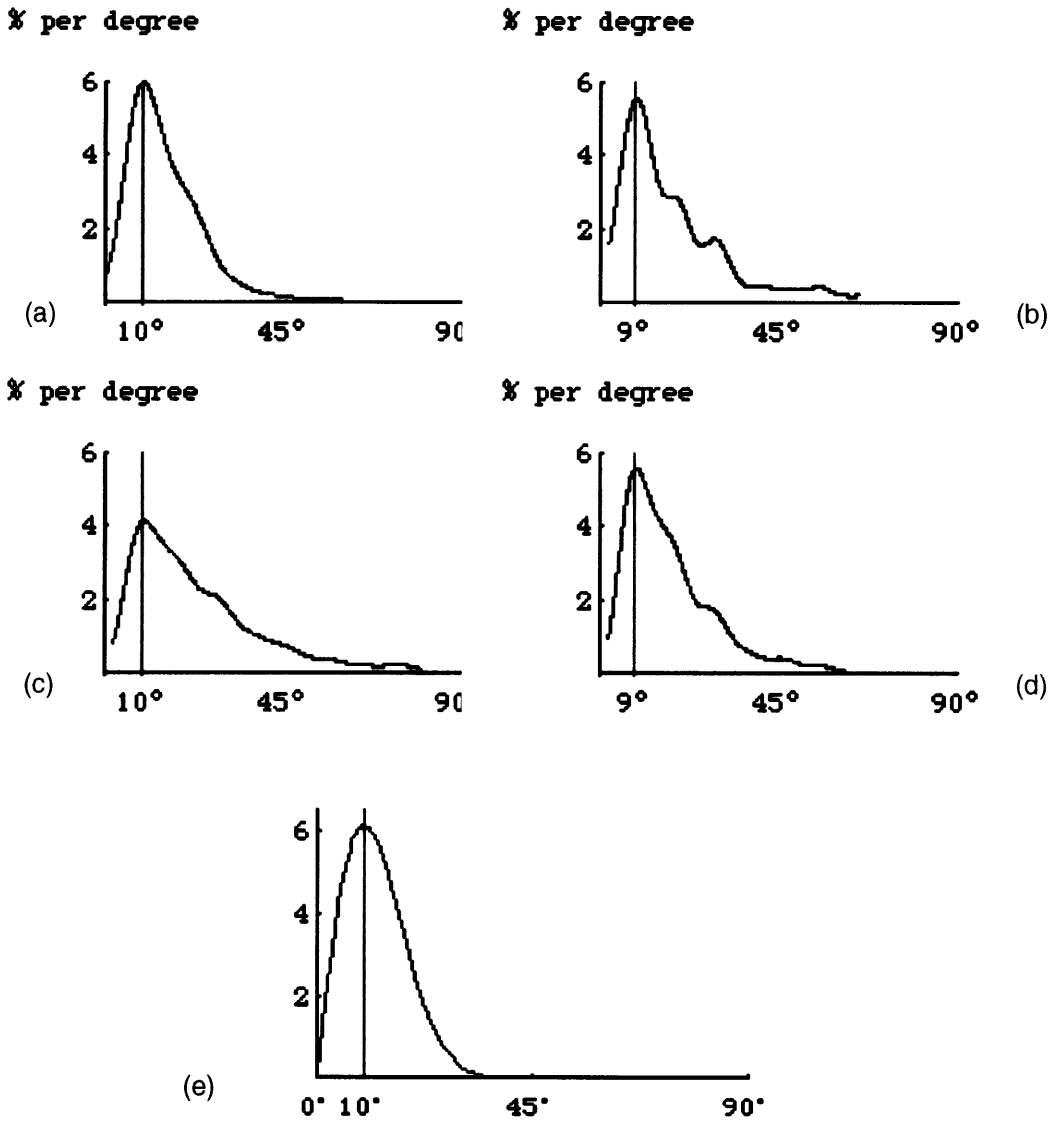

Figure 2.3 Histograms of specimens 1 (top left, a), 2 (top right, b), 3 (middle left, c) and 3' (middle right, d). The bottom figure (e) shows a histogram of disparity angles that is a multiplication of a Gaussian function and sin(θ). The location of the peak disparity is related to the width of the Gaussian σ by $\sigma = \theta_p \tan(\theta_p)$.

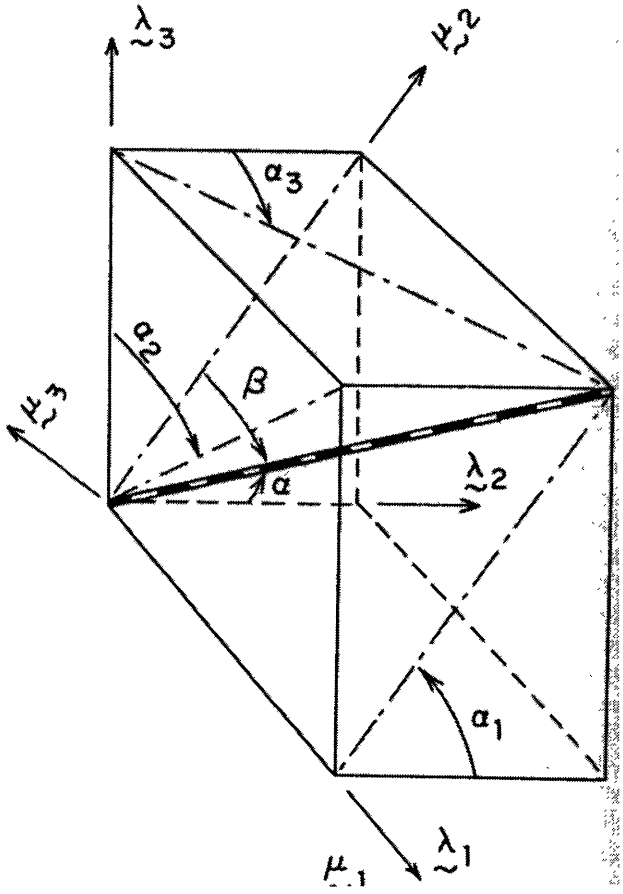

Figure 2.4 3D orientation of the fiber and the geometric illustration of the helix and imbrication angles. For a fiber element (the rod with stripes) at an arbitrary point in the wall, its components in orthogonal planes of local cardiac coordinates (circumferential λ_1, longitudinal λ_2, radial λ_3) are the helix angle α_1, the longitudinal angle α_2, and the traverse angle α_3, respectively. Fiber imbrication angle β is defined relative to μ_2 axis on imbrication plane, namely the plane spanned by the fiber and μ_2 axis.

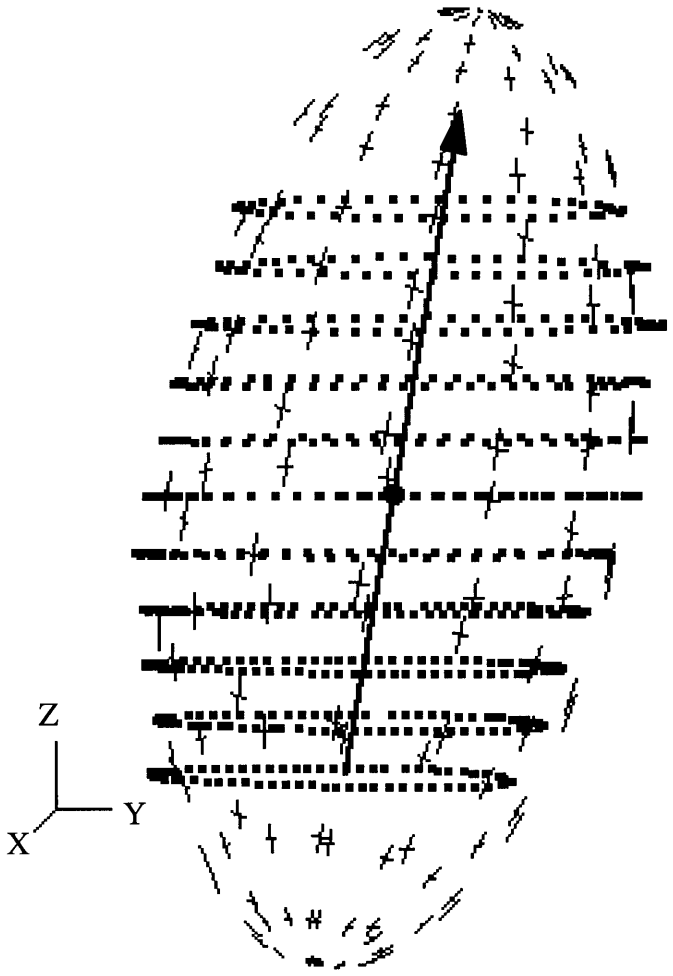

Figure 2.5 An ellipsoid (marked by little crosses on its surface) that best fits the epicardial contours (little black dots) from base to apex. The straight line indicates the ventricular axis with the arrow head point toward base. The axis passes through the center of the ellipsoid at the mid-ventricular level (big dot). The positions are described in the image-coordinates {X, Y, Z}.

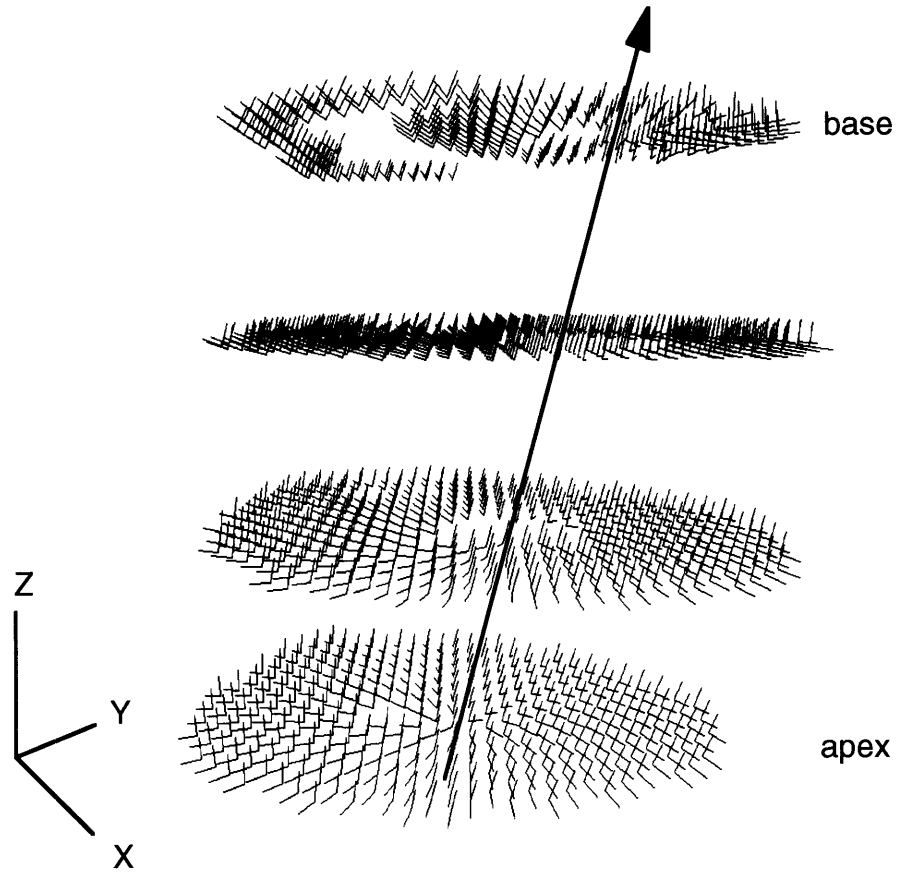

Figure 2.6 Longitudinal and radial vectors at each pixel in the image-coordinates {X, Y, Z}. Four equally spaced short-axis slices of the heart from base to apex and the left ventricular axis indicated by a thick line pointing toward base are shown. Longitudinal vectors are the short segments with their unconnected ends pointing toward base, and radial vectors are those pointing outward.

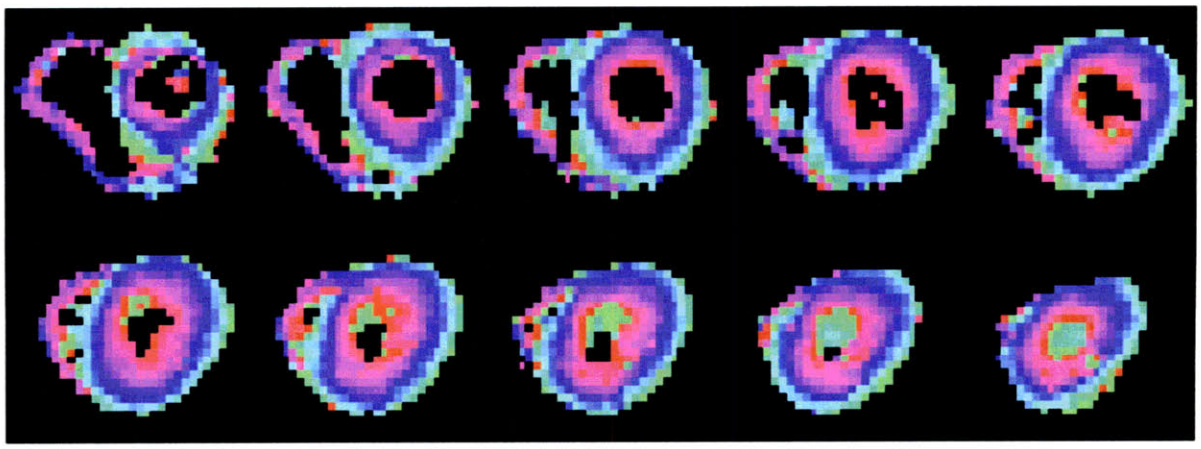

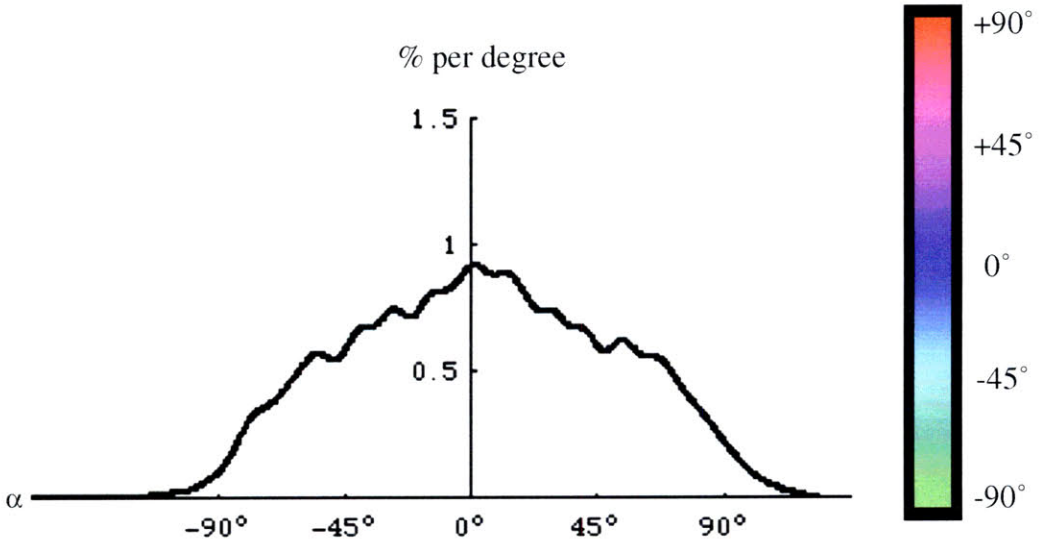

Figure 2.7 Helix angle (α) maps in 10 slices from base to apex (top). The helix angles are color-coded as indicated by the color bar on the bottom right. Helix angle histogram of the same fiber population is shown on the bottom left.

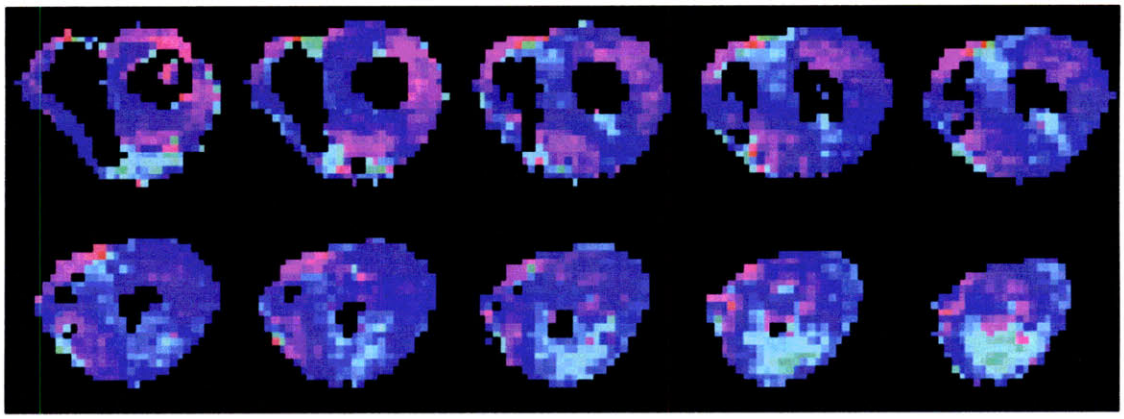

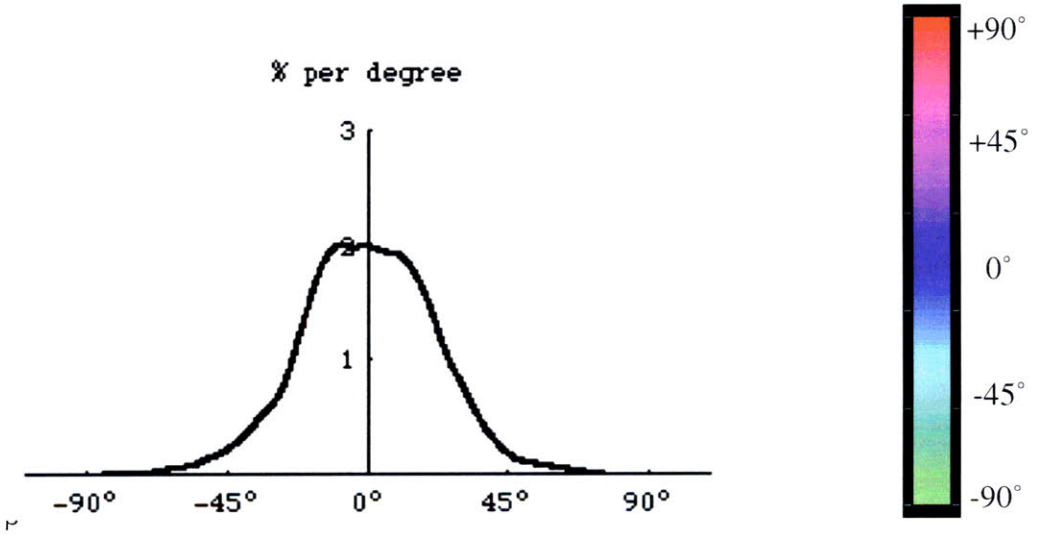

Figure 2.8 Imbrication angle (β) maps in 10 slices from base to apex (top). The imbrication angle in each pixel is color-coded as indicated by the color bar on the bottom right. Imbrication angle histogram of the same fiber population is shown on the bottom left.

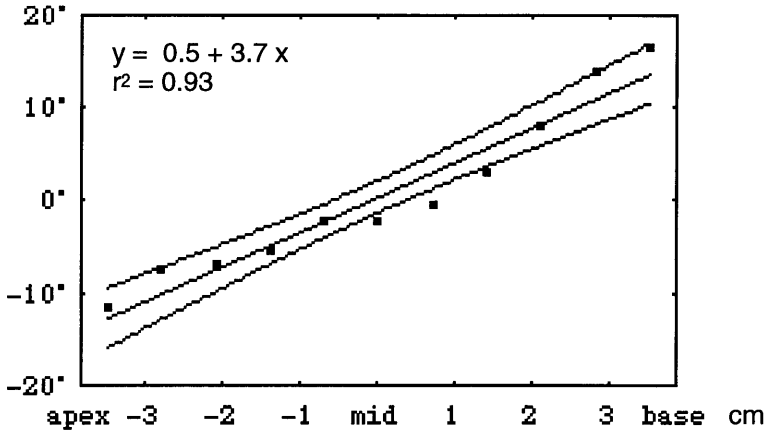

Figure 2.9 Linear regression of the mean imbrication angles versus distance along apex to base direction. The distance (cm in unit) zero is set at the mid-ventricle level. The transition of imbrication angles shows a smooth linear increase from apex (≈-13°) through mid-ventricle (≈0°) to base (≈13°).

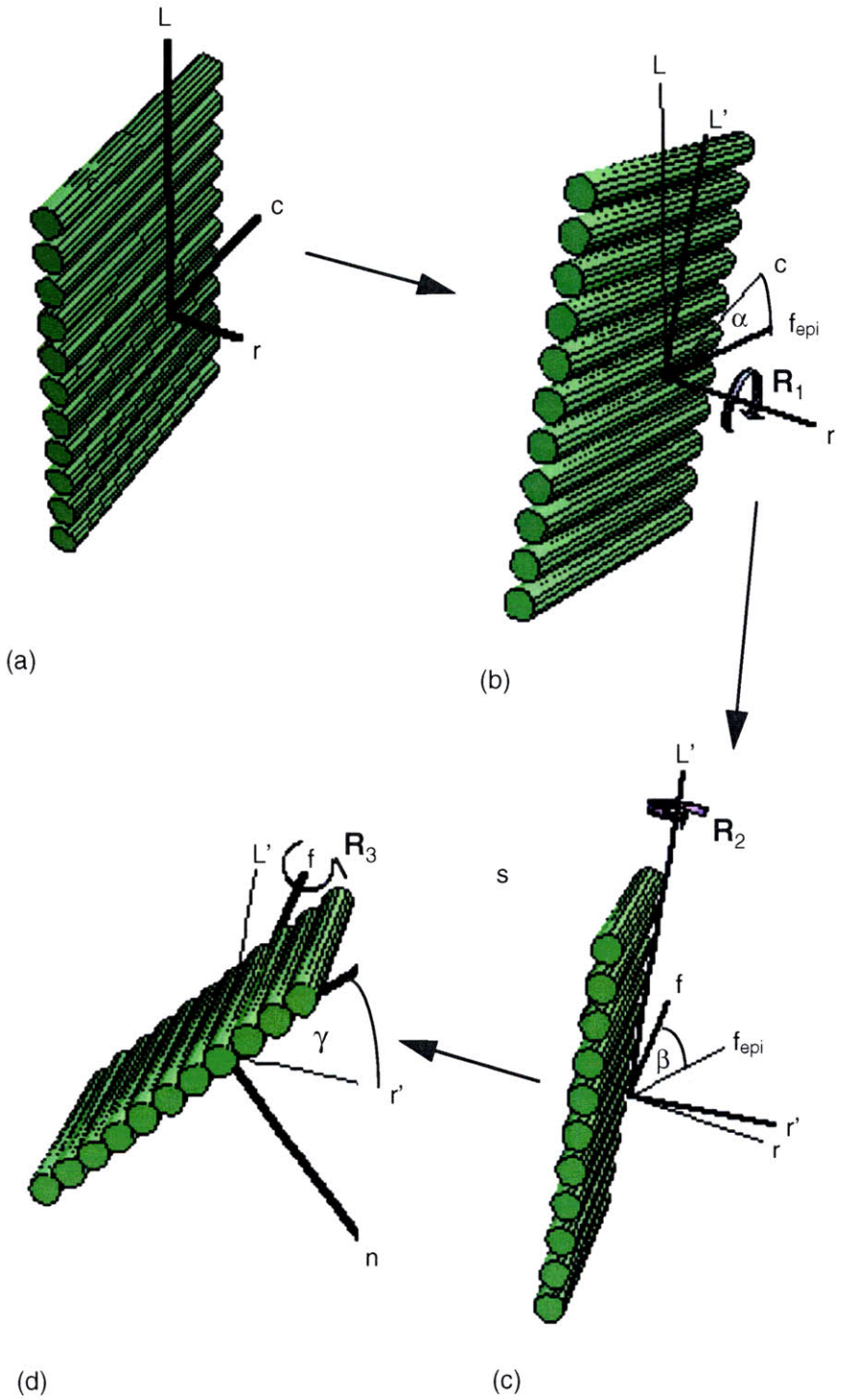

Figure 2.10 Three successive rotations from local cardiac coordinates (**c**, **L**, **r**) to material coordinates (**f**, **s**, **n**). The first rotation ($\mathbf{R}_1$) is about radial axis (**r**) by α, shown from (a) to (b); the second rotation ($\mathbf{R}_2$) is about **L**' by β, shown from (b) to (c); and the third rotation ($\mathbf{R}_3$) is about fiber axis (**f**) by γ, shown from (c) to (d).

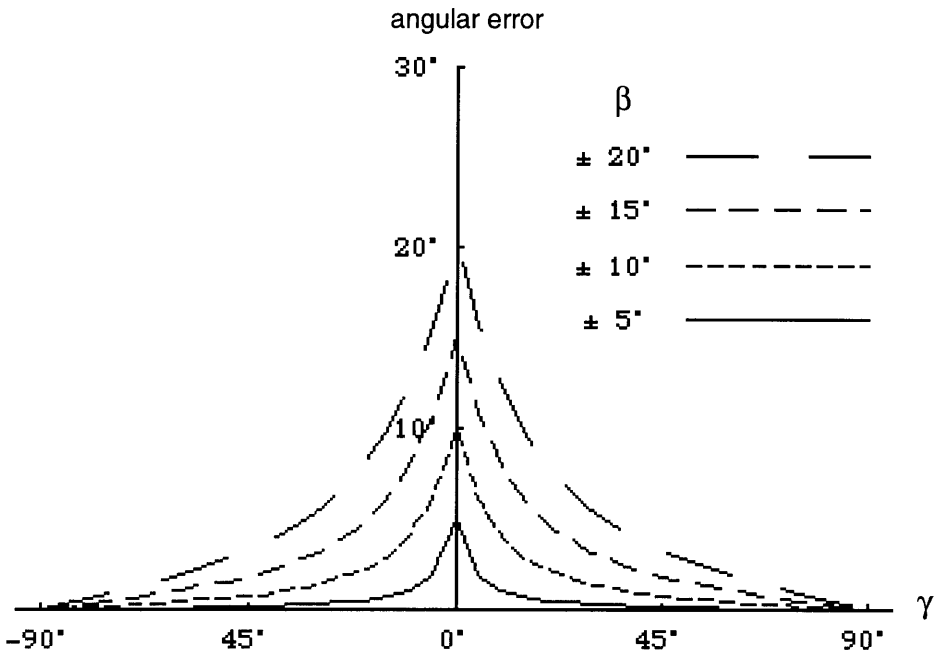

Figure 2.11 A plot of angular error using Eq. 2.6 to calculate sheet angle (γ'). Four curves of errors corresponding to different imbrication angles β (±20°, ±15°, ±10°, ±5°) show that the maximum error occurs at 0° of sheet angle (γ) while the minimum occurs at ±90°. Such error does not occur if the sheet angle is calculated by Eq. 2.7 (γ').

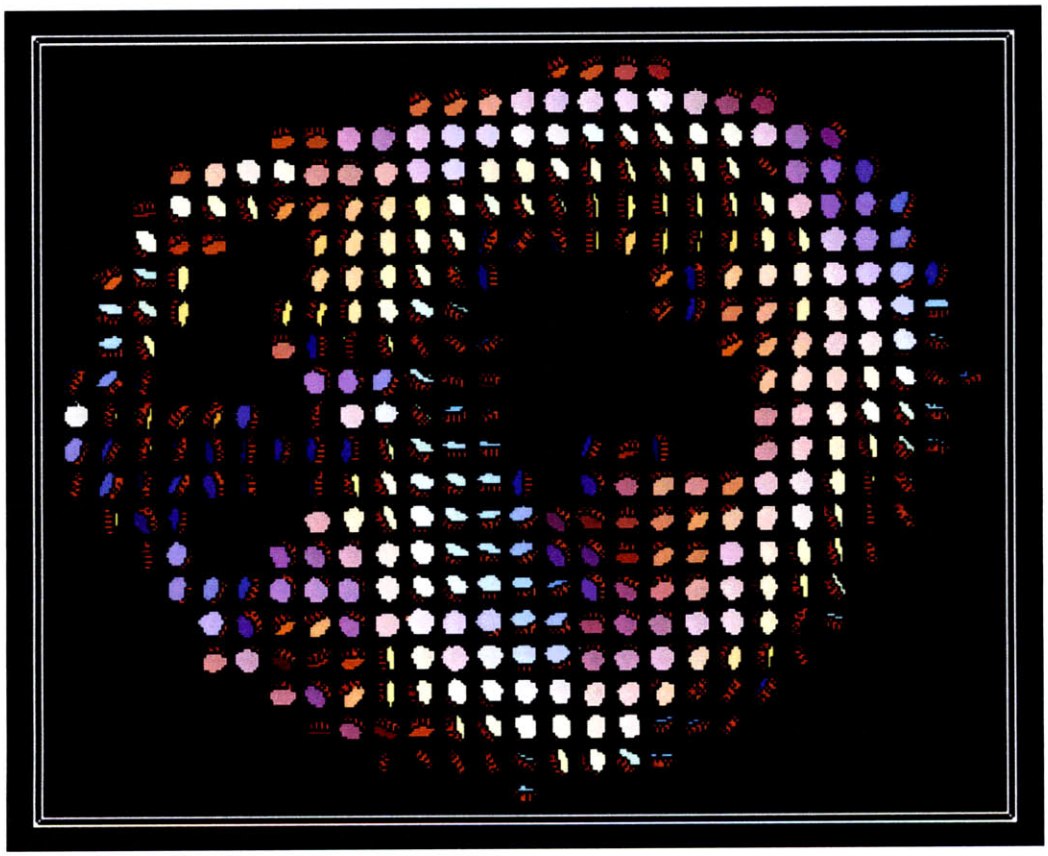

Figure 2.12 Sheet architecture at mid-ventricle level rendered by a three-dimensionally oriented disc at each pixel. It is obvious to see that top faces of the discs at the septum are mostly oriented toward left ventricular cavity, but those at the free wall are mostly oriented opposite to the cavity. This orientation pattern accounts for the sheet polarization pattern observed in the gray-level sheet angle maps (see Fig. 2.13).

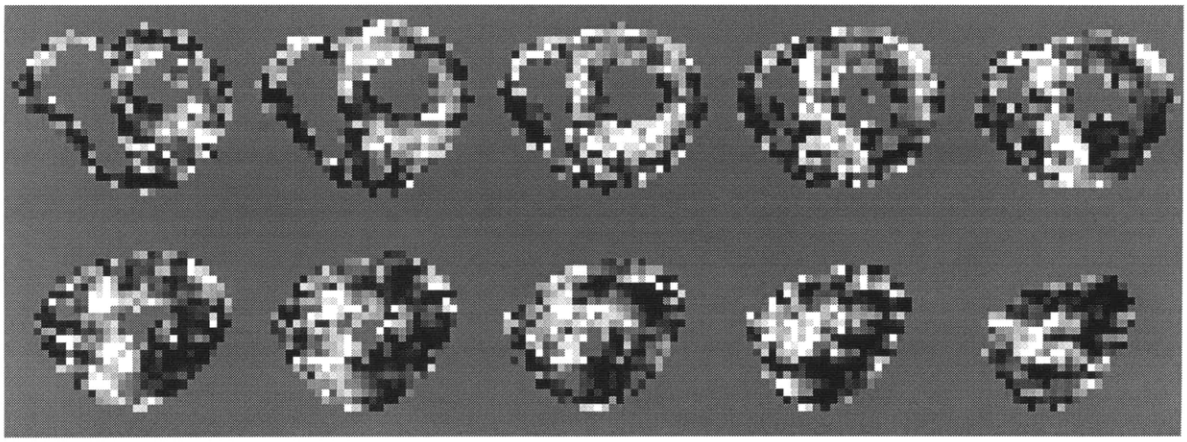

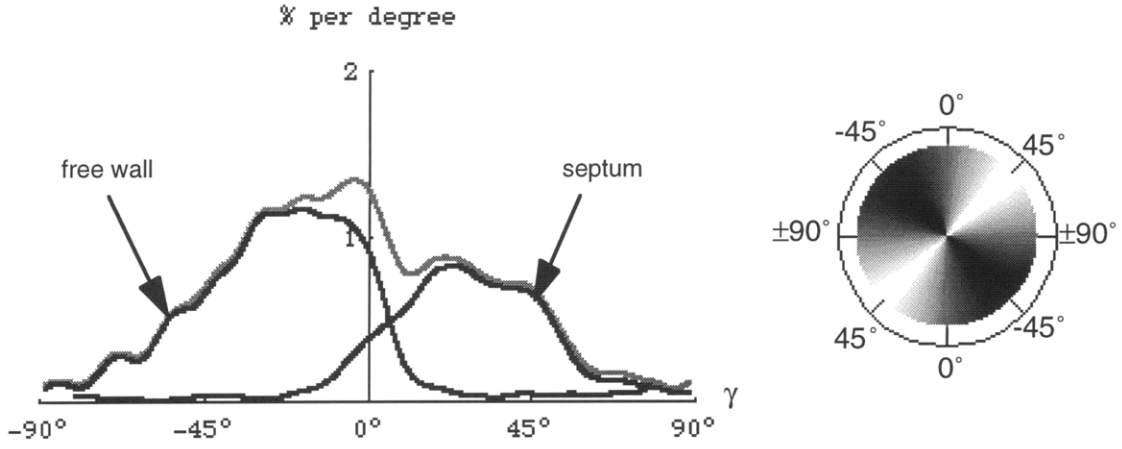

Figure 2.13 Sheet angle (γ) maps and histogram of the normal heart. Sheet angles at each pixel of the spatial maps (top) are scaled by gray levels according to the pie chart indicated at the bottom right. Sheet angle histogram (bottom left) shows individual distributions in the septum and the free wall (black curves) as well as total distribution (gray curve). Bimodal distribution of septum versus free wall is evident.

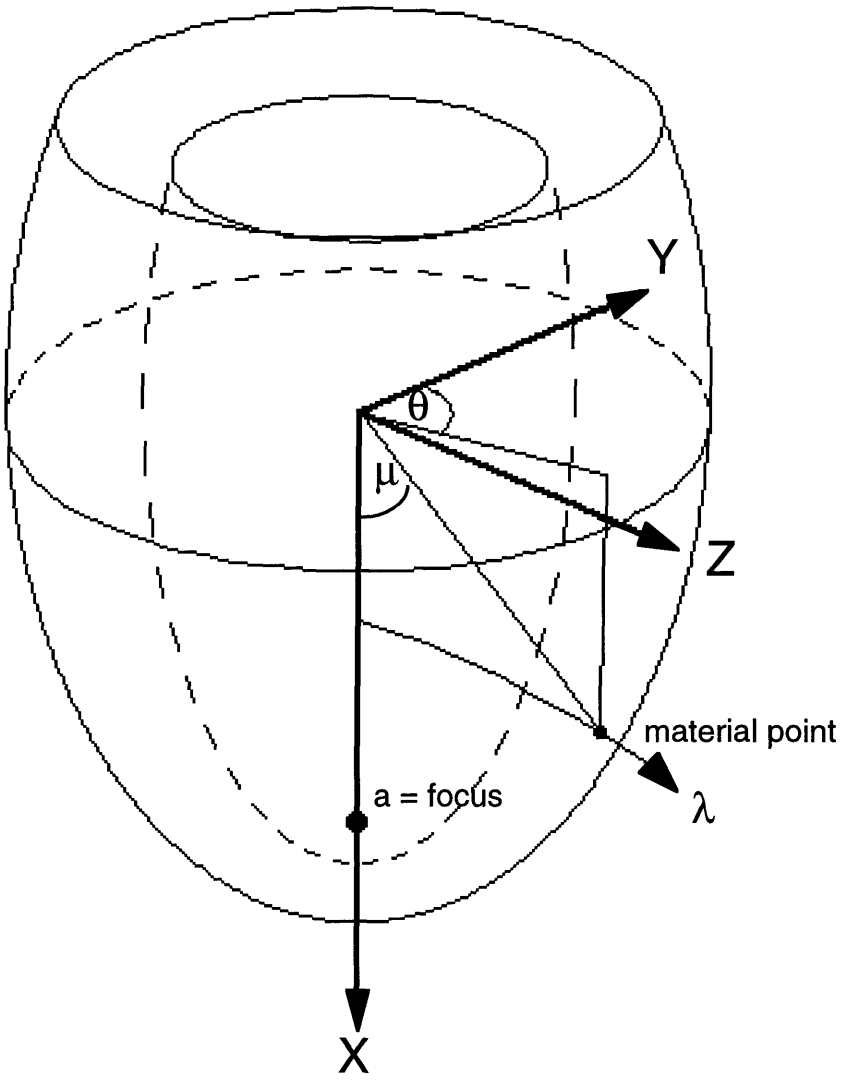

Figure 2.14 Cardiac prolate spheroid coordinates (λ, μ, θ) in relation to rectangular Cartesian coordinates (x, y, z). The geometry of the heart is modeled as confocal shells of ellipsoid of revolution about x-axis with constant λ. Any material point at (x, y, z) has a unique corresponding prolate spheroid coordinates (λ, μ, θ).

Chapter 3

Diffusion Tensor MRI of Architectural Derangement in the Diseased Myocardium

3.1 Introduction

In many heart diseases, abnormal changes in underlying myocardial architecture are often observed, and are thought to be the cause of subsequent alteration of the cardiac morphology and deterioration of the cardiac function [33, 83-85]. With MR diffusion tensor imaging, we have been able to depict the myocardial architecture of the normal heart, and have characterized it in terms of three angles: helix angle, imbrication angle and sheet angle. Spatial maps of these three angles are found to have distinctively different geometric patterns: axisymmetric transmural variation of the helix angles, septum-versus-free-wall polarization of the sheet angles and apex-to-base transition of the imbrication angles. Overall distribution patterns of the three angle populations are provided by histograms, from which quantitative information pertinent to the distribution features can be derived. Knowing normal patterns of the myocardial architecture, we want to investigate, with the same MRI method, the change in these angle distributions in the diseased hearts.

To contrast the change from the angle distributions of the normal heart, we choose two abnormal hearts with vividly different morphological and architectural changes: hypertrophic cardiomyopathy (HCM) and acute myocardial infarction with infarct expansion (IE). Hypertrophic cardiomyopathy is an autosomal dominant disorder manifesting as thickening of the left and/or right ventricular wall in the absence of increased cardiac work. A bizarre and unique disorganization of the fiber orientation (fiber disarray) was uniformly found in the autopsies of the HCM myocardium [86]. Post-infarct expansion is a disproportionate thinning of acutely infarcted myocardium that occurs within the first 24 hours after infarction. The thinning of the wall also involves non-infarcted regions and leads to early cardiac dilatation [87, 88]. The mechanism of wall thinning in non-infarcted regions is thought to be due to the slippage of the fiber bundles (cellular rearrangement) [32, 33]. The inherently different architectural changes of hypertrophic cardiomyopathy and infarct expansion provide us an opportunity to see whether MR diffusion tensor imaging is capable of differentiating between these two abnormalities or not.

The goal of this study is to: 1) demonstrate that angle distribution patterns obtained from the MRI method can detect architectural change in hypertrophic cardiomyopathy and infarct expansion; 2) quantify the characteristic changes in angle distributions in these two kinds of diseased hearts.

3.2 Methods

Two fresh cadaver hearts were obtained from autopsies on two patients, one diagnosed as having hypertrophic cardiomyopathy and another as acute myocardial infarction with infarct expansion. Multiple transaxial MR diffusion tensor images from base to apex were acquired in each heart. Local cardiac coordinates were established using prolate spheroid fit of the epicardial contours. Helix angle (α), imbrication angle (β) and sheet angle (γ) were quantified with the same procedures used in the normal heart. Spatial maps and histograms of these three angles were produced and compared with those of the normal heart.

The features of the alteration in spatial maps of three orientation angles were assessed first. The changes were then quantified from the histograms. The quantities included for comparison were variances of the histograms of α, β, and γ angles, relative populations of the smaller absolute angles and the diffusion anisotropy. The way of obtaining these quantities is explained as follows. To reveal the significance of the difference in variances, variance ratio and variance ratio (95%) confidence interval were computed for each angle. Since there was a systematic shift of the mean imbrication angles of each slice along the apex-to-base direction, we adjusted this variation by subtracting the mean from the angles of the same slice. Smallness of the angles was set in accord with the typical range of angular variation; they were $\pm 30^\circ$, $\pm 20^\circ$ and $\pm 10^\circ$ for helix angle, sheet

angle and imbrication angle, respectively. The ratios of the population of the smaller absolute angles relative to the total population were then calculated for comparison. Diffusion anisotropy was calculated by taking the ratio of variances of the mean-normalized diffusion eigenvalues between the normal heart and each of the abnormal hearts. Variance ratio (95%) confidence intervals were also calculated to reveal the significance of difference.

3.3 Results

3.3.1 Hypertrophic cardiomyopathy

From MRI, the morphologic feature of the HCM heart can be identified by having a disproportionate hypertrophy of the interventricular septum with the mean septum-to-free-wall ratio of 1.3 or greater [89].

Spatial maps of angles α, β, and γ (in Figures 3.1, top, 3.4 and 3.2, top, respectively) in general maintain the same geometric patterns as those in the normal heart. However, there is a mosaic pattern observed in these angle maps; namely, the variation of the angles between adjacent pixels is not smooth. This pattern can be easily appreciated in the helix angle maps (Fig. 3.1). A smooth, transmural transition of helix angles typically found in normal hearts is changed to irregular transition zones in HCM. This irregular pattern is more prominent in the interventricular septum than in the free wall. Furthermore, the zone of circumferential fibers (in bluish hue) in the septum appears relatively wider than in the free wall.

As compared with the normal heart, the helix angle histogram appears more triangular, and has a significant peak at 0° (Fig. 3.3, top). The sheet angle histogram shows less septum-versus-free-wall distinction (about 20° peak-to-peak gap versus 45° in the normal) and a broader variance for each bump (Fig. 3.4). The imbrication angle histogram has a significantly wider distribution with a lower peak (Fig. 3.3, bottom).

3.3.2 Infarct expansion

A dilated heart with a huge pseudoaneurysm formation (in contrast to an aneurysm, the wall of pseudoaneurysm is enclosed by pericardium only) mostly involving the anterior free wall and interventricular septum is the hallmark of the infarcted heart. In this heart, rupture at the septum and blood clots in the dilated cavity are evidenced in MRI. The infarcted region is large, extending longitudinally in the anterior wall, and is mostly destroyed due to pseudoaneurysm formation and rupture. Because of our interest in the intact myocardium, the pseudoaneurysm and the ruptured septum were excluded from the analysis.

Helix angle maps (Fig. 3.1, bottom) still maintain a transmural variation, but the zone of circumferential fibers seems to be depleted. Sheet angle maps (Fig. 3.5) show little traceable polarization pattern, and imbrication angle maps (Fib. 3.2, bottom) show loss of typical apex-to-base transition.

In contrast to the HCM heart, the histograms of the infarct expansion heart in general show the opposite change. The histogram of the helix angle (Fig. 3.3, top) looks like a truncated pyramid because of depletion of the circumferential fiber population. The flat top ranges from about -60° to 60°. The sheet angle histogram has a somewhat uniform distribution without any bimodal or unimodal feature (Fig. 3.5). The imbrication angle histogram shows a skew pattern with dominant negative angle population and a peak at about 7° (Fig. 3.3, bottom).

3.3.3 Quantitative comparison

Despite the change in the distribution shapes, variances of α, β, and γ angle distributions of the diseased hearts are uniformly wider than those of the normal heart (Table 3.1, columns 1 to 3). Among them, the most significant changes are the increase in variance of the imbrication angles of the HCM heart and the increase in variance of the sheet angles of the infarcted heart. Relative populations of the smaller absolute angles show, consistent with the histograms, an opposite trend of change in two abnormal hearts. For hypertrophic cardiomyopathy, the change increases in helix angle and decreases in imbrication angle, whereas for infarct expansion, it decreases in helix angle and increases in imbrication angle (Table 3.1, columns 4 to 6). The sheet angles of the infarct expansion show a drastic reduction in the population of small angles. Diffusion anisotropy shows no significant difference between the normal and the infarcted heart, but a significant reduction in the HCM heart (Table 3.1, column 7).

	$\sigma^2(\alpha)$ ratio ± 95% C.I.	$\sigma^2(\beta)$ ratio ± 95% C.I.	$\sigma^2(\gamma)$ ratio ± 95% C.I.	relative population $\lvert\alpha\rvert \leq 30°$	relative population $\lvert\beta\rvert \leq 20°$	relative population $\lvert\gamma\rvert \leq 10°$	$\sigma^2(D)$ ratio ± 95% C.I.
HCM	1.1±0.1	1.9±0.1	1.2±0.1	0.51	0.28	0.42	4.5±0.2
IE	1.2±0.1	1.4±0.1	1.7±0.2	0.36	0.39	0.26	1.0±0.1
Normal	1	1	1	0.44	0.41	0.35	1

Table 3.1 Comparison of fiber and sheet angle distributions between normal and diseased hearts. Note $\sigma^2(\alpha)$ ratio, $\sigma^2(\beta)$ ratio , $\sigma^2(\gamma)$ ratio indicate variance ratios of abnormal to normal heart for helix angle α, imbrication angle β and sheet angle γ, respectively. C.I. is the confidence interval. The $\sigma^2(D)$ ratio indicates the diffusion eigenvalue variance ratio of normal to abnormal hearts.

3.4 Discussion

This chapter demonstrates the capability of MR diffusion tensor imaging to reveal architectural derangement in the myocardium of hypertrophic cardiomyopathy and infarct expansion. By assessing the spatial maps and analyzing the histograms of fiber and sheet orientations, we have specified characteristic changes for each of these two different diseases. In the following paragraphs, we will discuss these MR findings and relate them to typical architectural changes observed in pathology.

The most striking microscopic finding in hypertrophic cardiomyopathy is the presence of disorganized cardiac muscle cell clusters (fiber disarray) scattered in the myocardium [90]. No longer maintaining parallel relation to each other, in these foci adjacent cardiac muscle cells are aligned perpendicularly or obliquely to each other. Corresponding to this unique microscopic feature, three obvious changes are observed in MR diffusion tensor images: 1) mosaic appearance in the spatial maps of helix, sheet and imbrication angles; 2) increased variances in the histograms of these three angles; and 3) decreased diffusion anisotropy. The mosaic appearance of the angle maps indicates that the transition of structural orientation between nearby pixels is not smooth. This appearance is probably due to the fact that mean orientations of the fiber-sheet structure in different voxels are perturbed by different extents of fiber disarray. Though the mosaic pattern prevails over the whole ventricle, it is more prominent at the asymmetrically thickened interventricular septum (See Figures 3.1 and 3.2). This is consistent with the pathologic finding that area of architectural disorganization in the septum is often greater than that in the free wall [90, 91]. Increases in variances of three angle histograms, we believe, are also the results of fiber disarray. Among three angles, the variance of imbrication angles appears to be the quantity that most sensitively reveals the difference from the normal. Variance (±95% C.I.) in HCM is 778 ± 34 versus 455 ± 24 in normal with variance ratio (±95% C.I.) of 1.9 ± 0.1. In the histograms of helix angle and sheet angle there are, respectively, increased circumferential fiber population and decreased bimodal distribution that compete with the broadening effect of the fiber disarray and make the change in variance of these two angles less sensitive. The myocardium of HCM heart shows significant decrease in diffusion anisotropy; variance ratio (±95% C.I.) of principal diffusivities for normal to HCM is 4.5 ± 0.2. This can be understood by viewing the diffusion tensor $\mathbf{D}$ as a dyadic average of the population of fiber orientation vectors within the voxel $\{\mathbf{f}_n\}$, i.e., $\mathbf{D} = d \sum_n \mathbf{f}_n \otimes \mathbf{f}_n$, where d is a scalar constant. In the presence of fiber disarray, disordered fiber orientations within each voxel smear out the preferential orientation of the diffusion tensor, and so decrease the diffusion anisotropy.

The major architectural change in the non-infarcted myocardium of the infarcted heart is the structural remodeling secondary to hemodynamic change and slippage of the myocyte layers [32]. Recent understanding of the mechanical function of the sheet structure provides some insights into this slippage motion. During systole, sheets normally slide on each other and rotate by about 15° so that the sheet orientation moves closer to the radial direction. This slippage motion between the sheets results in increased transmural myocyte numbers and hence the thickening of the wall [30, 31]. By the same mechanism but in the opposite direction, wall thinning is the consequence of a sheet slippage with the sheets approaching an orientation perpendicular to the radial direction. This induces a decrease in transmural myocyte numbers and therefore the wall thinning. In infarcted hearts, this sheet slippage may be aggravated by elevated intra-cavitary pressure as well as damaged collagen framework of the myocardium [92, 93]. Microscopically, it has been found that subendocardial cleavage planes form acute angles to the endocardial surface and that there is a significant reduction in transmural myocyte numbers in the infarct expansion heart [33]. These architectural changes are consistently reflected in the marked reduction of the relative population of the small absolute sheet angles in the histogram (0.26 for the infarcted heart versus 0.41 for the normal).

In the infarct expansion heart, the circumferential fiber population is also decreased significantly (0.36 for the infarcted heart versus 0.44 for the normal). This relative depletion of circumferential fibers in a spherical ventricle is in fact the opposite of what one would expect were fiber redistribution directly caused by the mural deformation. The logic is as follows: sphericalization due to cardiac dilatation implies that the wall has undergone more stretching in the circumferential direction than the axial. Were the fibers carried along passively by this process, then on simple geometric grounds, the final state would have an increase in the volume of fibers with circumferential orientations. In fact, the result of depleted circumferential fibers is the opposite of this. The inconsistency between fiber redistribution with mural deformation may be explained by involution *in situ* of the circumferential relative to the axial fibers. As to a possible cause of this pattern, we postulate that this long apex-to-base infarct may have unloaded circumferential fibers (given them little to work against, as it were, hamstrung them) which then involute. This would represent the inverse of the cases of pressure-overloaded right ventricles, in which specific reversible hypertrophy of the circumferential fibers was constantly found [94].

3.6 Conclusion

MR diffusion tensor imaging is capable of detecting architectural change of the hypertrophic cardiomyopathy and infarct expansion hearts. Corresponding to the characteristic changes observed microscopically, consistent distribution patterns of the fiber and sheet orientations were found and quantified. These results warrant potential application in the clinical investigation from which the relation between architectural derangement and functional deterioration can be understood.

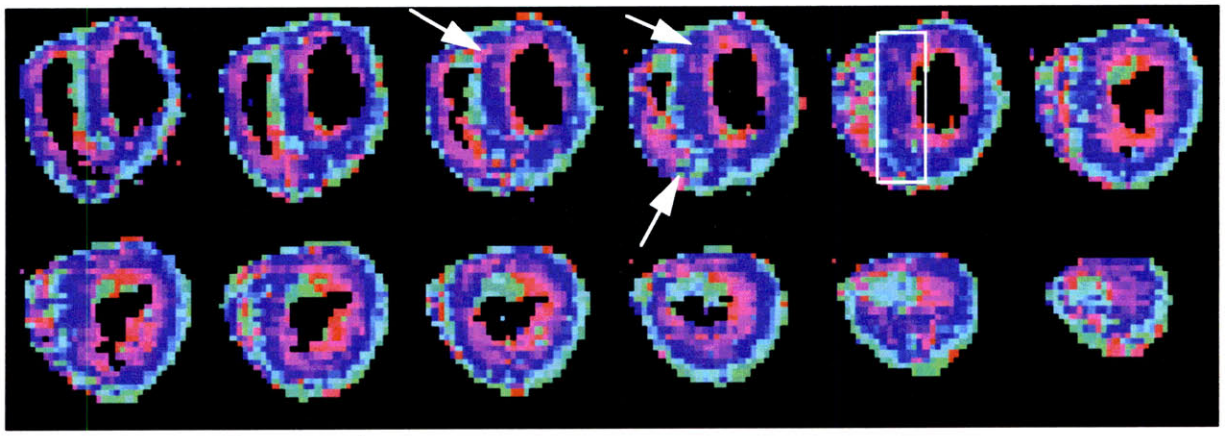

hypertrophic cardiomyopathy

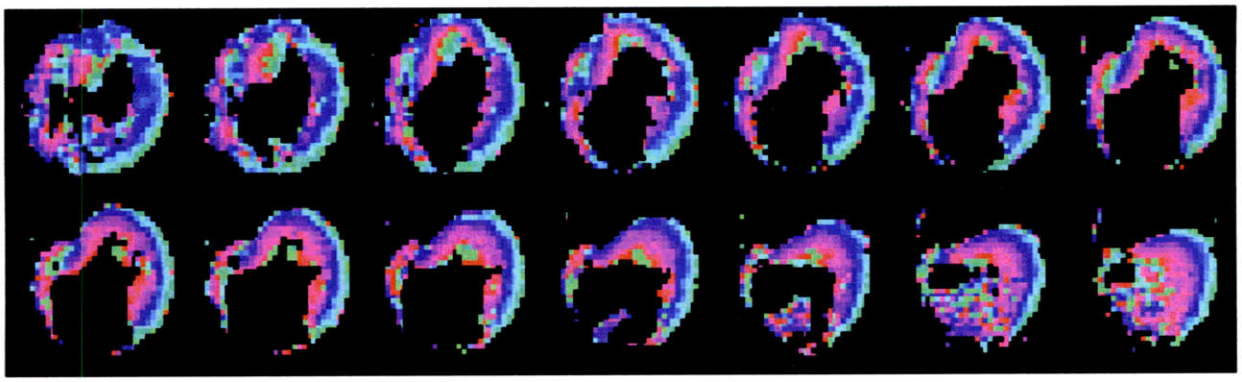

myocaridal infarction with infarct expansion

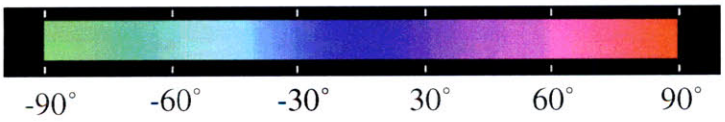

Figure 3.1 Multiple transaxial slices of color-coded helix angle maps of HCM heart (top) and infarct expansion (bottom). Mosaic appearance is most obvious around RV insertions of the HCM (arrows). Also note that in the septum (enclosed by a rectangle at mid-ventricular level), the transmural change of the helix angles is not smooth as compared to the free wall side.

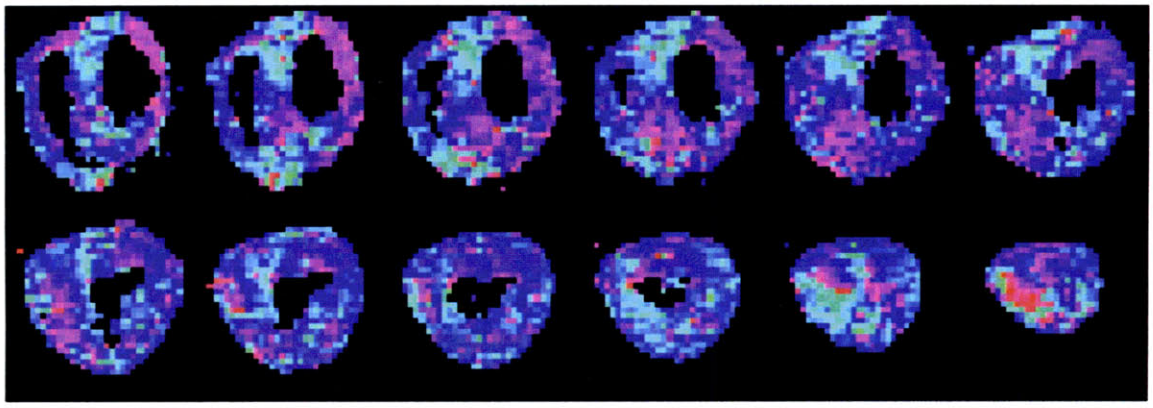

hypertrophic cardiomyopathy

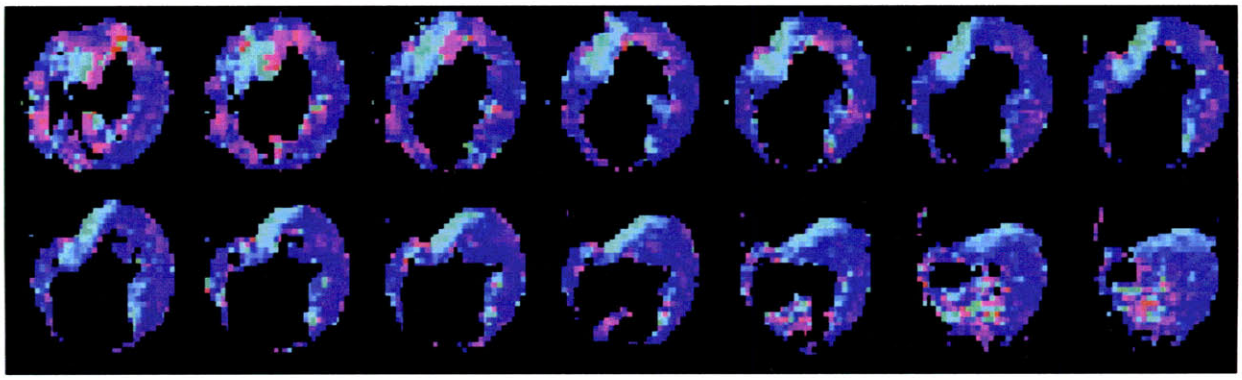

myocaridal infarction with infarct expansion

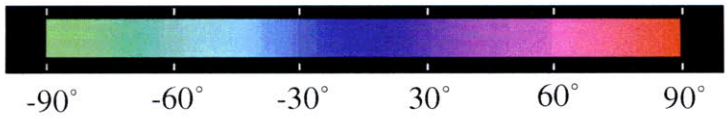

Figure 3.2 Multiple transaxial slices of color-coded imbrication angle maps of the hearts of HCM (top) and infarct expansion (bottom). A mosaic pattern is present in the HCM heart.

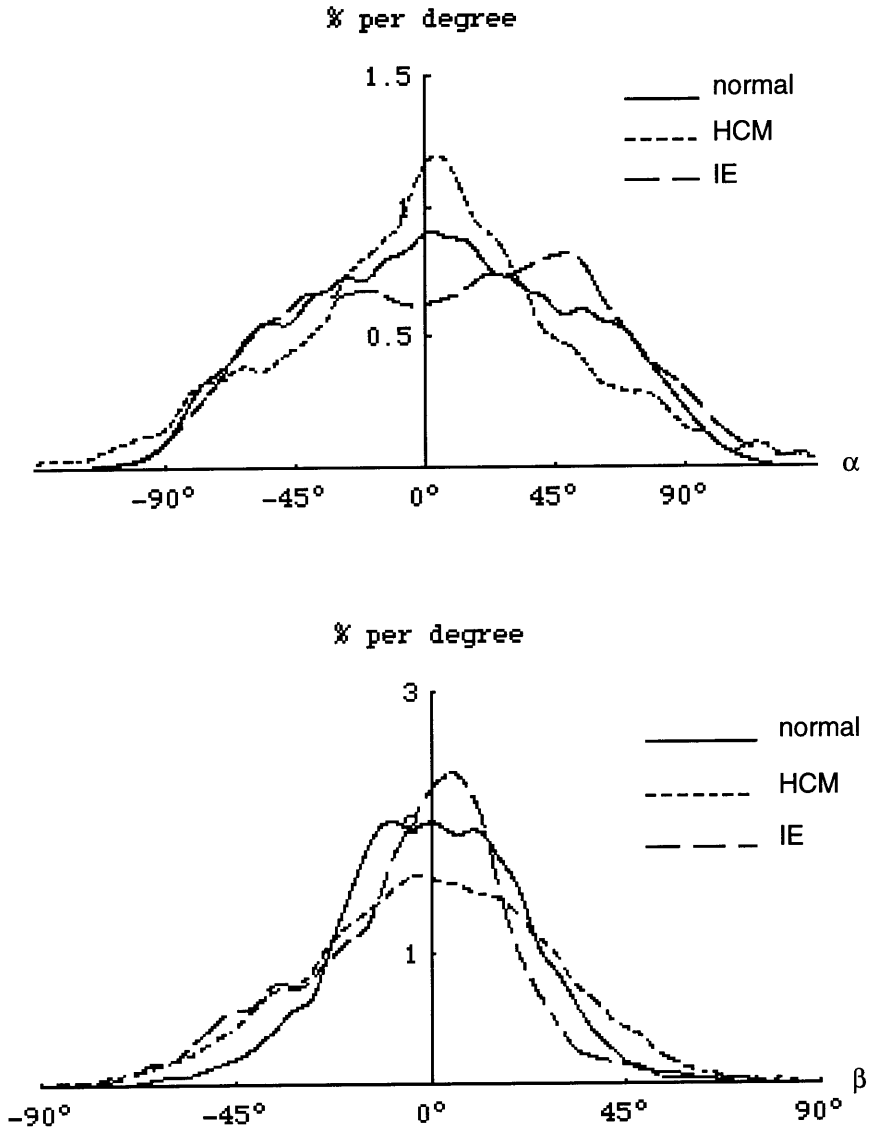

Figure 3.3 Overlapped helix angle (α) histograms, top, and imbrication angle (β) histograms, bottom, of normal, hypertrophic cardiomyopathy (HCM) and infarct expansion (IE).

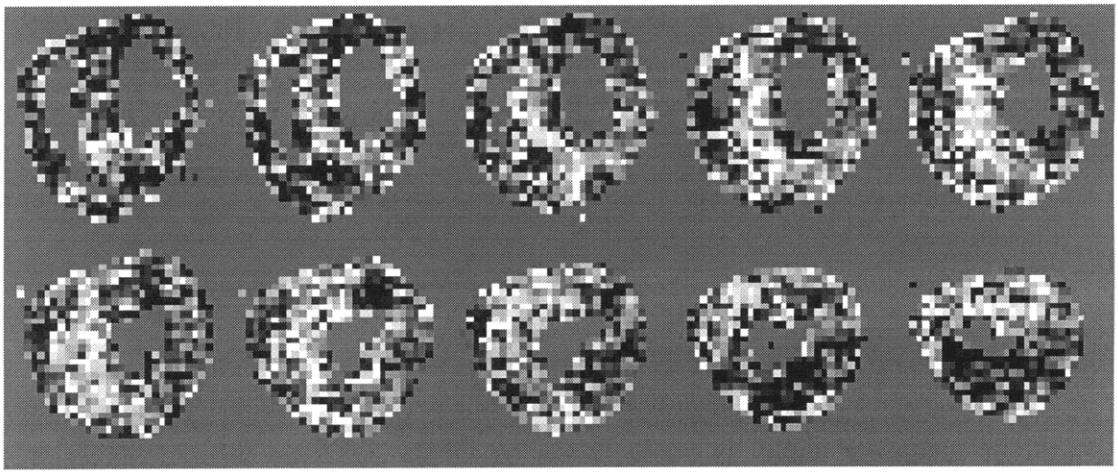

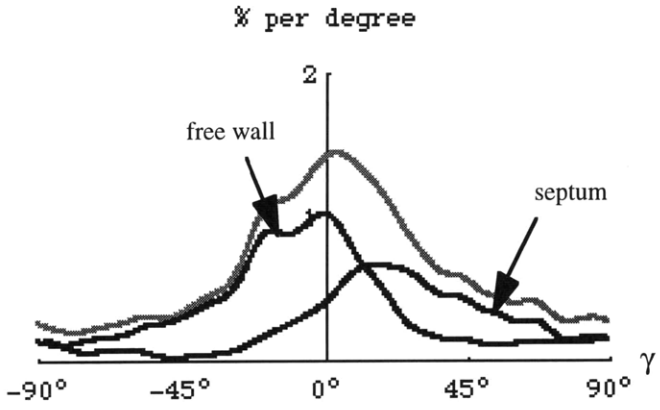

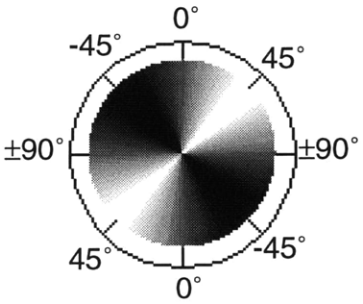

Figure 3.4 Sheet angle maps and histogram of the HCM heart. Sheet angles (γ) at each pixel of the spatial maps (top) are scaled by gray levels according to the pie chart indicated at the bottom right. The sheet angle histogram (bottom left) shows individual distributions in the septum and the free wall (black curves) as well as total distribution (gray curve).

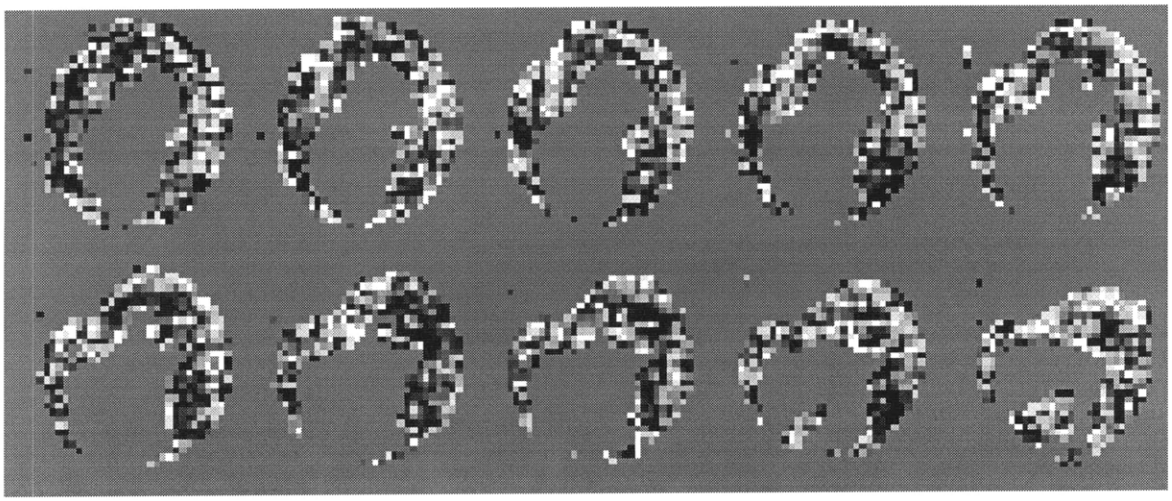

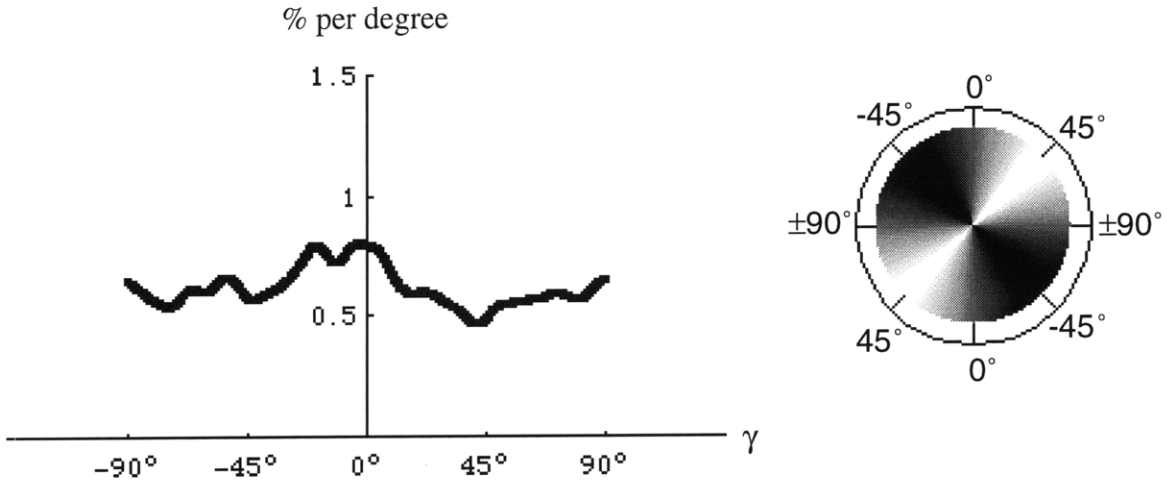

Figure 3.5 Sheet angle maps and histogram of the infarct expansion heart. Sheet angles (γ) at each pixel of the spatial maps (top) are scaled by gray levels according to the pie chart indicated at the bottom right. The sheet angle histogram (bottom left) shows rather uniform population density per degree.

Chapter 4

Cardiac Diffusion Tensor MRI *In Vivo:* A Practical Method without Strain Correction

4.1 Introduction

In previous chapters, we have validated the capability of diffusion tensor MRI to depict the main features of the myocardial architecture *ex vivo*. Now, we want to apply the same technique to the beating heart to obtain the structural information *in vivo*. However, unlike the experiment on the stationary sample, diffusion tensor MRI in the beating heart suffers from unwanted signal loss due to bulk cardiac motion. To control this problem, Edelman et al. developed a technique to encode diffusion over an exact cardiac cycle by means of a stimulated-echo echo-planar MRI (STE-EPI) pulse sequence with two gate triggers [68]. In this way, provided regular cardiac rhythm, little bulk motion is phase-encoded by the diffusion sensitizing gradients, and so signal attenuation of the echo is purely from the molecular diffusion. Reese et al. subsequently found that this experiment contains an important motion-sensitivity via a previously unrecognized mechanism: direct modification of the diffusion-sensitizing spatial modulation of the z-magnetization by the tissue strain. He also showed that these diffusion data can be corrected for strain using an

auxiliary MRI map of the strain histories of each material location in the image [70]. This procedure, however, exacts significant costs in experimental noise, time and complexity.

In the double-gating STE-EPI diffusion experiment, the spatial modulation of the z-magnetization, k(t), is changed cyclically with cardiac motion, and the time average of this change over a mixing time of 1 R-R interval constitutes a net strain effect on the diffusion measurement. In section 1.4, we have emphasized that diffusion attenuation is the result of time integral of $k(t)^2$. Using the diagrams of $k(t)^2$ evolution shown in Fig. 4.1, it is easy to appreciate this strain effect. Consider the strain effect in radial direction, if diffusion-sensitizing gradients are applied at end-diastole (when the wall is the thinnest), the spatial period of k(t) in the radial direction will be stretched throughout the whole diffusion time Δ. Time integral of $k(t)^2$ will thus be smaller than that measured in the stationary heart, and so the observed diffusion is smaller than the true value. If diffusion-sensitizing gradients are applied at end-diastole, an opposite strain effect will occur. Consequently, in this cyclic change there must be at least two points at which the spatial modulation equals its time average. If diffusion sensitizing gradient pulses are applied at these points, "sweet spots," it is possible to obtain a diffusion measurement that is effectively equivalent to a measurement free of strain effect.

This chapter develops a method to find these sweet spots, based on which desired diffusion data can be directly obtained. To do so, we need to define the sweet spots, locate their positions, and to show that MR diffusion measurement at the sweet spots can actually provide reliable information about the myocardial architecture. The body of this work has two parts. The first covers the theory of the sweet spot, why and where they exist, and proposes an efficient method to determine the sweet spot positions. The second offers experimental validation of the theory in human subjects.

4.2 Theory

Within the framework of *in-vivo* cardiac diffusion MRI with a mixing time of one cardiac cycle, a "sweet spot" is a cardiac phase delay of this mixing time at which the effect of strain on the diffusion measurement becomes negligible. This section will show that the existence of such sweet spots depends on two assumptions: 1) that myocardial strains are normally synchronous, so that all strain components at all ventricular locations have parallel time courses; and 2) that the effect of myocardial deformation on the NMR diffusion measurement is linear in strain. Given these assumptions, a sweet spot is a time point where the myocardium achieves its mean strain-state, where the effect of strain on diffusion cancels. We conclude this section with a practical

method to determine the sweet spot from a conventional phase-contrast MRI movie of myocardial strain-rate.

Reese et al. [69] showed that the material strain physically stretches an applied spatial modulation of the z-magnetiziation $\mathbf{k}$. Specifically, a motion $\mathbf{X} \rightarrow \mathbf{x}$ of a material point $\mathbf{X}$ will stretch the spatial modulation $\mathbf{k}(\mathbf{X}) \equiv \mathbf{grad}(\phi)$, ϕ the phase, according to:

$$\mathbf{k}(\mathbf{X}) \rightarrow \mathbf{F}^{-T}(\mathbf{X}) \cdot \mathbf{k}(\mathbf{X})$$

where $\mathbf{F}(\mathbf{X}) \equiv \partial \mathbf{x} / \partial \mathbf{X} = \mathbf{grad}(\mathbf{x})$ is the deformation gradient tensor. Diffusion MRI in the beating heart with a mixing time of one cardiac cycle will in general measure an observed diffusivity $\mathbf{D}^{obs}$ different from the value $\mathbf{D}_0$ that would be found were this heart not beating. As derived in Section 1.6.2, they are related at any location $\mathbf{X}$ by

$$\mathbf{D}^{obs} = \langle \mathbf{U}(t)^{-1} \cdot \mathbf{D}_0 \cdot \mathbf{U}(t)^{-1} \rangle_\Delta \, , \tag{4.1}$$

where $\mathbf{U}(t) = (\mathbf{F}^T \cdot \mathbf{F})^{1/2}$ is right stretch tensor at time t.

Using $\mathbf{U}^{-1} = (\mathbf{1} + 2\mathbf{S})^{-1/2} = \mathbf{1} - \mathbf{S} + 3/2\, \mathbf{S}^2 \cdots$, expanding Eq. 4.1 to first order in strain tensor $\mathbf{S}$, we obtain at any location $\mathbf{X}$

$$\begin{aligned} \mathbf{D}^{obs} &\approx \mathbf{D}_0 - \langle \mathbf{S}(t) \cdot \mathbf{D}_0 + \mathbf{D}_0 \cdot \mathbf{S}(t) \rangle_\Delta \\ &= \mathbf{D}_0 - \langle \mathbf{S}(t) \rangle_\Delta \cdot \mathbf{D}_0 - \mathbf{D}_0 \cdot \langle \mathbf{S}(t) \rangle_\Delta \, . \end{aligned} \tag{4.2}$$

A sweet spot is defined as a time Ψ relative to which mean strain over the cardiac cycle is zero, $\langle \mathbf{S}_\Psi(t) \rangle_\Delta = \mathbf{0}$, at all myocardial locations $\mathbf{X}$, giving $\mathbf{D}^{obs} \approx \mathbf{D}_0$. Intuitively, the strains relative to such time-points go through balanced positive and negative deflections in one cardiac cycle, and therefore the net effect of strain on MR diffusion encoding is zero to first order. It follows that the cardiac cycle normally contains two sweet spots, one during mid-ejection, and a second in mid-filling.

The existence of times Ψ in the normal cardiac cycle relative to which the mean strain $\langle \mathbf{S}_\Psi(t) \rangle_\Delta$ is zero for the entire myocardium is a consequence of the synchrony of the normal motion. Using principal component analysis (PCA) of myocardial strain we have previously shown [95] that in normal motion, the components of the myocardial strain tensor are highly correlated. In reference coordinates at end-diastole, myocardial strains through the cardiac cycle history are well approximated by a net systolic strain $\mathbf{S}$ times a scalar function of time, F(t), that represents the "principal time-course" of myocardial strains varying between 0 at end-diastole to 1 at end-systole:

$$\mathbf{S}(t) \approx F(t)\, \mathbf{S} \tag{4.3}$$

In the normal human subject, Eq. 4.3 models myocardial strains with an accuracy of better than 90% [95]. Under a change of coordinates, the strain history with reference to the configuration at time t' is

$$\mathbf{S}_{t'}(t) \approx (F(t) - F(t'))\, \mathbf{S}_{t'} \tag{4.3'}$$

By substituting Eq 4.3' into Eq 4.2 we have $\mathbf{D}^{obs}{}_{t'}$, the diffusion observed at t',

$$\mathbf{D}^{obs}{}_{t'} \approx \mathbf{D}_0 + (F(t') - \langle F \rangle_\Delta)\, (\mathbf{S}_{t'} \cdot \mathbf{D}_0 + \mathbf{D}_0 \cdot \mathbf{S}_{t'}) \ . \tag{4.4}$$

A sweet spot becomes a time Ψ in t' such that

$$F(\Psi) = \langle F \rangle_\Delta \tag{4.5}$$

so that $\mathbf{D}^{obs}{}_{\Psi} \approx \mathbf{D}_0$. As F(t) is continuous and periodic, it is a corollary of the mean value theorem that such points exist.

To localize the sweet spot in practice, we note that by Eq. 4.3, all scalar functions linear in myocardial strain are proportional to F(t) and specify identical sweet spots. In practice, the function we will use is the time-course of radial strain, averaged throughout myocardial voxels in a mid-ventricular slice, $\bar{s}_{rr}(t)$. Use of the radial component confers high signal-to-noise ratio (SNR), and use of the slice-average references this parameter to an approximately constant material volume. As pointed out by Zhu et al., cardiac displacements normal to such a slice are less than its thickness, here 7 mm [96]. To determine this time course, we acquire a conventional phase contrast NMR movie of myocardial strain rates and from it we compute the myocardial average of the radial strain rate at the time frame i, $\bar{s}'_{rr}(i)$. Radial strain rate at each pixel is calculated by $s'_{rr} = \mathbf{r}^T \cdot \mathbf{S}' \cdot \mathbf{r}$ for $\mathbf{S}'$ is the myocardial strain rate tensor, and $\mathbf{r}$, the ventricular radial unit-vector at each voxel [49]. While it would be tempting to suppose that $\bar{s}_{rr}(i) = \Sigma_{j = 1,\ldots,i}\ \Delta_j\ \bar{s}'_{rr}(j)$, this is inaccurate because each $\bar{s}'_{rr}(i)$ is defined in a different coordinate system: the Cartesian coordinate x_i established at the acquisition of the i-th movie frame. The coordinate x_{i+1} is related to x_i by a stretch U_i, $x_{i+1} = U_i\, x_i$, where $U_i \approx (1 + \Delta_i\ \bar{s}'_{rr}(i))$ for Δ_i is the length of the i-th cine time step. Using this, the needed time-course is

$$\bar{s}_{rr}(i) = \Sigma_{j = 1,\ldots,i}\ q(j)\ \Delta_j\ \bar{s}'_{rr}(j)\ ;$$

$$q(j) = \prod_{k = 1,..,j} (1 + \Delta_k\ \bar{s}'_{rr}(k)) \tag{4.6}$$

where q(j) is the net coordinate re-scaling from the first up to the j-th time point. Using the discrete time-series data of Eq. 4.6, we extend $\bar{s}_{rr}(i)$ to a continuous function $\bar{s}_{rr}(t)$ by interpolation, and then determine the sweet spot according to Eq. 4.5, solving for Ψ such that $\bar{s}_{rr}(\Psi) = \langle \bar{s}_{rr}(t) \rangle_\Delta$.

4.3 Experiments and Results

To confirm our theory, we tested the prediction that the trace ADC measured at the sweet-spot is equal to the average trace ADC's measured over the cardiac cycle. We then tested the capacity of sweet spot MRI to reliably define the myocardial fiber architecture as seen by conventional diffusion MRI in the isolated non-beating heart.

4.3.1 MRI acquisition methods

Normal volunteers were imaged in a GE/ANMR 1.5 Tesla echo-planar magnet. After giving informed consent, subjects were positioned in the 45° LAO position and a 5 x 11" rectangular receive-only surface coil positioned precordially. Following localization of a mid-ventricular short-axis slice, cardiac strain and diffusion data were obtained. In addition to routine ECG triggering, synchronized breathing was used to suppress respiratory motion in both strain and diffusion studies: with TR = 5 cardiac cycles, the subject upon hearing the scan pulse took one breath, then exhaled normally and kept still for next scan that followed within 4 s. This paradigm was learned in all cases in a single training run of 1 min and was easily sustained for the 5 – 10 min scan periods. Both diffusion and strain acquisitions were spatially encoded using single-shot EPI with spatial resolutions of 3 x 3 x 7 mm.

A conventional phase-contrast NMR movie of myocardial strain rates was first obtained for sweet spot localization. This was an SE 50 sequence, TR = 5 R-R intervals augmented with bipolar gradient pulses of velocity sensitivity K_v =1.2 radian s mm^{-1}, and of tetrahedral orientation [49, 97], with a full-k acquisition. Using a progressive ECG delay of 32 ms and 1 average, movies of at least 30 frames were acquired in about 8 min. From these data, the radial component of the myocardial strain-rate tensor was computed, and from this, the location of the mid-systolic sweet spot location identified as described above.

Diffusion tensor MRI was acquired by double-gated stimulated-echo sequence, in which the two diffusion-encoding gradient pulses are located at identical delays from ECG R-wave trigger in consecutive cardiac cycles [68, 70, 98]. These pulses were applied in orientations corresponding to the 6 non-opposed edge-centers of a cube, and were of intensity $\|\mathbf{g}\|$ = 1 gauss cm^{-1}, duration δ = 7.6 ms and mixing time Δ_D = 1 R-R interval, normally $\approx$ 820 ms, corresponding to a diffusion sensitivity $b = 4\pi^2 \Delta_D k^2 \approx 340$ s mm^{-2} where k is the spatial modulation $k = (1/2\pi)\gamma\delta\|\mathbf{g}\| = 3.2$ mm^{-1}. From these data, the diffusion tensor image was computed by b-matrix inversion as described in Eq. 1.9 [67, 99-101].

4.3.2 Trace ADC movie

Using the linearity of observed diffusion in material strain expressed in Eq. 4.2, we test the prediction that

$$\langle \mathrm{trace}(\mathbf{D}^{obs}{}_{t'}) \rangle_{\Delta} \approx \mathrm{trace}(\mathbf{D}^{obs}{}_{\Psi}). \quad (4.7)$$

Following acquisition of strain data and sweet spot computation as described above, we acquired a time-series of mid-ventricular diffusion tensor images using a progressive ECG delay 50 ms, for 10 frames in total. These acquisitions each required about 5 min.

Results are shown in Fig. 4.2, where the time-course of ventricular mean trace of apparent diffusion coefficient (ADC) and the mean trace ADC of the single image acquired at the cardiac sweet spot are compared. We see a cyclical change of the mean trace($\mathbf{D}^{obs}{}_{t'}$) with dynamic range from 3.4 ± 0.1 ($\times 10^{-5}$ cm^2 s^{-1}, mean $\pm$ 95% confidence interval) at end-systole to 4.2 ± 0.1 at end-diastole . Applying Eq. 4.6 to the strain-rate move, the mid-systolic sweet spot was localized to a trigger delay $\Psi = 192 \pm 15$ ms; we find $\langle \mathrm{trace}(\mathbf{D}^{obs}{}_{t'}) \rangle_{\Delta} = 3.8 \pm 0.1$ and $\mathrm{trace}(\mathbf{D}^{obs}{}_{\Psi}) = 3.7 \pm 0.1$, obtaining good agreement.

4.3.3 Myocardial architecture

To evaluate its capacity to faithfully image myocardial architecture, multislice diffusion tensor MRI data acquired at the sweet spot were compared to conventional diffusion tensor MRI of human cardiac necropsy specimens.

Imaging 5 normal volunteers, following determination of the mid-systolic diffusion sweet-spot using strain-rate MRI as described above, cardiac diffusion MRI was acquired at the sweet spot, and diffusion tensor fields computed. With 7 slices (short axis, 1 cm gaps) and 16 averages, total acquisition times were approximately 30 min and net SNRs were 40:1 for unattenuated ($b \approx 0$) and 20:1 for attenuated ($b \neq 0$) images.

Analysis of fiber architecture is performed in local cardiac coordinates. Axes of local cardiac coordinates at each myocardial point are defined by tangentials of three arcs parametrized by prolate spheroid coordinates, which in turn are determined by fitting an ellipsoid to the epicardial contour. Given the diffusion tensor field, we identify the first eigenvector with the orientation of the myocardial fiber vector **f**. The direction of **f** is assigned as the one having smaller angle to the circumferential vector. Fiber helix angle is the angle in the epicardial tangent plane between the projection of the fiber orientation and the circumferential direction.

Fiber helix angle maps in both *in-vivo* and *ex-vivo* studies (Fig. 4.3a and b) show smooth and continuous variation of the fiber orientations from epicardium ($\approx -90^{o}$) to endocardium

($\approx 90^{o}$). The spatial pattern of fiber orientations is highly circular symmetric, and varies little from apex to base. Both helix angle histograms (Fig. 4.3c and d) show a similar pyramid pattern, achieving maxima near 0° (fibers of circumferential orientation), declining symmetrically toward minimal at the densities at +/- 90°.

Imbrication angle maps in both studies show the same characteristic pattern of spatial distribution (Fig. 4.4 a and b). Positive angles are mainly in the anterior wall near base, and posterior wall around the RV insertion, whereas negative angles are mainly in the posterior wall near apex, and anterior wall around the RV insertion. In the septum, there is a clear transition of the angles from negative at the anterior, through zero, to positive at the posterior. Apex-to-base shift of the mean imbrication angles is still present, with a smaller slope, however. Sheet angle maps also show a clear septum-versus-free-wall polarization pattern of the sheet angle sign in both cases (Fig. 4.5 a and b). Bimodal distribution of the sheet angles in the *in-vivo* case is more conspicuous than that in the *ex-vivo* heart that was in rigor mortis.

4.4 Discussion

The purpose of this work is to bypass the complication of strain effect encountered in MR measurement of myocardial diffusion *in vivo*, and propose an efficient method to directly acquire diffusion data that reliably depict the fiber architecture. To achieve this purpose, we first show that given a periodic and synergic cardiac motion, there exist unique time points relative to which mean myocardial strain over the cardiac cycle vanishes. Recognizing this, it follows that if the diffusion sensitizing gradient pulses are placed at these points (sweet spots), the strain effect on the measured diffusivity is reduced to a minimum. In practice, we propose a strain rate movie technique to localize sweet spot positions according to which diffusion MRI can be performed. Using this method we are able to obtain multislice diffusion MRI *in vivo* with consistent patterns of fiber orientations as compared to those obtained *ex vivo*. Therefore, we claim that MR diffusion measurement at the sweet spots effectively alleviates strain effect and provides diffusion data that faithfully reveal the myocardial fiber architecture.

The success of this method hinges on two key assumptions: first, the effect of strain on diffusion measurement is linear, second, myocardial strain is synchronous. Based on these two assumptions, some crucial approximations are made to find a simpler solution to the strain problem. By doing so, the accuracy of the results with the sweet spot method is undoubtedly compromised. The question is then how reliable this method can be. Sources of error in applying these two assumptions are discussed, and their magnitudes are assessed as follows.

4.4.1 Synchrony assumption

The assumption of cardiac synchrony is based on the result of principal component analysis of a myocardial strain rate history in the normal heart: the first eigen-image constitutes about 90 – 95% of relative contribution to the original strain rate image . The essence of the synchrony assumption is that it allows a dramatic simplification of the description of the strain history of the whole LV; it needs only a single strain image and a single time course function to reach a good approximation. It also ensures that temporal behavior of the strain tensor is position- and component-independent, hence, existence of unique sweet spots. Given this latitude, two approximations are made to locate sweet spots in practice: first, the original strain rate image approximates the first eigen-image, second, the time course of radial strain approximates that of other strain components. The errors from these two approximations will affect the accuracy of sweet spot positions, so in this section, we will assess the amount of these errors.

The error caused by taking the original strain rate image as the first eigen-image can be estimated by randomly subtracting 5 to 10% from the radial strain rate at each time frame, and from this repeating the calculation of sweet spot positions. We find that the deviation is smaller than 2 ms. As for the error caused by the second approximation (radial time course also applies to other components) we can calculate alternatively sweet spot positions with circumferential strains. We find that deviation of the sweet spot positions is smaller than 15 ms. From Eq. 4.4, it is clear that the fractional error given a deviation from the sweet spot is proportional to twice the strain S with respect to the sweet spot:

$$\|\mathbf{D}^{obs}_{t'} - \mathbf{D}^{obs}_{\Psi}\| \, \|\mathbf{D}^{obs}_{\Psi}\|^{-1} = 2\,S \ . \qquad (4.8)$$

Knowing that S_{max} ($S_{max} \leq 0.4$) is the maximum strain during the ejection phase of about 200 ms long, strain in 15 ms intervals corresponds to 0.03, and so the fractional error of diffusion is at maximum 6%.

4.4.2 Linear assumption

In Eq. 4.2, the strain effect is expressed only in linear terms. This approximation is based on the assumption that the strain effect is predominantly linear. To assess the error arising from truncating higher order terms of strain effect in Eq 4.2, we evaluate the magnitude of the quadratic term because it represents the upper bound of this error. Using $\mathbf{U}^{-1} = \mathbf{1} - \mathbf{S} + 3/2\,\mathbf{S}^2 \ldots$ to expand Eq. 4.1 up to second order in $\mathbf{S}$, and knowing $\mathbf{S}_{t'}(t) \approx (F(t) - F(t'))\,\mathbf{S}_{t'}$ (Eq. 4.3'), we have

$$\mathbf{D}^{obs}_{t'} \approx \mathbf{D}_0 - \langle \mathbf{S}_{t'}(t)\cdot\mathbf{D}_0 + \mathbf{D}_0\cdot\mathbf{S}_{t'}(t) - 3/2\ \mathbf{S}_{t'}(t)^2\cdot\mathbf{D}_0$$
$$- \mathbf{S}_{t'}(t)\cdot\mathbf{D}_0\cdot\mathbf{S}_{t'}(t) - 3/2\ \mathbf{D}_0\cdot\mathbf{S}_{t'}(t)^2\rangle_\Delta$$
$$\approx \mathbf{D}_0 + (F(t') - \langle F\rangle_\Delta)\ (\mathbf{S}_{t'}\cdot\mathbf{D}_0 + \mathbf{D}_0\cdot\mathbf{S}_{t'})$$
$$+ \langle (F(t) - F(t'))^2\rangle_\Delta\ (3/2\ \mathbf{S}_{t'}^2\cdot\mathbf{D}_0 + \mathbf{S}_{t'}\cdot\mathbf{D}_0\cdot\mathbf{S}_{t'} + 3/2\ \mathbf{D}_0\cdot\mathbf{S}_{t'}^2)\ .$$

At the sweet spots, $t' = \Psi$, the linear strain effect vanishes because $\langle F\rangle_\Delta = F(\Psi)$ (Eq. 4.5).

To estimate the amount of quadratic strain effect at the sweet spots, we use the actual time course of strain F(t) obtained from the strain rate movie and find that the value of $\langle (F(t) - F(\Psi))^2\rangle_\Delta$ is 0.1. In normal cardiac motion, the maximum normal strain in any particular direction, or the leading eigenvalue of the strain tensor, rarely exceeds 0.4 ($S_{max} \le 0.4$). So the maximal fractional error of diffusion caused by the quadratic term can be estimated as

$$\|\mathbf{D}^{obs}_\Psi - \mathbf{D}_0\|\ \|\mathbf{D}_0\|^{-1} = \langle (F(t) - F(t'))^2\rangle_\Delta\ 4\ (S_{max})^2 \approx 6\%.$$

Though we derived sweet spots based on Reese's model (Eq. 4.1), it should be noted that the existence of the sweet spots is a general attribute of any model with predominant linear dependency on diffusion and strain. As long as the strain effect can be reliably described within the context of linearity, the conclusion of the sweet spots we made is still valid.

4.4.3 Movie method

In using the movie method to obtain strain rate or trace ADC history, data were acquired at a fixed plane at mid-ventricular level without compensation for through-plane motion. An error arises when we approximate LV pixels at different time frames to be the same material population in computing spatial average of radial strain rates or trace ADC's. Through plane motion on a short-axis slice comes from longitudinal translation, longitudinal strain as well as circumferential-radial and longitudinal-radial shears. To simplify the estimate of this error, we only consider the major source of through plane motion: longitudinal translation. During cardiac contraction, longitudinal translation toward the apex occurs with maximum at the basal region and minimum at the apex [102]. At mid-ventricular level, this to-and-fro longitudinal translation makes up about 7 mm in range between end-systole and end-diastole. This means the material populations of data taken from the movie method vary within 7 mm. However, from 3D myocardial strain analysis of the canine heart, it is shown that longitudinal variation of radial strain within 7 mm is about 1% [22]. As compared to the average radial strain 30%, the error due to longitudinal translation within 7 mm in range is negligible. Similarly, in the trace ADC movie, this amount of through plane motion has little effect on the mean trace ADC.

Another error arises from the way we define radial vectors; they are all fixed on the imaging plane. Radial strain may be underestimated if during the cardiac cycle the radial vector tilts away

from the imaging plane owing to rigid body rotation. Though this rotation is possible, the range of rotational angle is measured to be within 5° only [103]. As for trace ADC, it is coordinate-invariant, and does not contribute to error.

4.5 CONCLUSION

To address the problem of strain effect on the myocardial diffusion measurement using STE-EPI sequence, we show that there exist sweet spots, one at mid-systole and the other at mid-filling, at which the strain effect vanishes up to the first order. These two points can be localized by a 2D strain rate movie using a conventional phase contrast technique. Multislice diffusion MRI at the sweet spot demonstrates characteristic patterns of fiber architecture that are in good agreement with those obtained *ex vivo*. Error estimates show approximately 90% accuracy attainable by this method. We conclude that MR diffusion measurement at the sweet spots can reliably reveal the myocardial fiber architecture.

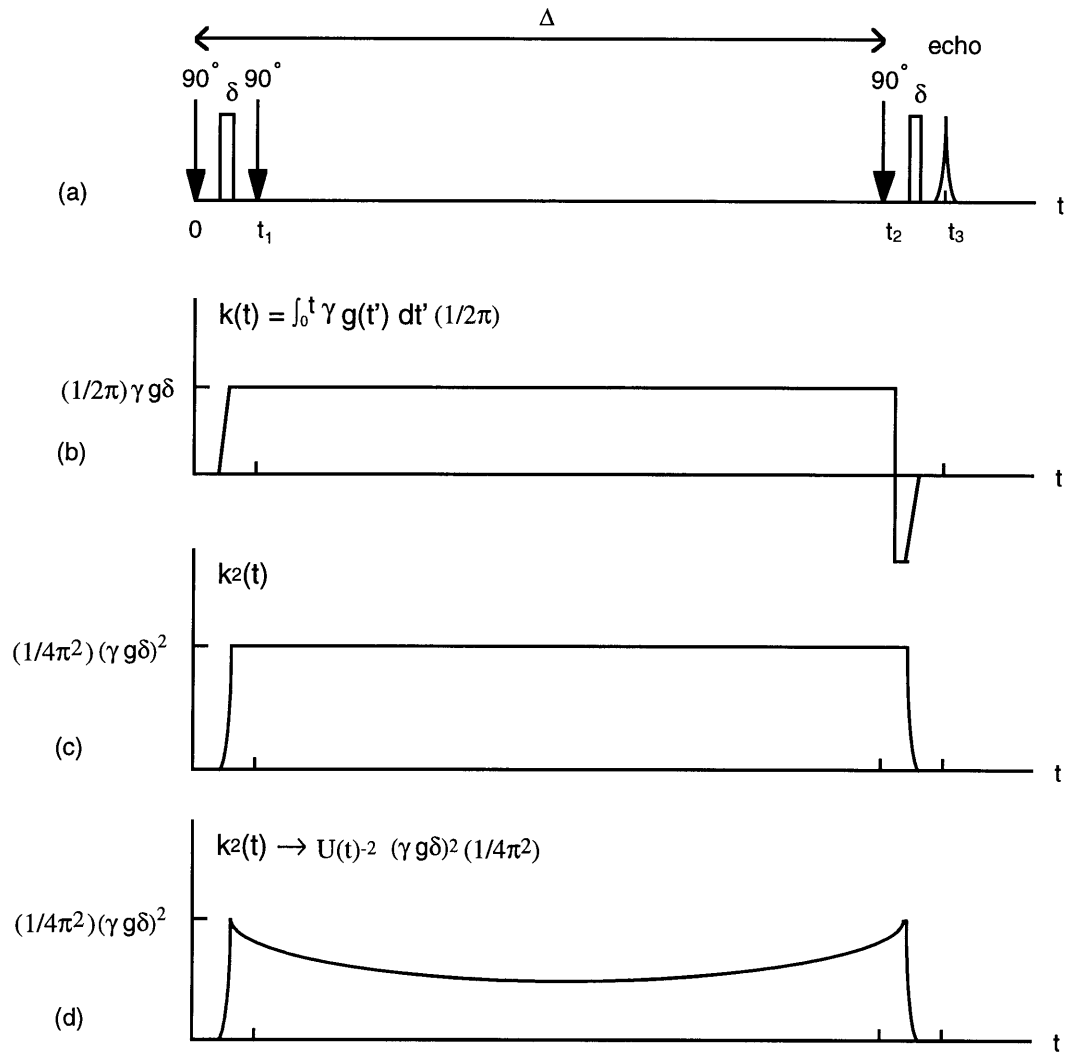

Figure 4.1 Pulsed gradient stimulated-echo diffusion sequence (a). Diffusion-sensitizing gradients are applied one at the time between the first and second 90° RF pulses, another between the third 90° RF pulse and the echo. In double-gating STE-EPI diffusion experiment, diffusion time Δ equals 1 R-R interval, and $\delta << \Delta$. If the measured sample is stationary, the curves of k(t) and $k(t)^2$ are shown in (b) and (c). If the same experiment is performed in the beating heart, with diffusion-sensitizing gradients applied at end-diastole, the evolution of $k(t)^2$ in radial direction is affected by the material stretch $U(t)^{-2}$.

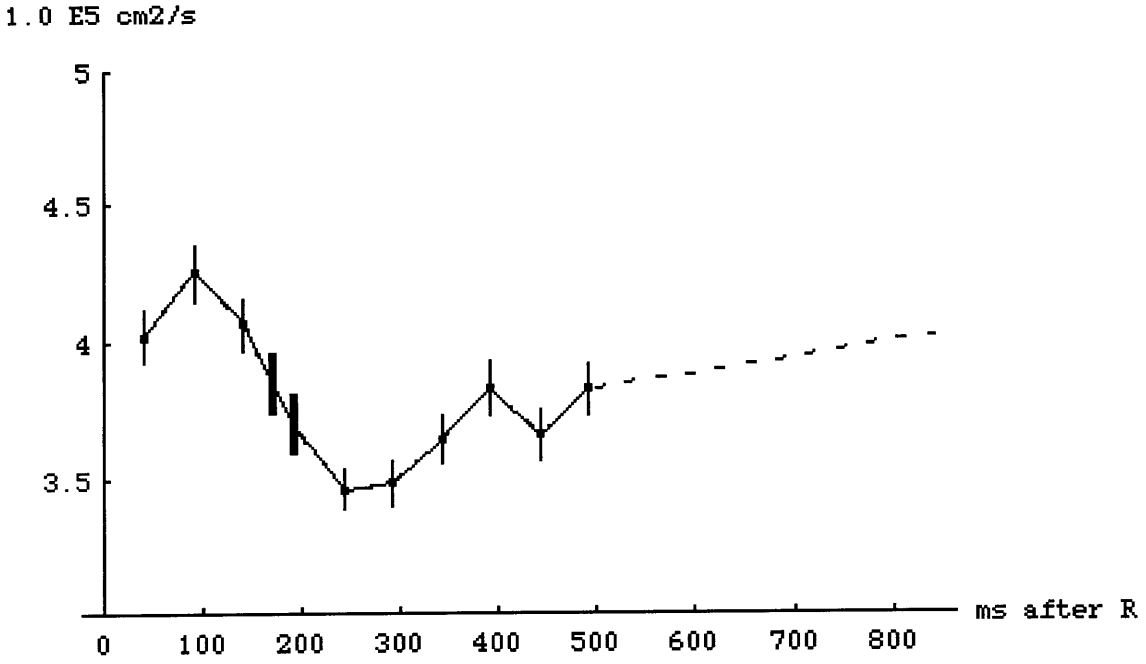

Figure 4.2 The time-course of mean trace ADC over the cardiac cycle and the mean trace ADC of the single image acquired at the cardiac sweet spot. The mean trace ADC at each time point is indicated by a dot with a fine bar expressing 95% confidence interval. The dash line from 500 to 840 ms after R-wave is obtained by interpolation. The coarse vertical bar on the left indicates the time average of the mean trace ADC, $\langle \mathrm{trace}(\mathbf{D}^{obs}_{t'}) \rangle_{\Delta} = 3.8 \pm 0.1$ (x 10^{-5} cm^2 s^{-1}). Another coarse vertical bar on the right is the mean trace ADC at the systolic sweet spot, $\mathrm{trace}(\mathbf{D}^{obs}_{\Psi}) = 3.7 \pm 0.1$.

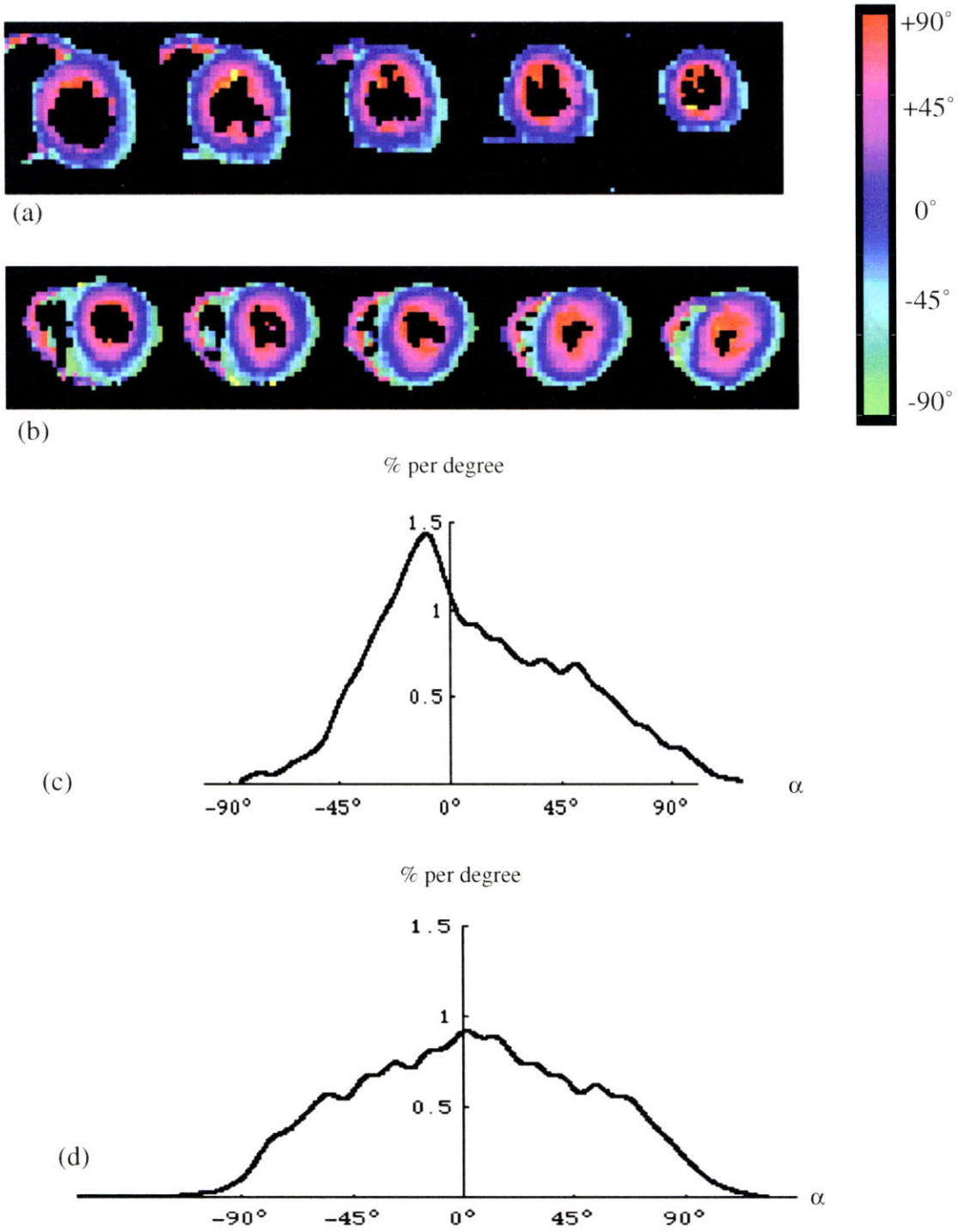

Figure 4.3 Fiber helix angle (α) maps and the corresponding histograms in the beating heart: (a) and (c), and the cadaver heart: (b) and (d). The spatial distributions of the helix angles are circularly symmetric in both cases. Both histograms show predominant circumferential fiber populations.

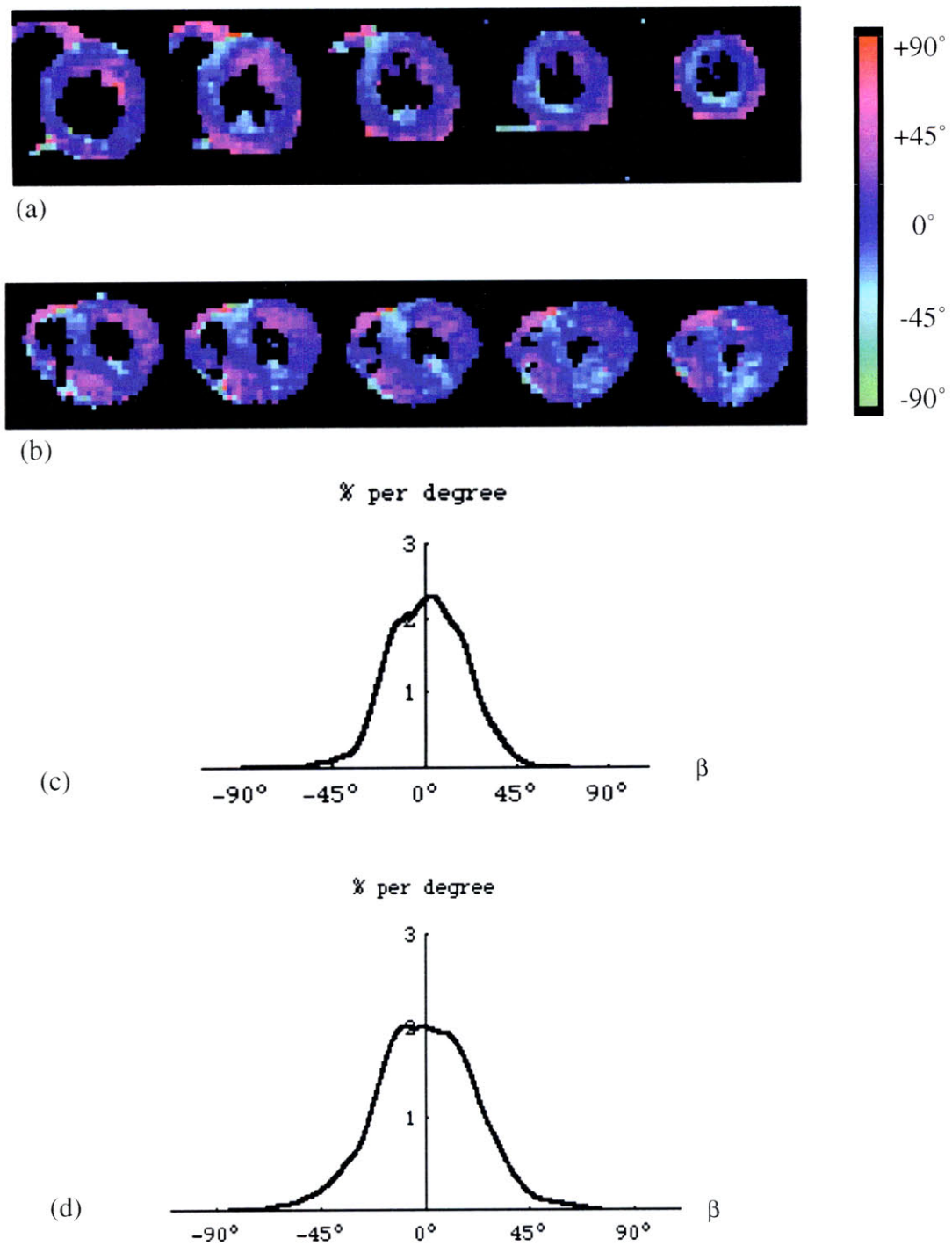

Figure 4.4 Imbrication angle (β) maps obtained *in vivo* (a), *ex vivo* (b), and the corresponding histograms for *in-vivo* case (c) and *ex-vivo* case (d).

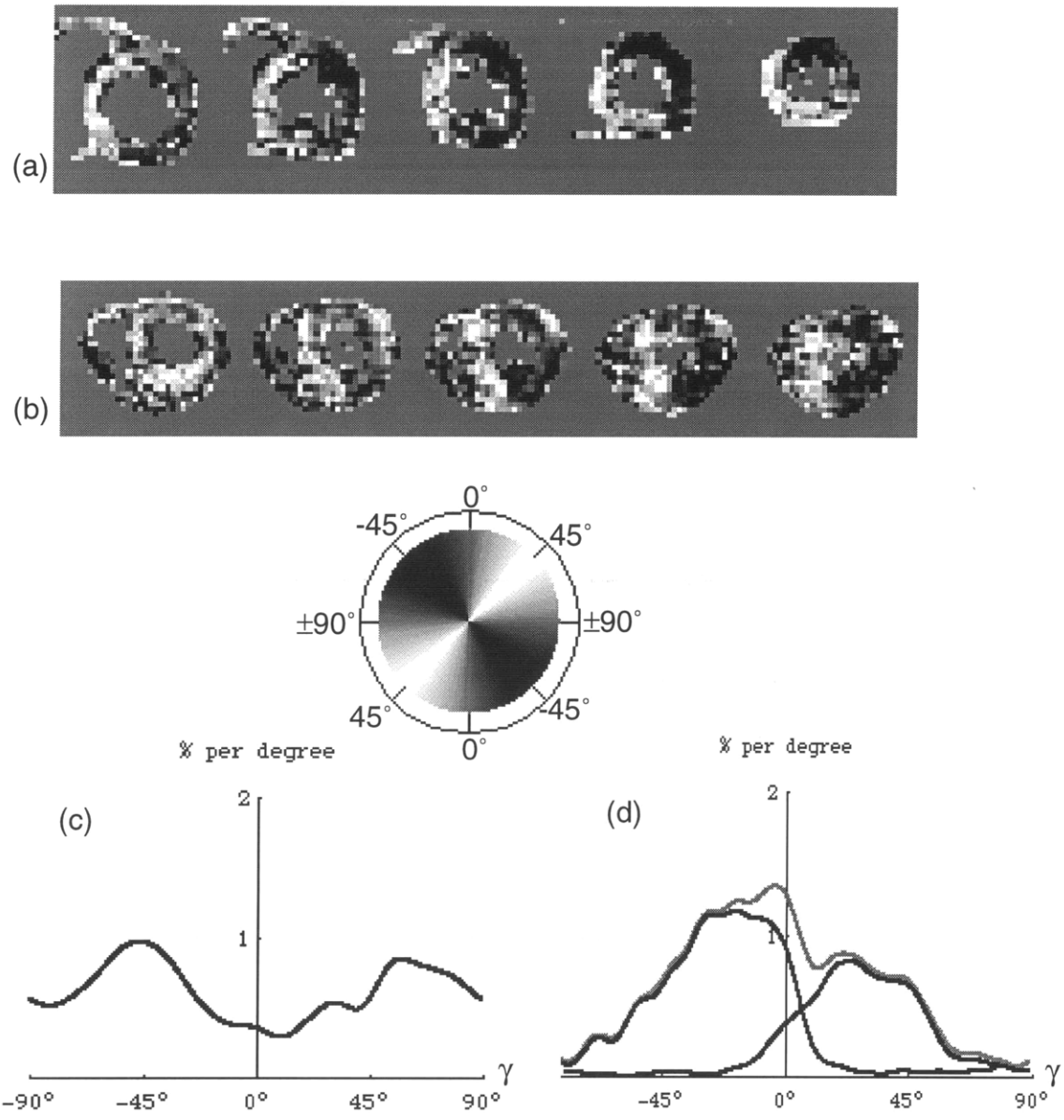

Figure 4.5 Sheet angle (γ) maps obtained *in vivo* (a), *ex vivo* (b), and the corresponding histograms for *in-vivo* case (c) and *ex-vivo* case (d).

Chapter 5

Noninvasive Imaging of Human Myocardial Fiber and Sheet Functions using Magnetic Resonance

5.1 Introduction

While the relationship of myocardial architecture to ventricular function has long been of great interest, experimental progress has been impeded by the difficulties of assessing myocardial architecture [71]. Using diffusion-sensitive MRI, it has recently become possible to noninvasively map myocardial fiber architecture in the intact excised heart and *in vivo* [61, 70]. In Chapter 4 we have demonstrated a practical way to trivialize the strain effect on the STE-EPI diffusion measurement; it greatly reduces the scanning time and avoids the complex correction scheme, making application of this technique to the human study more feasible and robust. In the present chapter, MRI of myocardial architecture is combined with velocity-sensitive MRI of myocardial strain to map myocardial fiber shortening and sheet slippage quantitatively in the human. To

reveal functional significance of the myocardial fiber and sheet organizations, they are then related to the local geometry of myocardial deformation during contraction.

Since the modern clarification by Streeter and colleagues of the unique structure of the ventricular myocardium, considerable progress has been made in rationalizing myocardial architecture in terms of ventricular mechanics, expressing myocardial structure and function as jointly optimal solutions to specific design problems [13, 16, 24, 104-106]. Of experimental approaches to myocardial design, among the most fruitful have been direct comparisons of local myocardial fiber architecture and myocardial function, defined as the patterns of myocardial deformation during the cardiac cycle [21, 22, 30, 31]. On a technical level, these studies have addressed a common challenge. While myocardial function can now be measured *in vivo* by any of several methods, myocardial architecture is assessed by light microscopy of myocardial specimens *ex vivo* . This limitation has significant consequences, for while the measurements of myocardial function can be three-dimensional, dynamic, noninvasive and repeatable, optical measurements of myocardial architecture do not share these characteristics. Moreover, accurate geometric registration of functional data with conventional histology remains problematic and continues to occasion technical innovation [80].

To address the limitations of microscopy for the assessment of myocardial architecture, investigation has turned to noninvasive technologies. For example, using backscatter ultrasound, the innovative studies of Wickline showed the sensitivity of this modality to myocardial fiber orientation and its capacity *ex vivo* to reconstruct myocardial fiber 3D orientation by multi-angle tomography [107]. Following demonstration by Moseley of the capacity of diffusion-sensitive MRI to detect the material anisotropy of biologic tissues, methods were devised to map with MRI the 3D architecture of fibrous tissue including cerebral white matter and the myocardium, and subsequently, to characterize and control the effects of cardiac motion to image myocardial architecture *in vivo* [61, 70, 98, 108, 109]. In a parallel development, MRI methods have moved to the forefront of myocardial function measurement, and now can noninvasively provide high resolution images of myocardial strain fields in 2 and 3 dimensions [40, 49, 110]. Given these methodologies, we combine diffusion NMR images of myocardial architecture with registered NMR images of myocardial 3D strains obtained under unaltered physiologic conditions, sampled on an identical grid of equal resolution and from these, define myocardial structure-function relations by simple operator-independent algebraic manipulation of the digital image data. By addressing the aforementioned issues of invasiveness and intermodality registration and synthesis, ventricular coverage and reproducibility, this approach enables efficient and relatively comprehensive examination of myocardial structure and function *in vivo*.

The specific goals of this study are: 1) to define a practical protocol for registered diffusion and strain MRI in humans, 2) to compute quantitative images of fiber and sheet orientations and of

the myocardial systolic strain tensor field, 3) to analyze the relationships between myocardial strain and the orientations of the fibers and the sheets to investigate their functional roles.

5.2 Theory

Based on the finding that myocardial fiber orientation in the normal heart is indicated by the leading eigenvector **f** of the local water diffusion tensor **D** at each location, relations between myocardial fiber architecture and function are defined by correlating myocardial fiber orientation with the myocardial systolic 3D strain tensor (boldface denotes vector and tensor quantities; eigenvectors are normalized). The principal example of this is computation of net systolic fiber shortening S_{ff} as the component of net systolic strain tensor $\mathbf{S}_{sys}$ along the unit vector **f**

$$S_{ff} = \mathbf{f}^T \cdot \mathbf{S}_{sys} \cdot \mathbf{f} \ . \tag{5.1}$$

This definition can be generalized to quantify dynamics (including normal strain and shear strain) of any structural components, the orientations of which can be furnished by MR diffusion tensor imaging. To obtain these quantities, an image of myocardial architecture and an image of systolic strain tensor are needed. As we have shown in Chapter 4, 3D orientation of the local myocardial structure can be obtained reliably from strain-free diffusion measurement at the sweet spots. In the first part of the section, we revisit the basis for the whole methodology: cardiac synchrony. Based on this, not only we verify the existence of the sweet spots, but also know how to localize them efficiently using the time course of the strain rate. To compute the net systolic strain, we evoke this time course again; with it, we are able to rescale the strain rate image appropriately to obtain the image of net systolic strain. The idea of determining the time course and computing the net systolic strain is stated in the second part of the section.

5.2.1 Cardiac synchrony

The present MRI methodology takes advantage of the following simplification of myocardial motion known to be valid in the normal heart. Owing to the synchrony of the local strains of cardiac contraction, it has been found in the normal the strain-rate history of the myocardium in material coordinates **X**, $\mathbf{S}'(\mathbf{X}, t)$, may be approximately factored as

$$\mathbf{S}'(\mathbf{X}, t) \approx f(t)\ \mathbf{S}'(\mathbf{X}, \tau) \tag{5.2}$$

or, integrating strain-rate to find the material strain relative to time 'τ', $\mathbf{S}_\tau(\mathbf{X}, t)$,

$$\mathbf{S}_\tau(\mathbf{X}, t) \approx F_\tau(t)\ \mathbf{S}'(\mathbf{X}, \tau) \tag{5.3}$$

where $\mathbf{S}'(\mathbf{X}, \tau)$ is the single image of the myocardial 3D strain-rate tensor field measured at time

'τ', f(t) is a scalar function describing the time-course of the myocardial contraction and $F_\tau(t)$ is the time-integral of f(t') from t' = τ to t' = t (see below) [49].

Equations 5.2 and 5.3 are essential in the present MRI experiments in three ways. Firstly, the current MRI measurements of myocardial diffusion, based on a diffusion encoding that spans a cardiac cycle, are sensitive to the history of myocardial strains throughout the cycle, and in general require a complex strain correction [68, 70]. By Eq. 5.3, there exist special points in the normal cardiac cycle when this effect on the measured diffusion tensor **D** is negligible. These times Ψ occur when cardiac configuration approximates its mean value over one cardiac cycle, so that $\langle F_\Psi(t) \rangle_\Delta = 0$. At these times, the effects of myocardial strain on the diffusion measurement are zero to first order and are negligible. Using the cardiac diffusion MRI acquisition of Edelman et al., cardiac diffusion data encoded at such times, is accurate as acquired, without the need for strain correction. The authors call such time points "sweet spots"; the normal cardiac cycle has two sweet spots, one in mid-contraction and one in mid-filling. Secondly, Eq. 5.3 makes possible a practical method to experimentally identify the locations of these sweet spots. To do this, F(t) is measured using a conventional 2D MRI movie of one component of myocardial strain. The measured signal will be proportional to F(t) by Eq. 5.3. Thirdly, Eq. 5.3 is used to reconstruct the myocardial net systolic 3D strain tensor field by combining f(t) and a single image of the myocardial 3D strain-rate tensor field $\mathbf{S}'(\mathbf{X}, \Psi)$.

5.2.2 Localization of the sweet spot

As f(t) is proportional to any linear function of material strain-rates, 2D images of a single in-plane component of myocardial velocity are obtained at a series of time-points t_i, and the myocardial mean radial strain-rate $\underline{S}_{rr}'(t_i)$ estimated as previously described in Chapter 4 [49]. The radial component of strain-rate is chosen for its high SNR. Setting $f(t_i) = \underline{S}_{rr}'(t_i)$, $F(t_i)$ represents the time-course of mean radial strains. Referenced to the configuration at $t = t_0$, $F(t_i)$ is given by summing the s_i with rescaling for the cumulative stretch

$$F(t_i) = \Sigma_{j = 1,\ldots,i}\ q_j^{\,2}\ s_j \qquad (5.4)$$

where s_j represents the j-th interval strain

$$s_j = f(t_j)\ \delta t_j$$

where $\delta t_j = t_j - t_{j-1}$ is the size of j-th time-step, and q_j is the cumulative stretch from $t = t_0$ to $t = t_j$

$$q_j = \Pi_{k = 1,..,j-1}\, u_k \ ;$$

for $$u_k = (1 + 2\ s_k)^{1/2}$$

where u_k represents the stretch during the k-th interval. Sweet spots are determined from the interpolated curve of $F(t_i)$ as points Ψ such that $F(\Psi) = \langle F(t) \rangle_\Delta$ [111]. An example of such a

curve and its sweet-spots is shown in Fig. 5.1; the normal cardiac cycle contains mid-systolic and mid-diastolic sweet spots, respectively Ψ and Ψ'.

5.2.3 Net systolic strain

To compute the net systolic strain tensor image $\mathbf{S}_{sys}$, a high-SNR image of the 3D strain-rate tensor $\mathbf{S}'(\Psi)$ is acquired at the systolic sweet spot Ψ, registered to the diffusion data and rescaled as follows. By Eq. 5.4, the net systolic strain tensor field, expressed in the material coordinates established at the systolic sweet spot $\tau = \Psi$, is

$$\mathbf{S}_{sys} = \xi\, \mathbf{S}'(\Psi)$$

where $$\xi = [\underline{S}_{rr}'(\Psi)]^{-1} \int_{sys} \underline{S}_{rr}'(t)\, dt \ ; \qquad (5.5)$$

the integral is computed from the $\underline{S}_{rr}'(t_i)$ by interpolation. Intuitively, the net systolic strain is the strain that would be produced if the strain-rates measured at $\tau = \Psi$ were to act continuously for ξ seconds; in the example of Fig. 5.1, $\xi = 0.178$ s.

5.3 Methods

5.3.1 MRI acquisition

Diffusion and strain data are reconstructed from 2D images acquired using single-shot echo-planar MRI (GE/ANMR 1.5 T instrument) with 3 x 3 mm in-plane resolution. Each subject provides written informed consent prior to study under MGH SHS approval. After ECG leads are applied, a rectangular 6 x 11" rectangular receive-only RF surface coil placed over the precordium and the subject placed in the scanner in a 45° LAO orientation. Following conventional ECG-gated sagittal T_1-weighted study to establish left ventricular location and axis, a mid-ventricular short-axis slice is defined for further studies. Registered studies of myocardial strain-rate (movie to determine Ψ, followed by 3D strain-rate tensor image at Ψ) and the study of myocardial diffusion are then acquired as described below. Lastly, a T_1-weighted multislice echo-planar MRI study of the ventricle is acquired gated at Ψ to define the ventricular anatomy.

To suppress the effects of respiratory motion, all of the present images are acquired at a constant respiratory phase of end-expiration using synchronized breathing. With scanning ECG-triggered to every 4th or 5th heartbeat, subjects are requested to take a breath after the sound of each scan pulse, then passively exhale, await the next scan, and repeat. The resulting respiratory rate is within normal limits and can be comfortably sustained for many minutes.

5.3.2 Strain MRI

Strain-rate MRI data are acquired using a conventional ECG gated single-shot echo-planar MRI pulse sequence augmented by a velocity phase-encoding gradient pulse pair. The strain-rate movie used for computation of F(t) is acquired using the in-plane velocities (x and y) for a single slice of 7 mm thickness and a progressive cardiac delay of 30 ms with coverage of an entire cardiac cycle. From these, myocardial radial strain-rates are computed as previously described [49] and the systolic sweet spot Ψ computed as described above. A typical example of the computed curve $F_\Psi(t)$ is shown in Fig. 5.1. A second strain acquisition is then performed furnishing an image of the 3D strain-rate tensor field at the mid-systolic sweet spot, $\mathbf{S}'(\Psi)$. In this image, the full 3D velocity is encoded for two slices offset by 3 mm in the z-direction. The myocardial strain-rate tensor field is computed using Eq. 1.2; its component form is:

$$S_{ij}' = 1/2\ (\partial v_i/\partial x_j + \partial v_j/\partial x_i) \tag{5.6}$$

where v_i and S_{ij}' are the Cartesian components of the velocity field $\mathbf{v}$ and strain-rate tensor field $\mathbf{S}'$, respectively. The spatial derivatives are computed via $\partial v_i/\partial x_j \approx \Delta v_i/\Delta x_j$, the velocity differential between adjacent pixels [49]. This achieves isotropic 3 mm resolution of 3D strain for the imaged slice. Velocity-encoding gradient pulses were applied with cubical orientations: $\{x, y, z\} = \{\pm1, \pm1, \pm1\}$, amplitude $\|\mathbf{g}_v\| = 1$ gauss cm^{-1}, pulse duration $\delta_v = 8.4$ ms and encoding time $\Delta_v = 9$ ms, producing a velocity sensitivity $\|\mathbf{K}_v\| = \gamma\|\mathbf{g}_v\|\delta_v\Delta_v \approx 0.2$ s cm^{-1}, where $\gamma = (2\pi)\ 4258$ s^{-1} gauss^{-1} is the proton gyromagnetic ratio. While this sensitivity typically produces myocardial phase shifts of several cycles, these are removed by the strain calculation of Eq. 5.6 provided phase shifts within each voxel remain less than 180° [49]. The movie of strain rates is acquired using 4 gradient encodes (a tetrahedron within the cube), 1 slice, TR = 2 R-R interval ≈ 1.5 s, 1 average, and a progressive cardiac delay of 30 ms, for a total acquisition time of about 4 min. Data acquisition for image of 3D strain-rate is completed in about 4 minutes: 8 gradient-encodes x 2 slices x 4 signal averages x TR = 5 R-R intervals ≈ 4 s; this provides a strain-rate SNR > 50:1.

5.3.3 Diffusion MRI

Diffusion tensor MRI reconstructs the second-rank symmetric diffusivity tensor at each location in an NMR image. It is based on the diffusion-dependent attenuation of the NMR signal that results from the application of a reversible spatial modulation of magnetization by a pair of temporally separated magnetic gradient pulses of opposite signs. The measured signal is related to the diffusion by

$$\ln[A/A_o] = -4\pi^2 \Delta\, \mathbf{k}_D^T \cdot \mathbf{D} \cdot \mathbf{k}_D \tag{5.7}$$

where A_o and A represent the native and attenuated image intensities, respectively, $\mathbf{D}$ the diffusion

tensor, Δ the diffusion mixing time, and $\mathbf{k}_D$ is the gradient-induced spatial modulation of magnetization which is assumed to be produced in a time $\delta_D \ll \Delta$. By measuring this attenuation for spatial modulations in 6 directions, the diffusion tensor **D** is computed at each image location by algebraic inversion of Eq. 1.9. From this, the local fiber orientation **f** is defined by the leading eigenvector of the diffusion tensor, and the local sheet orientation **s** is defined by the second eigenvector of the diffusion tensor (See Chapter 2).

Registration of this diffusion scan and the strain-rate image $\mathbf{S}'(\Psi)$ requires temporal alignment with respect to the ECG trigger between three corresponding components of the respective scans: 1) readout period for in-plane registration, 2) slice-selection for slice registration, and 3) diffusion- /and velocity-encoding pulses for registration of architecture and function. This arrangement is shown in Fig. 5.2.

In the present study, tomographic images of diffusion at the systolic sweet spot were acquired with 3 x 3 x 7 mm resolution. Acquisition utilizes the twice-gated stimulated-echo pulse sequence. Diffusion-sensitizing pulsed gradients were applied in the six directions $\{x, y, z\} = \{1, \pm1, 0\}$, $\{0, 1, \pm1\}$ and $\{\pm1, 0, 1\}$ of intensity $\|\mathbf{g}_D\| = 1$ gauss cm^{-1} and duration $\delta_D = 8.6$ ms, corresponding to spatial modulation $\|\mathbf{k}_D\| = 3.7$ mm^{-1} and diffusion sensitivity $b = 4\pi^2 \Delta \|\mathbf{k}_D\|^2 \approx 400$ s mm^{-2} given a mixing time Δ = 1 R-R interval $\approx$ 800 ms. With 16 averages, TR = 5 R-R intervals $\approx$ 4 s, 75% read-out, TE = 46 ms, scan time $\approx$ 7.5 min and myocardial SNR $\approx$ 45:1 per pixel for the b = 0 and $\approx$ 25:1 for the b $\approx$ 400 s mm^{-2} images.

5.3.4 Cardiac coordinates

Cardiac coordinates are introduced for descriptive purposes by fitting a prolate ellipsoid to the epicardial contour in the multislice image data. These provide ventricular longitudinal (**L**), radial (**r**) and circumferential (**c**) coordinates [112]. Local orientations are described in relation to the unit vectors of these coordinates at each pixel: given a vector **v**, its helix angle h(**v**) is defined via the complex form

$$h(\mathbf{v}) \equiv \arg(v_c + i\, v_L) \tag{5.8}$$

where $\{v_c, v_L\}$ are its local circumferential and longitudinal components and $i = \sqrt{-1}$. Fiber helix angle is simply h(**f**).

5.4 Results

5.4.1 3D display of fiber orientation and strain tensor field

Registered images of fiber orientation **f** and systolic strain $\mathbf{S}_{sys}$ for a mid-ventricular short-axis slice rendered three-dimensionally are shown in Fig. 5.3. In the normal heart, such short-axis tomograms typically yield 200 – 300 myocardial voxels. Fiber orientation shown in Fig. 5.3, top, is represented by a cylinder at each pixel whose axis is **f** that is also color-coded according to fiber helix angle h(**f**). Fiber orientations are, as expected, approximately orthogonal to the local radial direction, and fiber helix angles show the classic transmural progression from negative subepicardially (left-handed helix, turquoise) through zero in the midwall (circumferential orientations, blue) to positive subendocardially (right-handed helix, red) [16, 70]. The registered image of myocardial net systolic strain for the identical slice is shown in Fig. 5.3, bottom. Here, ventricular myocardial strain at each location is represented by an octahedron whose axes span the points $\{\pm(1 + 2S_i)^{1/2}\ \mathbf{e}_i\}$, i = 1,2,3, where S_i and $\mathbf{e}_i$ are, respectively, the eigenvalues and eigenvectors of the systolic strain tensor $\mathbf{S}_{sys}$ at the indicated location. The orientations of principal strain are predominantly radial at each location, as expected, and the epi- to endocardial gradient of radial strains is also evident.

5.4.2 Strain component maps

Figure 5.4 shows images of systolic strain tensor $\mathbf{S}_{sys}$ components in four key representations; each panel is a 3 x 3 matrix of gray-scale images representing the 3 x 3 matrix of strain tensor components in the respective coordinates. They are representations of the myocardial systolic strain tensor $\mathbf{S}_{sys}$ in: 1) local cardiac coordinates {circumferential **c**, longitudinal **L**, radial **r**}, Fig. 5.4a; 2) principal strain coordinates $\{\mathbf{e}_1, \mathbf{e}_2, \mathbf{e}_3\}$, Fig. 5.4b; 3) fiber coordinates {fiber **f**, cross-fiber **x**, radial **r**}, $\mathbf{x} \equiv \mathbf{r} \times \mathbf{f}$, Fig. 5.4c; and 4) structural coordinates {fiber **f**, sheet **s**, sheet normal **n**}. Strain components in local cardiac coordinates (Fig. 5.4a) are, along the diagonal, radial thickening S_{rr}, and the smaller shortenings in longitudinal and circumferential directions, S_{LL} and S_{cc}. Off-diagonal entries represent shear terms and include myocardial twist S_{cL} and the transverse shears S_{cr} and S_{Lr}. The principal strain images (Fig. 5.4b) show the image of one large positive eigenvalue (S_3) corresponding in this normal heart to principal wall thickening, and two negative eigenvalues (S_1, S_2) of smaller size that are the principal shortenings. In the fiber coordinates (Fig. 5.4c), the fiber shortening map S_{ff} shows rather uniform distribution. The image of cross-fiber shortening, S_{xx}, shows a steep transmural variation which increases from the epicardium to endocardium. In the structural coordinates (Fig. 5.4d), there are significant stretching in sheet S_{ss}

and sheet normal S_{nn} directions. A large amount of shear is found in the sheet-sheet normal component, S_{sn}; the sign of the S_{sn} shows a pattern consistent with the septum-versus-free-wall polarization of the sheet angle (Fig. 5.7).

5.4.3 Uniformity of the fiber strain

Analyses of myocardial systolic normal strains, including fiber shortening, are presented in Table 5.1.

strain	strain relative to t = Ψ, (%) mean ± SD	σ^2 / μ^2 vs. S_{ff} ratio ± 95% CI	slope ± SE (% strain per unit depth)	intercept ± SE (% strain)	residual x 100%	(slope ± SE) / mean x 100%	strain relative to ED, (%) mean ± SD
S_{cc}	-15±7	1.9±0.5	-12.8±1.3	-14±4	11	88±9	-12±4
S_{LL}	-10±4	1.4±0.4	2.9±1.0	-10±3	15	-29±10	-8±3
S_{rr}	23±10	1.8±0.5	3.8±3.4	22±1	28	17±15	29±14
S_1	-21±7	0.9±0.2	- 8.7±1.3	-20±4	6	42±6	-17±3
S_2	-9±4	1.6±0.4	4.5±0.8	-9±2	12	50±9	-8±3
S_3	26±12	2.0±0.5	5.2±3.2	27±10	19	20±12	32±16
S_{ff}	**-13±4**	**1**	**2.3±1.2**	**-13±4**	**12**	**-17±10**	**-11±3**
S_{xx}	-12±7	3.7±1.0	12.2±1.4	-10±4	19	106±12	-9±5

Table 5.1. Distributions of net systolic normal strains, including fiber shortening S_{ff}.

Strains in the first column are represented relative to the cardiac configuration of the image data defined at t = Ψ, and in the last column, scaled to the end-diastolic cardiac configuration using

$$\mathbf{S}_{sys}^{ED} = \mathbf{U}_\Psi \cdot \mathbf{S}_{sys} \cdot \mathbf{U}_\Psi \qquad (5.9)$$

where $\mathbf{U}_\Psi$ is the stretch from t = t_0 to t = Ψ in the coordinates at t = Ψ

$$\mathbf{U}_\Psi = (\mathbf{1} - 2\, F_0(\Psi)\, \mathbf{S}_{sys})^{-1/2} ,$$

where $F_0(\Psi)$ represents the fraction of total systolic strain that has taken place between end-diastole and the sweet spot. See Appendix A3 for the derivation of Eq. 5.9.

The mean net systolic fiber shortening relative to fiber length at mid-systole (t = Ψ) is S_{ff} = 13 ± 4%, and relative to fiber length at end-diastole is S_{ff}^{ED} = 11 ± 3%. Distribution widths are measured by the variance of each strain component and by the slope of its linear regression versus wall depth, both scaled to the means. Fiber shortening has the narrowest distribution of the measured normal strains after principal thickening S_1. Fiber shortening has the lowest transmural

regression slope relative to its mean: nominally similar to radial thickening S_{rr}, fiber shortening has a significantly better fit to the linear model, indicated by smaller normalized residual ($\sum$(strain - fit)^2 / $\sum$ strain^2). The regression plots are shown in Fig. 5.5.

5.4.4 Orientations of fibers relative to the principal shortenings

The comparatively large values of cross-fiber shortening are evident in the image of S_{xx} and its steep regression slope from epi- to endocardium. To further characterize the role of cross-fiber shortening, the deviation angles between fiber orientation and the directions of maximum and of minimum shortening (S_1 and S_2, respectively) were measured as functions of wall depth. The direction of maximum shortening coincides with fiber orientation subepicardially and with increasing wall depth rotates away from the fiber direction and becomes orthogonal to fiber orientation endocardially, Fig. 5.6. This transmural variation of the deviation is characteristic of all the ventricular myocardium except near the papillary muscle insertions (Fig. 5.6, top). The change in orientation with wall-depth is linear, having a regression r = 0.9 (Fig. 5.6, bottom).

5.4.5 Orientations of sheets relative to the principal thickenings

To understand the structural basis for large sheet-sheet normal shear, we computed the angle between sheet orientation and the direction of the principal thickening. The spatial map of this angle shows a clear separation of the sheet angle sign between septum and the free wall; the positive angles are predominantly distributed in the septum whereas the negative angles are in the free wall (Fig. 5.7, top). Histogram of this angle shows a bimodal distribution (Fig. 5.7, bottom). A larger bump, corresponding to the sheet population in the free wall, has a peak at -45°. In the septum, which comprises one third of the sheet population, the peak of the sheet angles to the direction of the principal thickening is 63°.

5.5 DISCUSSION

MRI of myocardial diffusion and strain noninvasively provides quantitative images of myocardial architecture and function. In consequence, these studies are for the first time feasible in humans and avoid key methodological difficulties of prior analyses of myocardial structure and function, principally the difficulty of obtaining metrically correct structural information *ex vivo* that is accurately registered with myocardial function measured *in vivo*.

5.5.1 Fiber shortening

The hypothesis that myocardial fiber shortening is transmurally uniform was proposed by Arts [24], and was subsequently derived as an optimal solution to a general model of myocardial fiber architecture and function [106]. This hypothesis has been supported by experimental observations in the canine. Waldman who found fiber shortenings in the inner and outer half-walls of 6 ± 6 and $9 \pm 4\%$, using radio-opaque marker strain measurement and post-mortem histology for fiber architecture [21]. Rademakers correlated strain measured with tagging MRI and *ex-vivo* histology, and found the fiber shortening in the inner and outer half halves of the ventricular to be $8.5 \pm 10\%$ and 6.4 ± 11.8 [22]. Blumgarden, using tagging MRI and published values of helix angles, found shortening in the inner and outer halves of the ventricular wall of 12% and 13%, respectively [28]. The present MRI studies show fiber shortening to be among the most uniform of normal strain, and yields an estimate of mean systolic fiber shortening (with respect to end-diastole) of $11 \pm 3\%$. It also resolves a small but significant systematic decrease of fiber shortening from epicardium to endocardium, 12 ± 1 to $10 \pm 1\%$ respectively, confirming a small retrograde gradient of fiber shortening.

The finding that the deviation angle between principal shortening and fiber orientation increases from epi- to endocardium was made by Prinzen and Arts [113], who suggested that the deviation angle serves to equalize fiber shortening transmurally, and estimated the angle to range from 10° to 90° from epi- to endocardium based on published fiber orientations. This was confirmed by Waldman who found respective deviation angles of 25° and 91°, in the outer and inner halves of the canine ventricular wall [21]. Present MRI data in the human show smooth rotations of fiber orientation relative to both principal shortenings (S_1 and S_2) that is quite linear with wall depth ($r = 0.9$) over a complete 90° of rotation, Fig. 5.6.

An interesting aspect of the present data is the observation that the helix angles of the fibers sweep through approximately 180° transmurally, while disparity angles between fiber and principal shortening sweep through approximately 90°. The key point is that these ranges, of 90° and 180°, represent the extreme ranges of meaningful values of the variables in question. In light of this extremality, it is reasonable to posit that these variables are closely optimized by direct or indirect physiologic control mechanisms [25].

5.5.2 Unity of trabecular and compact myocardial function

Present data shed light on interesting differences between MRI of myocardial architecture and prior histological analyses. We have previously reported finding endocardial fiber helix angles in the human with values ranging up to 110° and do so again in the present *in vivo* data [98]. This result differs from most published results based on conventional histological analyses which reported

fiber angles only to 50° – 70° [16]. Present data suggest a possible explanation: that MRI appears to detect and accurately map the myocardial structure and function of the trabecular myocardium that may be poorly represented in previous histologic studies. Trabecular tissue is well represented by MRI; it is uncontaminated by partial-volume averaging with intra-cavitary blood, as this blood contributes little or no signal to present diffusion and strain images due to its high relative velocities. Direct evidence that the endocardial zone showing high fiber angles is indeed trabecular is provided by the strain images. On close inspection, the endocardial free-wall shows a systolic radial *thinning* (systolic radial strains < 0) indicating a radial compression. Further, the trace of the strain tensor, trace(**S**), is also exceptional in this same subendocardial region. While trace(**S**) ≈ 0 throughout most of the myocardium, consistent with its incompressibility, the subendocardial lateral wall has trace(**S**) < 0, indicating volumetric compression like a sponge. In contrast, at the level of fiber architecture and fiber shortening, this trabecular zone has no distinguishing features, but appears entirely integral with the adjacent compact myocardium.

5.5.3 Significance of sheet orientations

Present study characterizes an important principle of the sheet function: sheets tend to be oriented to maximize sheet slippage, that is, they tend to be oriented at 45° to the direction of the principal thickening. This finding confirms LeGrice's hypothesis of mechanism for ventricular wall thickening [31]. He asserted that slippage between the sheets is the underlying structural action for cellular rearrangement to occur; this cellular rearrangement has long been known to support the wall thickening. If the function of sheets is attributed to their shearing motion, we further postulate that the orientations of these sheets should be optimized to the best advantage, i.e., 45° to the direction of the principal thickening. Out results show that, in the free wall, it is indeed true (45° in both mean and peak). In the septum, however, there is a deviation of approximately 20° from this optimal angle. The deviation implies that the functional development of the septum is somewhat different from the free wall.

5.5.4 Error analysis

Known sources of error arising from the present imaging process yield an accuracy estimate for the fiber shortening images of 15 – 20% per pixel. This estimate includes: 1) effects of the statistical noise in images of diffusion and strain images (10% and 5%, respectively); 2) error in sweet spot location, which we estimate to correspond to ≤ 10% of the systolic strain and which perturbs the diffusion data according proportional to strain; and 3) error arising from the error in the assumption that the interaction of cardiac diffusion and strain is approximately linear. The cardiac diffusion-strain linearity assumption requires that there exists a linear function, $\boldsymbol{L}(\mathbf{D}_0, \mathbf{S})$, such that

strain modifies observed diffusion $\mathbf{D}_{obs}$ according to

$$\mathbf{D}^{obs} \approx \mathbf{D}_0 + \boldsymbol{L}(\mathbf{D}_0, \mathbf{S}) \tag{5.10}$$

where $\mathbf{D}^{obs}$ is the observed diffusion and $\mathbf{D}_0$ is the diffusivity were there no motion. The model of Reese et al., states that in the present experiment, the observed diffusion is

$$\mathbf{D}_\tau^{obs} = \langle \mathbf{U}_\tau^{-1}(t) \cdot \mathbf{D}_0 \cdot \mathbf{U}_\tau^{-1}(t) \rangle_\Delta \tag{5.11}$$

where $\mathbf{U}_\tau(t)$ is the history of material stretch relative to the configuration at time 'τ', and $\mathbf{U} = (\mathbf{1} + 2\mathbf{S})^{1/2}$. Eq. 5. 10 implies a small nonlinearity in the strain-diffusion interaction, that in scalar form leads to an error

$$\begin{aligned} (D_\Psi^{obs} - D_0)/D_0 &= \langle U_\Psi^{-2} \rangle_\Delta \\ &= \langle 4S_\Psi^2 (1 + 2S_\Psi)^{-1} \rangle_\Delta \leq 10\% \end{aligned} \tag{5.12}$$

where motion periodicity has given $\langle S_\Psi \rangle_\Delta = 0$ and $\langle 4S_\Psi^2 (1 + 2S_\Psi)^{-1} \rangle_\Delta \leq 10\%$ is a numerical estimate based on realistic cardiac strain histories (F(t); see Fig. 5.1). These strain histories are scaled to a maximum strain $|S_\Psi^{max}| \leq 10\%$, appropriate for the shortening strains that can affect fiber orientation, and incorporating typical errors related to the approximation of Eq. 5.3 [95]. The net error is estimated as the root-mean-square of these separate terms treated as uncorrelated. The relation of this scalar estimate to the tensor case is not well understood, the difficulty being that errors in the tensor case can depend upon the unknown correlation between diffusion and strain whose measurement is a principal experimental objective.

5.5.5 Future work

A few points relating on the implementation of the MRI methodology in humans deserve comment. First, volunteers have performed the synchronized breathing after a 1 to 2 min rehearsal in the scanner without difficulty. Images with incorrect gated may be identified post hoc and discarded: the cardiac diffusion images tested for motion effects by evidence of phase errors, and the strain images tested for motion by evidence of misregistration. In practice, however, this procedure proved unnecessary in our population of volunteers. In the future, we expect to replace synchronized breathing with one of the automated MRI methods for respiratory synchronization now under development, and by eliminating respiratory delays, to reduce acquisition times by a factor of at least two. Extension of the present methodology to cardiac diseased will require consideration of effects of possible cardiac dyssynergy on the diffusion and strain measurements. We anticipate negotiating a time-efficient compromise between the present methods specialized to the synergic heart and the method of Reese et al. that is generally applicable, in which somewhat

more data than used here are acquired to measure particular parameters of interest, for example, fiber shortening.

5.6 CONCLUSION

Registered NMR images of myocardial diffusion and strain provide the experimental basis for quantitative analysis of myocardial architecture and function. Focusing on contraction, present MRI measurements of the dynamics of human myocardial fiber shortening are in good accord with previous findings in canines. It also characterizes the role of the sheets in contribution to the wall thickening. Because these data are spatially resolved images, providing hundreds of ventricular pixels, they offer finer and more complete pictures of myocardial fiber architecture and its dynamics than previously available. Additionally, because they are noninvasive, such analyses may now be accomplished in their entirety in living subjects. These capabilities should afford a significantly more flexible approach to the study of myocardial architecture and function in the normal heart and in disease.

Appendix A.3 Conversion of reference state of strain from mid-systole to end-diastole

Consider a material point $\mathbf{x}$ in the mid-systolic configuration, this point $\mathbf{x}$ is mapped to $\mathbf{y}_1$ in the end-diastolic and $\mathbf{y}_2$ in the end-systolic configuration by local deformation gradient tensors $\mathbf{F}_1$ and $\mathbf{F}_2$, respectively (see the figure below), with linear relationships $\mathbf{y}_1 = \mathbf{F}_1 \cdot \mathbf{x}$, and $\mathbf{y}_2 = \mathbf{F}_2 \cdot \mathbf{x}$. Then the strains to end-diastole ($\mathbf{S}_1$) and to end-systole ($\mathbf{S}_2$) with respect to mid-systole can be described as

$$\mathbf{S}_i = (\mathbf{F}_i^T \cdot \mathbf{F}_i - \mathbf{1}) / 2, \text{ for } \quad i = 1,2 \ . \tag{A.8}$$

We define the net systolic strain with respect to mid-systole $\mathbf{S}_{ms}$ to be the sum of $-\mathbf{S}_1$ and $\mathbf{S}_2$:

$$\mathbf{S}_{md} = (-\mathbf{F}_1^T \cdot \mathbf{F}_1 + \mathbf{1}) / 2 + (\mathbf{F}_2^T \cdot \mathbf{F}_2 - \mathbf{1}) / 2 = (\mathbf{U}_2^2 - \mathbf{U}_1^2) / 2 \ . \tag{A.9}$$

Knowing that $\mathbf{y}_2 = \mathbf{F}_2 \cdot \mathbf{x} = \mathbf{F}_2 \cdot \mathbf{F}_1^{-1} \cdot \mathbf{y}_1$, the net systolic strain with respect to the end-diastole $\mathbf{S}_{ed}$ can be expressed as

$$\mathbf{S}_{ed} = ((\mathbf{F}_2 \cdot \mathbf{F}_1^{-1})^T (\mathbf{F}_2 \cdot \mathbf{F}_1^{-1}) - \mathbf{1}) / 2 = (\mathbf{F}_1^{-T} \cdot \mathbf{U}_2^2 \cdot \mathbf{F}_1^{-1} - \mathbf{1}) / 2 \ . \tag{A.10}$$

Using $\mathbf{U}_2^2 = 2\,\mathbf{S}_{md} + \mathbf{F}_1^T \cdot \mathbf{F}_1$ obtained from Eq. A.9 and replacing $\mathbf{U}_2^2$ in Eq. A.10, we have

$$\begin{aligned} \mathbf{S}_{ed} &= (\mathbf{F}_1^{-T} \cdot (2\,\mathbf{S}_{ms} + \mathbf{F}_1^T \cdot \mathbf{F}_1) \cdot \mathbf{F}_1^{-1} - \mathbf{1}) / 2 \\ &= \mathbf{F}_1^{-T} \cdot \mathbf{S}_{ms} \cdot \mathbf{F}_1^{-1} = \mathbf{U}_1^{-1} \cdot \mathbf{S}_{ms} \cdot \mathbf{U}_1^{-1} \ . \end{aligned} \tag{A.11}$$

The last equality has used the fact that there is negligible rigid body rotation during contraction.

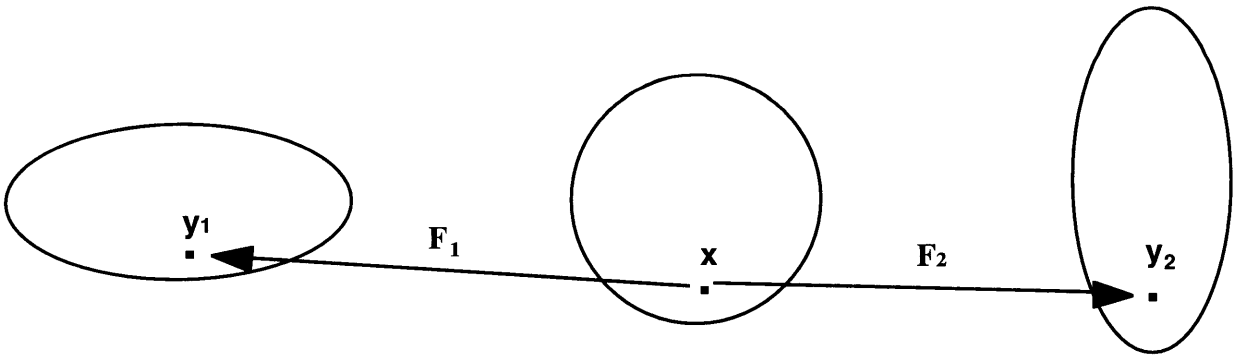

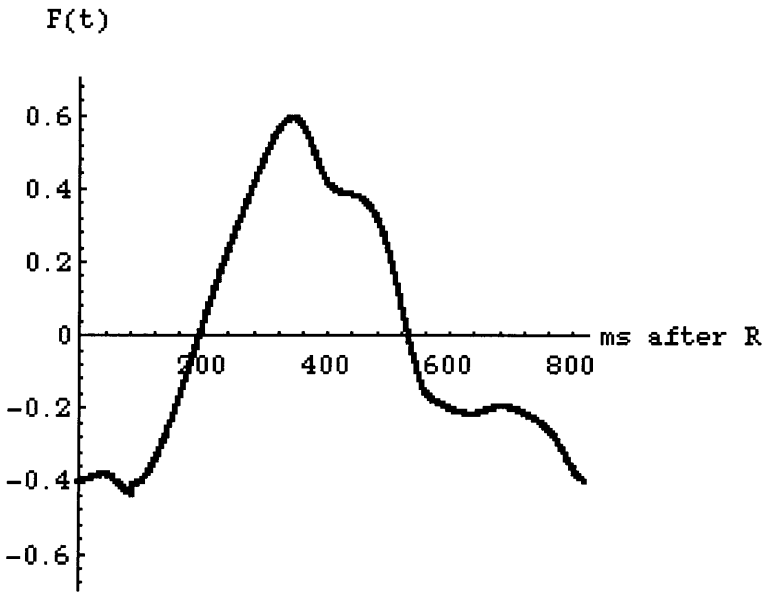

Figure 5.1 Time course function F(t) of the mean radial strain relative to the sweet spots (the points where curve passes zero). The time integral of F(t) over one cardiac cycle equals zero. Therefore, the effect of strain on the diffusion measurement vanishes up to the first order.

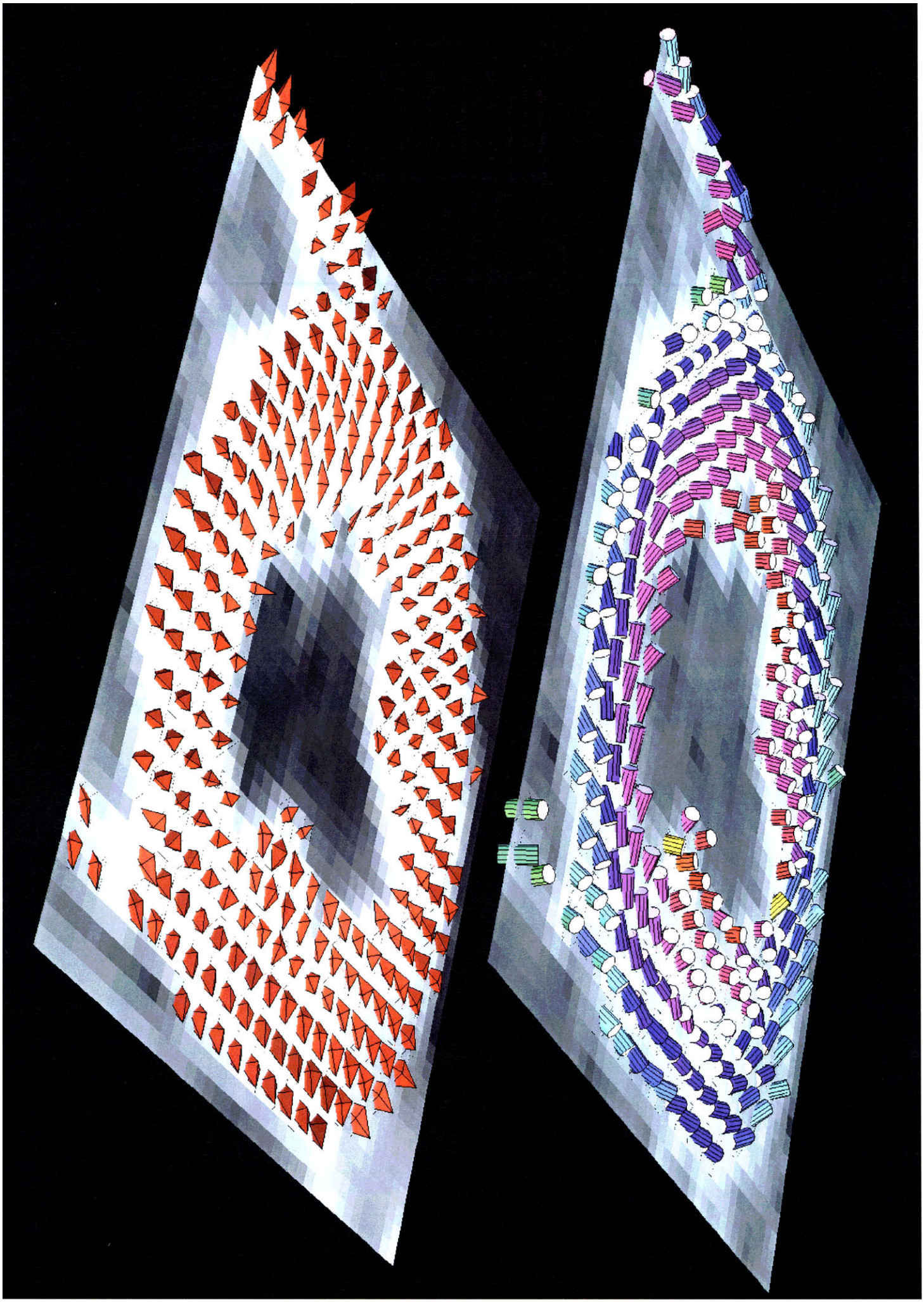

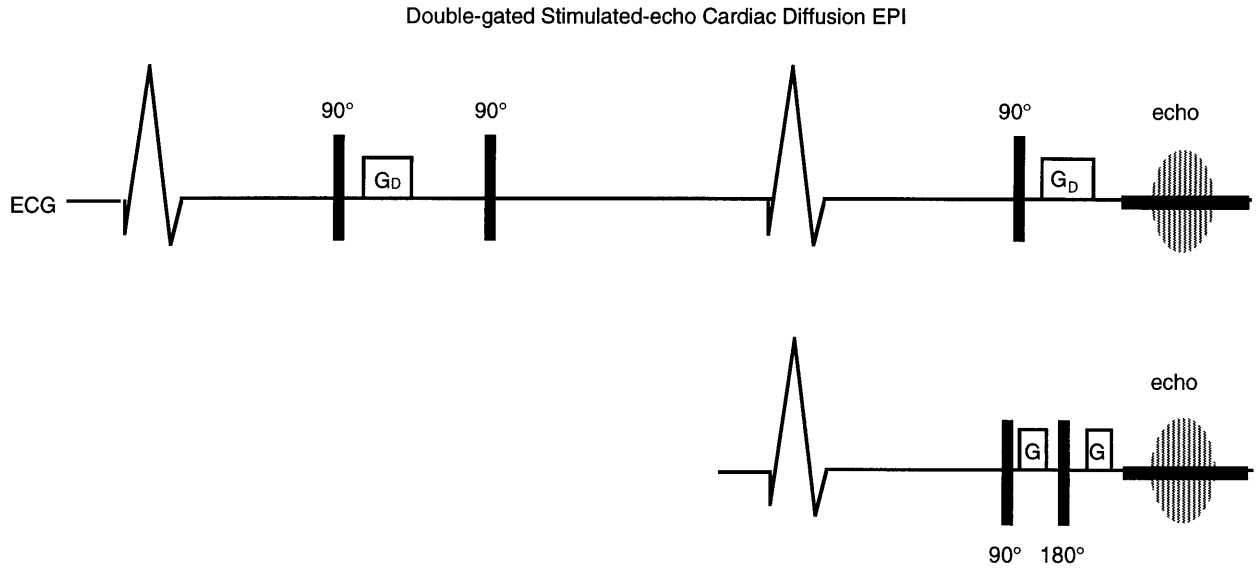

Figure 5.2 Registered diffusion and strain MRI pulse sequences. In STE-EPI sequence (upper), diffusion-sensitizing gradients (G_D) are positioned at the same cardiac phase of the consecutive heart beats. The phase-contrast spin-echo sequence is registered to STE-EPI sequence with alignment of slice-select, gradient-encoding (G), and signal read-out.

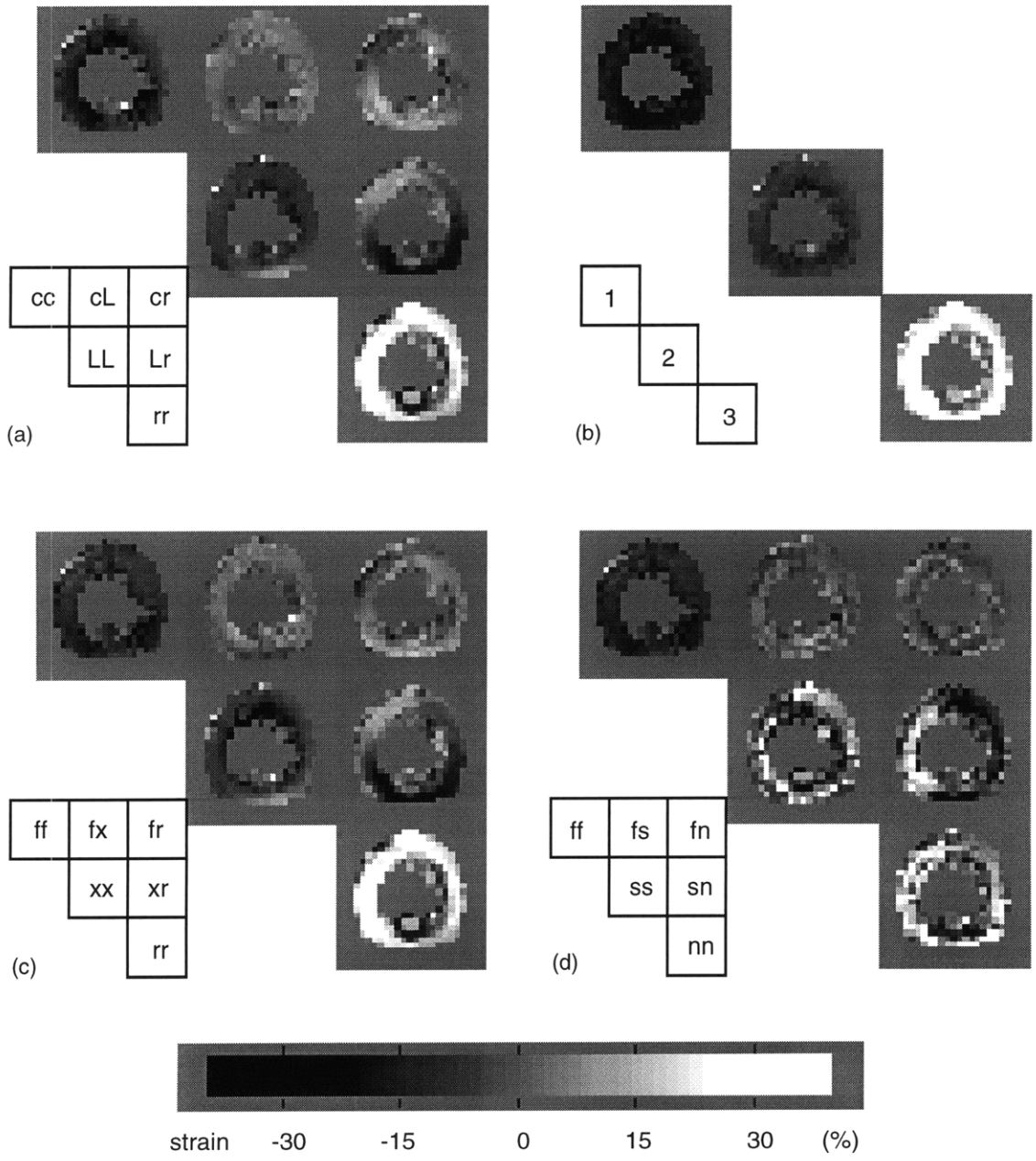

Figure 5.4 Strain component maps in local cardiac (a), principal (b), fiber (c), and structural (d) coordinates.

Figure 5.3 (see the left page) Graphics display of 3D orientations of the myocardial fibers (top) and the registered strain tensor field (bottom) from a normal volunteer.

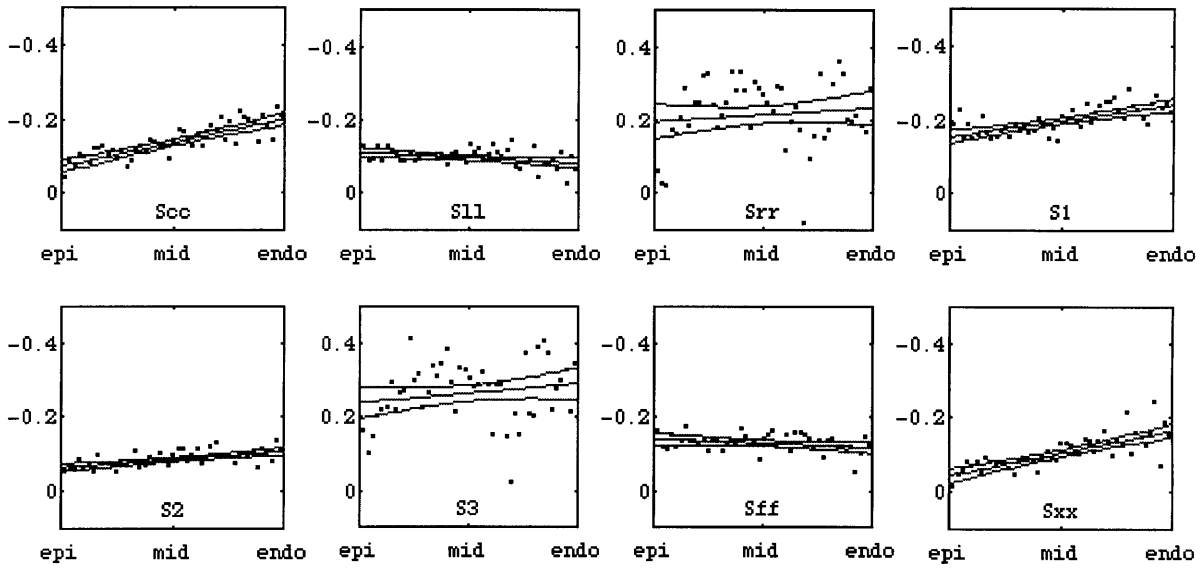

Figure 5.5 Linear regressions, with 95% confidence intervals, of normal strains versus wall depth.

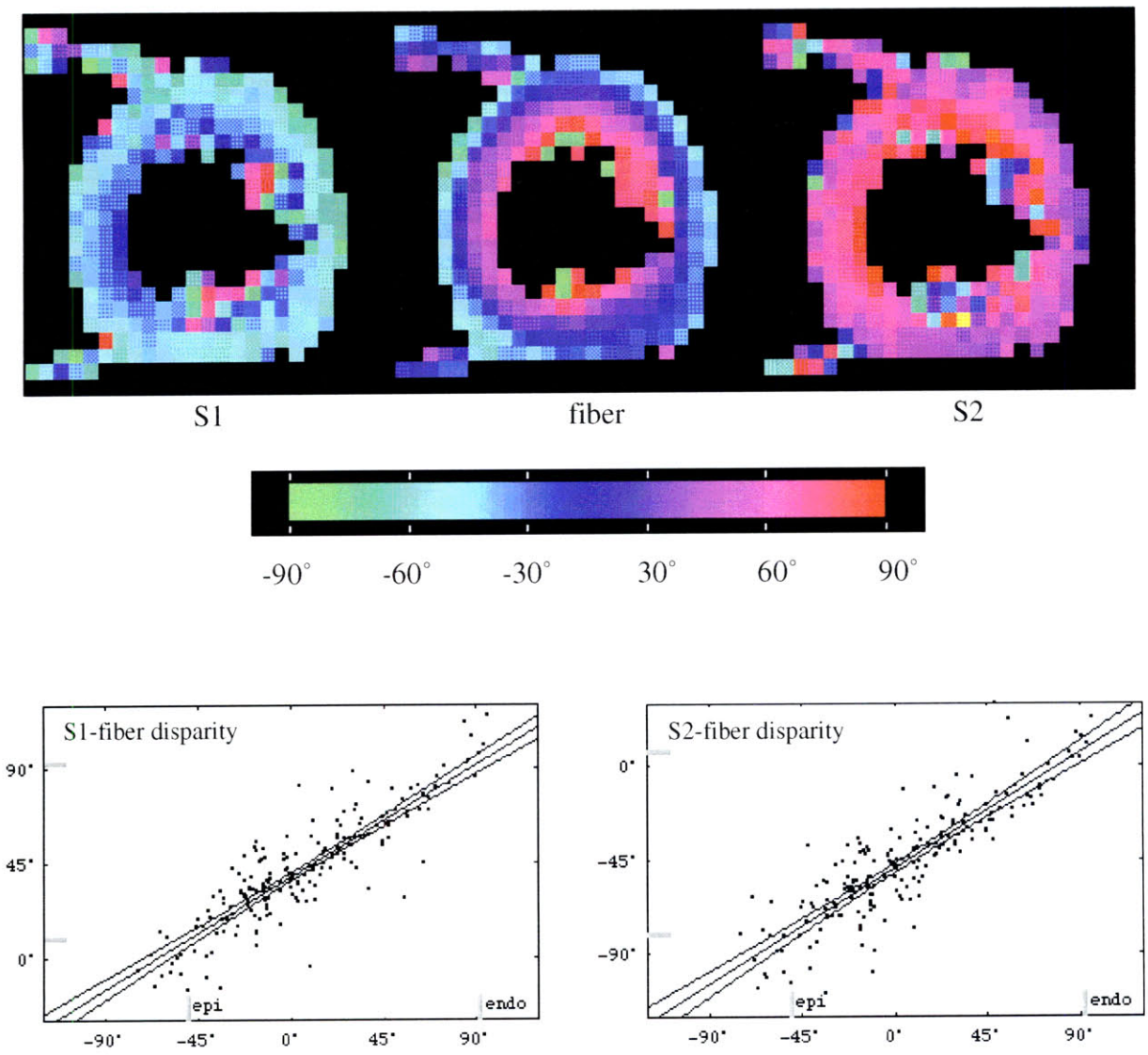

Figure 5.6 Images of helix angles of maximal principal shortening (S_1), fiber and minimal principal shortening (S_2), top, and linear regression of disparity angles versus radial depth, bottom.

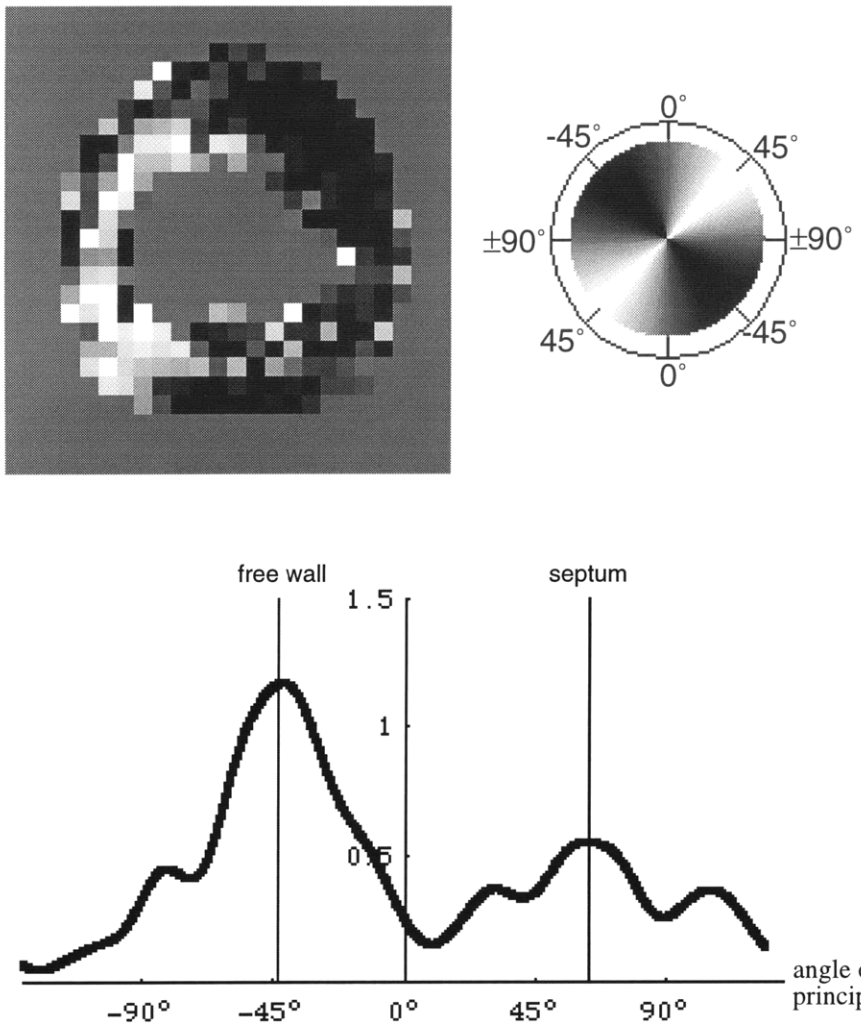

Figure 5.7 The quantitative map of the sheet angles relative to the direction of principal thickenings (top), and the corresponding histogram (bottom).

Chapter 6

Conclusions

6.1 Summary

The main goal of this thesis is to demonstrate the capacity of registered diffusion and strain MRI to noninvasively define structure-function relations in the human heart. In achieving this goal, three key questions are addressed in the present work. First, can the diffusion anisotropy of the myocardium faithfully depict the orientation of the underlying fiber and sheet structures (Chapters 2 and 3)? Second, how can we circumvent the complex effect of strain on the diffusion when it is measured in the beating heart (Chapter 4)? Third, can registered diffusion and strain MRI in the human heart reproduce main features of structure-function relations found in animal models (Chapter 5)? In the following paragraphs, we will summarize our results in answering these questions.

To answer the first question, in Chapter 2, we begin our investigation on the correspondence of the 1-2 eigenspace of the diffusion tensor with the sheet structure in 5 mm-thick sections of the cow hearts (Section 2.1). Intersections of 1-2 eigenspaces with the imaging plane were compared with the registered optical image of cleavages shown on the same plane. The histograms of deviation angles consistently show a skew Gaussian with a peak at about 10°. This histogram can be explained by a model of MR-defined sheet orientation as it deviated from the north pole (real sheet orientation) according to a Gaussian distribution of a 10° width. These results suggest that the deviation between 1-2 eigenspaces of the diffusion tensors and the sheet orientations is within the limit of MR noise.

Next, in Section 2.2 we investigate the correspondence of the principal diffusion with the fiber orientation in a normal cadaver heart. Helix and imbrication angles of the first eigenvectors of the diffusion tensors are quantified in local cardiac coordinates. From comparison of the features

of these angular distributions with those found in quantitative histology, MR diffusion tensor imaging reveals consistent classic patterns of fiber organizations. In Section 2.3 we also quantify the sheet orientation in the same normal cadaver heart. We show that sheet organization presents a unique septum-versus-free-wall bimodal distribution. This pattern is in accord with the recently published histologic findings on the sheet architecture. Angular error of MR diffusion measurement is estimated to be approximately 10° and 15° for fiber and sheet orientations, respectively.

To successfully describe the myocardial architecture, MRI not only should present a clear and histologically-consistent picture in the normal heart, it also should be able to differentiate diseased hearts from normal hearts by showing the changes in their architectural patterns. For this reason, the ability of MR diffusion tensor imaging is further tested in Chapter 3 by measuring architectural abnormalities in the diseased cadaver hearts, including hypertrophic cardiomyopathy and infarct expansion. As compared to normal distribution patterns, helix, sheet and imbrication angles of these two diseased hearts show several significant changes. Hypertrophic cardiomyopathy shows a substantial decrease in diffusion anisotropy; as compared to the normal heart, the variance ratio (±95% C.I.) of mean-normalized eigenvalues was 4.5 ± 0.2. It also shows an increase in circumferential fiber proportion (0.51 versus 0.44 in the normal), and a widening of the imbrication angle distribution (variance ratio to normal = 1.9 ± 0.1). In the infarct expansion, there is depletion in circumferential fiber proportion (0.36 versus 0.44 in the normal), and decrease in proportion of small sheet angles (0.26 versus 0.41 in the normal). These changes are in general consistent with the observed architectural changes reported in the literature. Based on the results of Chapter 2 and Chapter 3, we conclude that MR diffusion tensor imaging is a reliable tool to depict myocardial architecture.

To address the second question, in Chapter 4 we develop an efficient method to obtain reliable diffusion data *in vivo*. Owing to the synchrony of the normal cardiac cycle, we show in the theory that there are points in the cardiac cycle, "sweet spots," when the net effect of strain on diffusion encoding is near zero. These are points in mid-systole and mid-diastole when the cardiac configuration approximates its mean. After defining a practical strategy to compute the sweet spot locations, we test cardiac diffusion MRI experimentally in normal human subjects in two ways. We find that the trace ADC at the sweet spot is equal to the mean trace ADC over one cardiac cycle as predicted by the theory, and that myocardial fiber architecture depicted at the sweet spot is in good agreement with that obtained in the *ex-vivo* heart. Myocardial diffusion MRI in the beating human heart shows a normal transmural variation of fiber helix angles, with a helix angle histogram characterized by dominant circumferential population. Imbrication and sheet angle maps also reproduce the main features found in the *ex-vivo* heart. Our error estimate shows approximately 90% accuracy attainable by this sweet spot method. The success of this method

greatly reduces the cost for strain correction and enhances the feasibility of MR diffusion measurement in the beating heart.

For the third question, in Chapter 5 we implement registered diffusion and strain MRI to normal volunteers and obtain quantitative maps of motion patterns of the fibers and the sheets. From these quantitative maps, many principal findings concerning structure-function relations of the myocardium are in good agreement with those obtained invasively from animal models. These consistent findings include the followings: 1) net systolic fiber shortening relative to end-diastole is measured to be $11 \pm 3\%$; 2) fiber shortening is found to have the highest transmural uniformity of measured normal strains; 3) the angle of disparity between fiber orientation and the direction of principal shortening is found to increase from 0° to 90° from epi- to endocardium; 4) a steep transmural slope from $3 \pm 2\%$ to $18 \pm 3\%$ from epi- to endocardium is observed in cross-fiber shortening. Since these quantitative maps are spatially resolved (3 x 3 in-plane resolution) and comprehensive (over the whole mid-LV), the features of these structure-function relations can be fully appreciated by a more rigorous analysis. For example, in investigating relative uniformity of fiber shortening, we compare normalized variance ratios, transmural slopes, and the residues against the slope among all normal strains. In this analysis, fiber shortening is found to have all the attributes that would qualify it to be the most uniform of all strains. In the study of disparity angle of the fiber to the direction of principal shortening, we further analyze the behavior of this angle versus wall depth. The result is astonishing. It shows an essentially linear variation of this angle across the wall, evidenced by a high correlation coefficient $r = 0.9$ over more than 200 data points. These solid examples demonstrate the ability of registered diffusion and strain MRI to reproduce published findings of structure-function relations with a superior quality.

Furthermore, registered diffusion and strain MRI also produces new results that we believe are important in understanding the LV functional design. They are: 1) first spatial mapping of strain components in geometrically based as well as structurally based coordinate systems; 2) first illustration of the structural and functional unity of the trabecular and compact myocardium; 3) first direct demonstration of myocardial sheet function, and of the optimal orientation of the sheets for maximum shear relative to *in-vivo* strains.

6.2 Conclusion

In this thesis, we have shown the capability of registered diffusion and strain MRI to provide reliable, quantitative maps of myocardial structure-function relations in the living human. From these quantitative maps, we are able to deduce simplifying principles concerning the design

purpose of the fiber and sheet organization. The success of this method has four potential implications. First, it overcomes the difficult access to the myocardial architecture, making structural information available from the intact heart. This will facilitate clarification of the complex organization of the myocardium. Second, it adds value to the conventional strain MRI. The myocardial strain can now be described in the structurally based coordinate system; as compared to the conventional geometrically based coordinate system, they provide more insights into the function of the underlying structural elements. Third, it produces comprehensive data of local myocardial architecture and myocardial strain over the whole LV, and have revealed simplifying principles governing structure-function relations. This knowledge will be of great value for improving the model of the LV wall mechanics. Fourth, it expands the scope of the experimental study of myocardial structure-function relations. Using this method, investigation of structure-function relations in the diseased hearts can be carried out. Moreover, because it is noninvasive, adaptive process of the myocardium can be observed by longitudinal study on the same subject.

6.3 Future work

The present work has established a framework of knowledge concerning myocardial architecture and its role in the LV pump function. Based on this, we will continue to address the following specific questions. First, a longitudinal study on the effect of architectural derangement to the ventricular remodeling in the patients of myocardial infarction will be carried out. Our results of the cadaver heart (Chapter 3) imply that depletion in circumferential fibers and diastolic slippage of the sheets may have significant impact on infarct expansion. Second, we will try to quantify cellular rearrangement as an indicator for sheet function. Our preliminary study shows that this rearrangement activity can be probed by a time series of myocardial diffusion and strain MRI. Third, we will model the relationship between diffusion and strain. In highly organized tissue, restricted diffusion is expected to be affected by the deformation applied to the tissue. In the present study, we assume this effect is linear, so it can be neglected at the sweet spot (Chapter 4). Clarification of this effect is necessary to improve our strain correction scheme. Finally, the discovery of sheet architecture in the myocardium induces many intriguing questions. What is the global picture of the cleavage plane hierarchy? How do these cleavage planes affect the mechanical property of the myocardium? How do these cleavage planes form? Why is there septum-versus-free-wall separation? What controls the extent and density of the cleavage planes? These puzzles remain to be solved.

Bibliography

1. Stensen N: De musculis et glandulis observationum specimen, cum epistolis duabus anatomicis. Amsterdam: P le Grand, 1664.
2. Lower R: Tractus de Corde, 1932 ed. London: Oxford University Press, 1669.
3. Senac JBD: Traite de la Structure du Coeur, de son Action, et de ses Maladies., Vol. 1. Paris: J Vincent, 1749.
4. Ludwig C: Ueber den Bau und die Bewegungen der Herzventrikel. Zeitschrift fur rationelle Medicin 1849; 7: 189-220.
5. Pettigrew JB: On the arrangement of the muscular fibres in the ventricles of the vertebrate heart, with physiological remarks. Philosophical Transactions 1864; 154: 445-500.
6. Krehl L: Kenntniss der Fullung und Entleerung des Herzens. Abhandl. Math. Phys. Kl. Koniglichen Saechs. Ges. Wiss. 1891; 29: 341-362.
7. MacCallum JB: On the muscular architecture and growth of the ventricles of the heart. Johns Hopkins Hospital Reports 1900; 9: 307-335.
8. Mall FP: On the muscular architecture of the ventricles of the human heart. Am J Anat 1911; 11: 211-266.
9. Lev M, Simkins CS: Architecture of the human ventricular myocardium, technique for study using a modification of the Mall-MacCallum method. Laboratory Investigation 1956; 5: 396-409.
10. Grant RP: Notes on the muscular architecture of the left ventricle. Circulation 1965; 32: 301-308.
11. Torrent-Guasp F: The cardiac muscle. Madrid: Fundacion Juan March, 1973.
12. Hort W: Untersuchungen uber die Muskelfaserdehnung wand des Meerschweinchens. Virchow Arch. Pathol. Anat. Physiol. Klin. Med. 1957; 329: 694-731.
13. Streeter DD, JR.,, Bassett DL: An engineering analysis of myocardial fiber orientation in pig's left ventricle in systole. Anat. Rec. 1966; 155: 503-511.
14. Streeter DD, Spotnitz HM, Patel DP, Ross J, Sonnenblick EH: Fiber orientation in the canine left ventricle during systole and diastole. Circulation Research 1969; 24: 339-347.
15. Streeter DD, Vaishnav RN, Patel DJ, Spotnitz HM, Ross J, Sonnenblick EH: Stress distribution in the canine left ventricle during diastole and systole. Biophysical Journal 1970; 19: 345-363.
16. Streeter DD: Gross morphology and fiber geometry of the heart. In: Berne RM, ed. Handbook of Physiology, vol 1: The Heart. Section 2: The Cardiovascular System. Bethesda, MD: American Physiological Society, 1979; 61-112.
17. Streeter DD, Ramon C: Muscle pathway geometry in the heart wall. Journal of Biomechanical Engineering 1983; 105: 367-373.

18. Hort W: Makroskopische und mikrometrische untersuchungen am myokard verscheiden stark gefulter linker kammern. Virchows Arch. Path. Anat. Physiol. Klin. Med. 1960; 333: 523-564.
19. Caufield JB, Borg TK: The collagen network of the heart. Laboratory Investigation 1979; 40: 364-372.
20. LeGrice IJ, Smaill BH, Chai LZ, Edgar SG, Gavin JB, Hunter PJ: Laminar structure of the heart I: Ventricular myocyte arrangement and connective tissue architecture in the dog. American Journal of Physiology 1995; 269: H571-H582.
21. Waldman LK, Nosan D, Villarreal F, Covell JK: Relation between transmural deformation and local fiber direction in canine left ventricle. Circulation Research 1988; 63: 550-562.
22. Rademakers FE, Rogers WJ, Guier WH, et al.: Relation of regional cross-fiber shortening to wall thickening in the intact heart: three-dimensional strain analysis by NMR tagging. Circulation 1994; 89: 1174-1182.
23. MacGowan GA, Shapiro EP, Azhari H, et al.: Noninvasive measurement of shortening in the fiber and cross-fiber directions in the normal human left ventricle and in idiopathic dilated cardiomyopathy. Circulation 1997; 96: 535-541.
24. Arts T, Reneman RS, Veenstra PC: A model of the mechanics of the left ventricle. Annals of Biomedical Engineering 1979; 7: 299-318.
25. Arts T, Prinzen FW, Snoeckx LHEH, Rijcken JM, Reneman RS: Adaptation of cardiac structure by mechanical feedback in the environment of the cell: a model study. Biophysical Journal 1994; 66: 953-961.
26. Feigl EO: Coronary physiology. Physiological Review 1983; 63: 1-206.
27. Prinzen FW: Gradients in fiber shortening and metabolism across the ischemic left ventricular wall. American Journal of Physiology 1986; 250: H255-264.
28. Bloomgarden DC, Young AA, Kraitchman DL, et al.: Noninvasive assessment of regional myocardial fiber and cross-fiber strain using finite element modeling and magnetic resonance tagging. International Society for Magnetic Resonance in Medicine, 5th scientific meeting and exhibition, Vancouver, B.C., Canada, 1997.
29. Sonnenblick EH, Ross JJ, Covell JW, Spotnitz HM, Spiro D: The ultrastructure of the heart in systole and diastole. Circulation Research 1967; 21: 423-431.
30. Spotnitz HM, Spotnitz WD, Cottrell TS, Spiro D, Sonnenblick EH: Cellular basis of volume related wall thickness changes in the rat left ventricle. J Molec Cell Cardiol 1973; 6: 317-331.
31. LeGrice IJ, Takayama Y, Covell JW: Transverse shear along myocardial cleavage planes provides a mechanism for normal systolic wall thickening. Circ Res 1995; in revision.
32. Weisman HF, Bush DE, Mannisi JA, Weisfeldt ML, Healy B: Cellular mechanisms of myocardial infarct expansion. Circulation 1988; 78: 186-201.
33. Olivetti G, Capasso JM, Sonnenblick EH, Anversa P: Side-to-side slippage of myocytes participates in ventricular wall remodeling acutely after myocardial infarction in rats. Circulation research 1990; 67: 23-34.
34. Sonnenblick EH: Physical forces and myocyte cell death. American Heart Association 70th Scientific Sessions, Orlando, Florida, U.S.A., 1997.

35. Bloch F: Physical Review 1946; 70: 460.
36. Purcell E, Torrey H, Pound R: Physical Review 1946; 69: 37.
37. Suryan G: Proc. Indian Acad. Sci., Vol. A 33, 1951.
38. Singer JR: Blood flow rates by nuclear magnetic measurements. Science 1959; 130: 1652-1653.
39. Morse OC, Singer JR: Blood velocity measurements in intact subjects. Science 1970; 170: 440-441.
40. Zerhouni EA, Parish DM, Rogers WJ, Yang A, Shapiro E: Human Heart: tagging with MR imaging - a method for noninvasive assessment of myocardial motion. Radiology 1988; 169: 59-63.
41. Young AA, Axel L: Three-dimensional motion and deformation of the heart wall: estimation with spatial modulation of magnetization - a model based approach. Radiology 1992; 185: 241-247.
42. Azhari H, Weiss JL, Rogers WJ, Siu C, Zerhouni EA, Shapiro EP: Non-invasive quantification of principal strains in normal canine hearts using tagged MRI images in 3D. American Journal of Physiology 1993; 264: H205-H216.
43. Axel L: Noninvasive measurement of cardiac strain with MRI. Adv Exp Med Biol 1997; 430: 249-256.
44. Carr H, Purcell EM: Effects of diffusion on free precession in NMR experiments. Physical Review 1954; 94: 630-638.
45. Hahn EL: Detection of sea-water motion by nuclear precession. Journal of geophysical research 1960; 65: 776-777.
46. Moran PR: A flow velocity zeugmatographic interlace for NMR imaging in humans. Magnetic Resonance Imaging 1982; 1: 197-203.
47. Moran PR, Moran RA, Karstaedt N: Verification and evaluation of internal flow and motion: true magnetic resonance imaging by the phase gradient modulation method. Radiology 1985; 154: 433-441.
48. van Dijk P: Direct cardiac NMR imaging of heart wall and blood flow velocity. Journal of Computer Assisted Tomography 1984; 8: 429-436.
49. Wedeen VJ: Imaging myocardial kinematics with MRI. Magnetic Resonance in Medicine 1992; 27: 52-67.
50. Hahn EL: Spin echoes. Physical Review 1950; 30: 580-594.
51. Torrey HC: Bloch equations with diffusion terms. Physical Review 1956; 104: 563-565.
52. Stejskal EO, Tanner JE: Spin diffusion measurements: spin echoes in the presence of a time-dependent field gradient. Journal of Chemical Physics 1964; 42: 288-292.
53. Wesbey GE, Moseley ME, Ehman RL: Translational molecular self-diffusion in magnetic resonance imaging. II. Measurement of the self-diffusion coefficient. Investigative Radiology 1984; 19(6): 491-498.
54. Murphy JA, Doane JW: An NMR measurement of the diffusion anisotropy in a nematic liquid crystals. Molecular crystal and liquid crystal 1971; 13: 93-95.

55. Kruger GJ, Spiesecke H: Anisotropy of the diffusion coefficient in nematic liquid solutions measured by NMR techniques. Zeitschrift fur Naturforschung A (Astrophysik, Physik und Physikalische Chemie) 1973; 28a: 964-967.

56. Ukleja P, Doane JW: The anisotropy of self-diffusion in the lamellar phase (using NMR). Ordering in Two Dimensions, Lake Geneva, WI, USA, 1980.

57. Callaghan PT, LeGros MA, Pinder DN: The measurement of diffusion using deuterium pulsed field gradient nuclear magnetic resonance. Journal of Chemical Physics 1983; 79: 6372-6381.

58. Finch ED, Harmon JF, Muller BH: Pulsed NMR measurement of the diffusion constant of water in muscle. Arch Biochem Biophys 1971; 147: 299-310.

59. Doran M, Hajnal JV, Van Bruggen N, King MD, Young IR, Bydder GM: Normal and abnormal white matter tracts shown by MR imaging using directional diffusion weighted sequences. Journal of Computer-Assisted Tomography 1990; 14: 865-873.

60. Cleveland GG, Chang DC, Hazlewood CF, Rorschach HE: Nuclear magnetic resonance measurement of skeletal muscle: anisotropy of the diffusion coefficient of the intracellular water. Biophysical Journal 1976; 16: 1043-1053.

61. Garrido L, Wedeen VJ, Spencer U, Kantor H: Anisotropy of water diffusion in the myocardium of the rat. Circulation Research 1994; 74: 789-793.

62. Yang Y, Shimony JS, Xu S, Gulani V, Dawson MJ, Lauterbur PC: A sequence for measurement of anisotropic diffusion by projection reconstruction imaging and its application to skeletal and smooth muscle. Proceedings of Society of Magnetic Resonance, Berkeley, California, 1994.

63. Muller MF, Prasad PV, Bimmler D, Kaiser A, Edelman RR: Functional imaging of the kidney by means of measurement of the apparent diffusion coefficient. Radiology 1994: 711-715.

64. Wu JC, Wong EC, Arrindell EL, Simons KB, Jesmanowicz A, Hyde JS: In vivo determination of the anisotropic diffusion of water and the T1 and T2 times in the rabbit lens by high-resolution magnetic resonance imaging. Invest. Ophthalmol. Vis. Sci. 1993; 34: 2151-2158.

65. Moseley ME, Cohen Y, Kucharczyk J, et al.: Diffusion-weighted MR imaging of anisotropic water diffusion in cat central nervous system. Radiology 1990; 176: 439-446.

66. Douek P, Turner R, Pekar J, Patronas N, LeBihan D: MR color mapping of myelin fiber orientation. Journal of Computer-Assisted Tomography 1991; 15: 923-929.

67. Basser PJ, Mattiello J, LeBihan D: MR diffusion tensor spectroscopy and imaging. Biophysical Journal 1994; 66: 259-267.

68. Edelman RR, Gaa J, Wedeen VJ, et al.: *In-Vivo* measurement of water diffusion in the human heart. Magnetic Resonance in Medicine 1994; 32: 423-428.

69. Reese TG, Wedeen VJ, Weisskoff RM: Measuring diffusion in the presence of material strain. J. Magn Reson B 1996; August, in press.

70. Reese TG, Weisskoff RM, Smith RN, Rosen BR, Dinsmore RE, Wedeen VJ: Imaging myocardial fiber architecture *in vivo* with magnetic resonance. Mag Reson Med 1995; 34: 786-791.

71. Lunkenheimer PP, Redmann K, Cryer CW, et al.: The difficult access to morphology of the heart: clinical implications. Technology and Health Care 1994; 2: 155-173.
72. Smaill BH, Hunter PJ: Structure and function of the diastolic heart: material properties of passive myocardium. In: Glass L, Hunter PJ, McCollough A, eds. Theory of heart. New York: Springer-Verlag, 1991; 1-29.
73. Arts T, Prinzen FW, Reneman RS: Chapter 7: Mechanics of the wall of the left ventricle. In: Strackee J, Westerhof N, eds. The physics of heart and circulation. London: Institute of Physics Publishing, 1993; 153-173.
74. LeGrice IJ, Hunter PJ, Smaill BH: Laminar structure of the heart: a mathematical model. American Journal of Physiology 1997; 272: H2466-H2476.
75. Lunkenheimer PP, Redmann K, Whimster WF, Theissen J, Frieling G, Lunkenheimer A: The problem created by myocardial structure in assessing myocardial function. Br J Anaesth 1988; 60: 2S-7S.
76. McLean M, Prothero J: Determination of relative fiber orientation in heart muscle: methodologic problems. Anatom Rec 1991; 232: 459-465.
77. Ross MA, Streeter DD, JR.: Nonuniform subendocardial fiber orientation in the normal macaque left ventricle. European Journal of Cardiology 1975; 3: 329-247.
78. Streeter DD, JR.,, Hanna WT: Engineering mechanics for successive states in canine left ventricular myocardium. 2. fiber angle and sarcomere length. Circulation Research 1973; 33: 639-655.
79. Kuribayashi T, Roberts WC: Myocardial disarray at junction of ventricular septum and left and right ventricular free walls in hypertrophic cardiomyopathy. American Journal of Cardiology 1992; 70: 1333-1340.
80. Hunter PJ, Nielsen PM, Smaill BH, LeGrice IJ, Hunter IW: An anatomical model of the heart with applications to myocardial activation and ventricular mechanics. Critical Reviews in Biomedical Engineering 1992; 20(5-6): 403-426.
81. Weyman AE: Cross-sectional echocardiography. Philadelphia: Lea & Febiger, 1982.
82. Costa KD: The structural basis of three-dimensional ventricular mechanics. University of California, San Diego; 1996.
83. Beltrami CA, Finato N, Rocco M, et al.: Structural basis of end-stage failure in ischemic cardiomyopathy in humans. Circulation 1994; 89: 151-163.
84. Omens JH, Covell JW: Transmural distribution of myocardial tissue growth induced by volume-overload hypertrophy in the dog. Circulation 1991; 84: 1235-1245.
85. Maron BJ, Roberts WC: Hypertrophic cardiomyopathy and cardiac muscle cell disorganization revisited: Relation between the two and significance. Am Heart J 1981; 102(1): 95-110.
86. Teare D: Asymmetrical hypertrophy of the heart in young adults. British Heart Journal 1958; 20: 1-8.

87. Eaton LW, Weiss JL, Bulkley BH, Garrison JB, Weisfeldt ML: Regional cardiac dilatation after acute myocardial infarction: recognition by two-dimensional echocardiography. N Engl J Med 1979; 300: 57-62.
88. Hochman JS, Bulkley BH: Expansion of acute myocardial infarction: An experimental study. Circulation 1982; 65: 1446-1450.
89. Henry WL, Clark CE, Epstein SE: Echocardiographic identification of the pathognomonic anatomic abnormality of IHSS. Circulation 1973; 47: 225-233.
90. Maron BJ, Roberts WC: Quantitative analysis of cardiac muscle cell disorganization in the ventricular septum of patients with hypertrophic cardiomyopathy. Circulation 1979; 59: 689-706.
91. Maron MB, Roberts WC: Hypertrophic cardiomyopathy. Circulation 1979; 59(4): 692-706.
92. Zhao MJ, Zhang H, Robinson TF, Factor SM, Sonnenblick EH, Eng C: Profound structural alterations of the extracellular collagen matrix in postischemic dysfunctional ("stunned") but viable myocardium. Journal of American College of Cardiology 1987; 10: 1322-1334.
93. Factor SM, Flomenbaum M, Zhao MJ, Eng C, Robinson TF: The effects of acutely increased ventricular cavity pressure on intrinsic myocardial connective tissue. Journal of American College of Cardiology 1988; 12: 1582-1589.
94. Tezuka F, Hort W, Lange PE, Nurnberg JH: Muscle fiber orientation in the development and regression of right ventricular hypertrophy in pigs. Acta Pathol Jpn 1990; 40: 402-407.
95. Wedeen VJ, Weisskoff RM, Reese TG, et al.: Motionless movies of myocardial strain rate using stimulated echoes. Magnetic Resonance in Medicine 1995; 33: 401-408.
96. Pelc NC: Tracking of cyclical motion using phase contrast cine MRI velocity data. JMRI 1995; in press.
97. Pelc NL, Bernstein MA: Optimized encoding for phase contrast flow measurement. SMRM 9th annual meeting, New York, New York, 1990.
98. Wedeen VJ, Reese TR, Smith RN, Rosen BR, Weisskoff RM, Dinsmore RE: Mapping myocardial architecture with diffusion anisotropy MRI. Soc Magn Reson 3rd Scientific Mtg, Nice, France, 1995.
99. Davis TL, Wedeen VJ, Weisskoff RM, Rosen BR: White matter visualization by echo-planar MRI. Society of Magnetic Resonance in Medicine 12th annual meeting, New York, N.Y., 1993.
100. Mattiello J, Basser PJ, Le Bihan D: The b matrix in diffusion tensor echo-planar imaging. Magnetic Resonance in Medicine 1997; 37: 292-300.
101. Basser PJ, Shrager R: Anisotropically Weighted MRI. International Society for Magnetic Resonance in Medicine, Vancouver, B.C., Canada, 1997.
102. Rogers WJ, Shapiro EP, Weiss JL, et al.: Quantitation of and correction for left ventricular systolic shortening by magnetic resonance tissue tagging and slice isolation. Circulation 1991; **84**: 721-723.
103. Meier GD, Ziskin MC, Bove AA: Helical fibers in myocardium of dogs change their pitch as they contract. American Journal of Physiology 1982; 243: H1-H12.
104. Ingels NBJ: Myocardial fiber architecture and left ventricular function. Technological Health Care 1997; 5: 45-52.

105. Horowitz A, Pearl M, Sideman S: Geodesics as a mechanically optimal fiber geometry for the left ventricle. Basic Res Cardiol 1993; 88 suppl 2: 67-74.
106. Rijcken J, Arts T, Bovendeerd P, Schoofs B, van Campen D: Optimization of left ventricular fibre orientation of the normal heart for homogeneous sarcomere length during ejection. European Journal of Morphology 1996; 34: 39-46.
107. Wickline SA, Verdonk ED, Miller JG: Three-dimensional characterization of human ventricular myofiber architecture by ultrasonic backscatter. Journal of Clinical Investigation 1991; 88: 438-446.
108. Moseley ME, Kucharczyk J, Asgari HS, Norman D: Anisotropy in diffusion-weighted MRI. Magnetic Resonance in Medicine 1991(19): 321-326.
109. Basser PJ, Mattiello J, LeBihan D: MR imaging of fiber tract direction and diffusion in anisotropic tissues. Society of Magnetic Resonance in Medicine 12th annual meeting, New York, N.Y., 1993.
110. Axel L, Dougherty L: MR imaging of motion with spatial modulation of magnetization. Radiology 1989; 171: 841-845.
111. Zhu Y, Drangova M, Pelc NJ: Fourier tracking of myocardial motion using cine PC data. Magnetic Resonance in Medicine 1996; 35: 471-480.
112. Meier GD, Ziskin MC, Santamore WP, Bove AA: Kinematics of the beating heart. IEEE Transactions on Biomedical Engineering 1980; BME-27: 319-329.
113. Prinzen FW, Arts T, Van der Vusse GJ, Reneman RS: Fiber shortening in the inner layers of the left ventricular wall as assessed from epicardial deformation during normoxia and ischemia. Journal of Biomechanics 1984; 17: 801-811.